PERMAFROST AND GROUND ICE CONDITIONS IN THE OGILVIE MOUNTAINS, CENTRAL YUKON

Thesis submitted to the University of Ottawa
in partial Fulfillment of the requirements for the
PhD in Geography

ROXANNE FRAPPIER

Department of Geography, Environment and Geomatics
Faculty of Arts
University of Ottawa

Supervisor:
Dr. Denis Lacelle, University of Ottawa

Examining committee:
Dr. Anders Knudby, University of Ottawa
Dr. Micheal Sawada, University of Ottawa
Dr. André Viau, University of Ottawa

Dr. Anna Liljedahl, Woodwell Climate Research Center
and University of Alaska Fairbanks

ABSTRACT

Permafrost is vulnerable to climate changes and the associated landscape changes that are enhanced by amplification processes and feedbacks unique to the Arctic. Permafrost degradation leads to important changes in terrestrial and aquatic ecosystems, and determining regions that are sensitive to permafrost degradation therefore represents an urgent issue. The Tombstone Territorial Park (TTP) and its surroundings (Ogilvie Mountains, central Yukon) represent one of those sensitive permafrost environment that should be monitored. The central Yukon is an enigmatic permafrost environment that reflects both Pleistocene and Holocene permafrost and climate conditions. The area is particularly intriguing because of the extensive presence of permafrost landforms that are more typical of areas much further north, especially ice-wedge (IW) polygons. It also represents a major transportation corridor linking multiple northern communities (Dempster Highway). Despite access along the road, and signs of permafrost degradation, there have been a limited number of studies addressing permafrost and ground ice conditions throughout the landscape. Consequently, this PhD thesis aims to characterize IW polygons, define the type and magnitude of landscape changes, and model permafrost distribution, conditions and sensitivity to climate changes in the study area.

Characterization of IW polygons reveals that they occupy 2.6% of the TTP and preferentially develop in woody sedge peat, glaciofluvial and alluvial deposits along the lower reaches of the Blackstone and East Blackstone rivers on hillslopes of ≤1°. Vegetation type, surface wetness, and polygon spatial pattern are influenced by the development stage of ice-wedge polygons, while the size and angles of polygons seem independent of the development stage.

A Landsat-based landscape change analysis of the TTP and surrounding region covering the 1986-2021 period shows that statistically significant spectral changes occurred in 24% of the study area, and most of these changes are associated with vegetation succession and hydrological processes (i.e., erosion and deposition). Other landscape changes included wildfires, slumps, changes to riverbanks and lake shores, earlier melting of icings in the summer, degradation on the peripheries of some ice wedge polygonal terrain, and potential insect damage to forests. The analysis reveals that the extent and magnitude of landscape changes in the study area are influenced by the geomorphic setting, ecological succession and glacial history of the region.

Modeling current and future permafrost conditions in the study area using the Northern Ecosystem Soil Temperature (NEST) model indicate that permafrost has persisted through the 20th century and beginning of the 21st century and is currently present throughout the area. Modeled mean permafrost depth (113.8 ± 49.6 m), active layer thickness (2.45 ± 7 m), surface, near-surface, and deep ground temperatures (−1 ± 1.2°C, −1.6 ± 1.2°C, −2.4 ± 1.3°C, respectively) are in the range of other local and regional measurements. Predicted ALTs and permafrost depth show areas of permafrost loss by 2100 (22% of study area under RCP4.5, and 29% under RCP8.5). Permafrost degradation in the study area could greatly impact slope stability and conditions of aquatic systems, and shrubification could contribute to increased degradation.

RÉSUMÉ

Le pergélisol est vulnérable aux changements climatiques et aux modifications du paysage qui y sont associées et qui sont renforcées par des processus d'amplification et des rétroactions propres à l'Arctique. La dégradation du pergélisol entraîne des changements importants dans les écosystèmes terrestres et aquatiques, et l'identification des régions sensibles à la dégradation du pergélisol représente donc un enjeux urgent. Le parc territorial de Tombstone (PTT) et ses environs (Monts Ogilvie, centre du Yukon) représentent l'un de ces environnements sensibles qu'il se doit d'être surveillé. Le centre du Yukon est un environnement de pergélisol énigmatique qui reflète les conditions climatiques et de pergélisol du Pléistocène et de l'Holocène. La région est particulièrement intrigante en raison de la présence étendue de formes de relief de pergélisol qui sont plus typiques des régions beaucoup plus au nord, notamment les polygones de coin de glace. Elle représente également un important couloir de transport reliant plusieurs communautés nordiques (Route Dempster). Malgré l'accès le long de la route et les signes de dégradation du pergélisol, il y a eu un nombre limité d'études sur les conditions du pergélisol et de la glace de sol dans l'ensemble du paysage. Par conséquent, cette thèse de doctorat vise à caractériser les polygones de coin de glace, définir le type et l'ampleur des changements de paysage, et modéliser la distribution, les conditions et la sensibilité du pergélisol aux changements climatiques dans la zone d'étude.

La caractérisation des polygones de coin de glace révèle qu'ils occupent 2,6 % du PTT et se développent préférentiellement dans la tourbe de carex, les dépôts fluvioglaciaires et les dépôts alluviaux le long des parties inférieurs des rivières Blackstone et East Blackstone sur des pentes de $\leq 1°$. Le type de végétation, l'humidité de surface et la configuration spatiale des polygones sont influencés par le stade de développement des polygones de coin de glace, tandis que la taille et les angles des polygones semblent indépendants du stade de développement.

Une analyse des changements de paysage du PTT et de la région environnante basée sur Landsat et couvrant la période 1986-2021 montre que des changements spectraux statistiquement significatifs se sont produits dans 24 % de la zone d'étude, et que la plupart de ces changements sont associés à la succession végétale et aux processus hydrologiques (c'est-à-dire l'érosion et le dépôt). Parmi les autres changements du paysage, nous observons des feux de forêt, des glissements de terrain, des modifications des berges des rivières et des lacs, la fonte précoce des aufeis en été, la dégradation en périphérie de certains terrains polygonaux de coins de glace et des dommages potentiels aux forêts par les insectes. L'analyse révèle que l'étendue et l'ampleur des changements de paysage dans la zone d'étude sont influencées par le contexte géomorphologique, la succession écologique et l'histoire glaciaire de la région.

La modélisation des conditions actuelles et futures du pergélisol dans la zone d'étude à l'aide du modèle Northern Ecosystem Soil Temperature (NEST) a montré que le pergélisol a persisté au cours du XXe siècle et au début du XXIe siècle et qu'il est actuellement présent dans toute la zone. La profondeur moyenne à la base du pergélisol (113,8 ± 49,6 m), l'épaisseur de la couche active (2,45 ± 7 m), la température de la surface, de la proche surface et en profondeur (−1 ± 1,2 °C, −1,6 ± 1,2 °C, −2,4 ± 1,3 °C, respectivement) sont conformes à d'autres mesures locales et régionales. Les mesures de couche active et de profondeur à la base du pergélisol prédites montrent des zones de perte de pergélisol d'ici 2100 (22 % de la zone d'étude sous RCP4.5 et 29 % sous RCP8.5). La dégradation du pergélisol dans la zone d'étude pourrait avoir un impact considérable sur la stabilité des pentes et sur les conditions des systèmes aquatiques, et l'augmentation de la répartition des arbustes pourrait contribuer à accroître cette dégradation.

REMERCIEMENTS

Je tiens d'abord à remercier mon superviseur, Denis Lacelle, pour son support en tant que superviseure de thèse et mentor. Denis, merci pour ta compréhension, ta flexibilité et ta disponibilité tout au long de mon doctorat. Merci d'avoir partagé avec moi ta passion pour la recherche. Tu m'as poussé à me poser plus de questions, à chercher plus loin et à ne pas trop vite tirer de conclusions; un bagage que j'emporterai avec moi tout au long de ma carrière. J'espère que nous aurons la chance de retravailler ensemble.

I would also like to thank Robert Fraser, Sylvain Legault and Yu Zhang for their collaboration all along my PhD project. Your guidance and help has been invaluable and I am honored to say I got to collaborate with you. In hopes that we get to work together again in the future.

Thank you to my thesis proposal committee members, Ian Clark, Robert Fraser, Anders Knudby and Toni Lewkowicz for their comments and suggestions on my thesis. And thank you to my thesis evaluation committee for their time and contribution to the completion of my doctorate degree.

J'aimerais aussi remercier Jean Bjornson pour son support à travers tout mon parcours académique. Jean, tu es vraiment un pilier du département, offrant ton support à plusieurs niveaux. Saches que le parcours de bien des étudiants, y compris le miens, ne serait pas pareil sans toi. Merci pour tout.

Merci aussi à mes collègues du département de Géographie, environnement et géomatique et particulièrement à Benoit F., Yifeng W., Hugo C., Kethra C-H, Nicolas C. et Michelle L., pour votre amitié et votre support.

Ce projet n'aurait pas été possible sans le support financier et logistique de l'Université d'Ottawa (Bourse d'admission), le gouvernement de l'Ontario (Bourse d'études supérieures de l'Ontario), les Fonds de recherche du Québec (Bourse d'études supérieures – Nature et Technologies), Ressources Naturelles Canada (Programme des adjoints de recherche), le Conseil de Recherche en Sciences Naturelles et Génie du Canada et le Programme de formation scientifique dans le Nord (Financement du travail de terrain).

Finalement, je tiens à remercier ma famille et mes amis pour leur support tout au long de mon parcours. Un merci spécial à mes parents, Gilles et Caroline, de m'avoir toujours fait sentir que j'étais capable de tout! Ça aura été un long chemin avec plusieurs hauts et bas, et je n'y serais pas arriver sans vous. Et un autre merci spécial à David et notre petit Louis d'avoir passé à travers tous ces hauts et ces bas avec moi, de m'avoir supporter, aimer et fait rire quand j'en avais besoin.

TABLE OF CONTENTS

LIST OF TABLES

LIST OF FIGURES

CHAPTER 1: INTRODUCTION

1.1 Introduction

The stability of permafrost is threatened by the ongoing climate warming and associated landscape changes that are enhanced by amplification processes and feedbacks unique to the Arctic (Arctic Monitoring and Assessment Programme (AMAP), 2017). Degradation of permafrost has important effects on terrestrial and freshwater ecosystems, and determining regions that are sensitive to permafrost degradation therefore represents an urgent issue for infrastructures, economy, health, food security and traditional usage of the landscape (Council of Canadian Academies, 2014; Hjort et al., 2022, 2018; Hovelsrud et al., 2011; Wesche and Chan, 2010; White et al., 2007).

The Tombstone Territorial Park and its surroundings (Ogilvie Mountains, central Yukon) represent one of those sensitive permafrost environment that should be monitored. The central Yukon is an enigmatic permafrost environment that reflects both Pleistocene and Holocene permafrost and climate conditions, since a large portion of the landscape has been ice-free since at least the Mid-Pleistocene (Duk-Rodkin, 1996). In some locations, permafrost is relict, while elsewhere it is in equilibrium with the recent climate (e.g., Monteath et al., 2023; Calmels et al., 2012). The area is particularly intriguing because of the extensive presence of permafrost landforms that are more typical of areas much further north (e.g., ice-wedge polygons, pingos, thaw slumps). It also represents a major transportation corridor linking multiple northern communities; The Dempster Highway cuts through the Ogilvie Mountains since the 1950s, making Eagle Plains accessible, and was extended all the way to Inuvik in 1979.

Despite access along the highway, there have been a limited number of studies addressing permafrost conditions in the area; Signs of permafrost degradation have been documented along the road, notably through gullying and ponding along high-center ice-wedge polygons troughs and thaw slumping (Lacelle et al., 2007, 2009; Grinter et al., 2019; Calmels et al., 2018). However, little is known about the conditions and state of permafrost and ground ice throughout the landscape. Consequently, this PhD thesis fulfills three main objectives: 1) Characterizing the distribution, morphometry, state and ice content of ice-wedge (IW) polygons in the study area, 2) defining the type and magnitude of landscape changes in the study area, and 3) modelling permafrost distribution, thermal conditions and sensitivity to climate changes in the study area.

1.2 Background literature

1.2.1 Permafrost fundamentals and distribution

Permafrost is defined as ground that remains at or below 0°C for at least two consecutive years. Its occurrence is determined by a balance between heat loss from ground surface, which is governed by climatic and surface conditions, and internal earth heat gain from depth (French, 2017). Large scale permafrost distribution is governed by climate, as shown by the zonal classification of permafrost spatial distribution based on the extent of land underlain by permafrost (i.e. continuous (90–100%), discontinuous (50–90%), sporadic (10–50%) or isolated (0–10%)), which closely follows the mean annual air and ground temperature isotherms (Heginbottom et al., 1995). This classification illustrates the climatic limit of permafrost distribution, but it does not take into account the influence of the geo-ecological system properties (Shur and Jorgenson, 2007). A number of complex interactions between topography, the physical properties of the ground, soil moisture, drainage, snow cover, waterbodies, fire, and vegetation can lead to positive and negative feedbacks to permafrost occurrence and sensitivity to climatic conditions (Shur and Jorgenson, 2007; Jorgenson et al., 2010). The relationships between permafrost and these local geo-ecological factors leads to a more complex representation of permafrost distribution involving climate-ecosystem interactions and should be considered when predicting the consequences of climate change on permafrost environments, which might be more dependent on local factors than broad-scale warming (Shur and Jorgenson, 2007).

1.2.2 Ice-rich permafrost sensitivity and associated landscape changes

A key component defining permafrost is ground ice content. Bodies of ground ice exist in various forms in permafrost including lenses, wedges, veins, sheets, seams, irregular masses, or individual crystals or coatings on mineral or organic particles (van Everdingen, 2005). The growth of bodies of ground ice can result in various landforms. The most widespread is ice-wedge (IW) polygonal terrain, which results from the freezing of water that infiltrated along thermal contraction cracks forming ice wedges that lead to a distinctive surface expression, with troughs or rims aligned on the axis of the ice wedges (Lachenbruch, 1962). IW polygons are either characterized as low-centered or high-centered; Low-centered polygons are associated with developing ice wedges, where cracking and freezing of infilling water causes outward and upward displacement of material, resulting in rims forming the edges of the depressed, often inundated, polygons; High-centered polygons are associated with melting of ice wedges, which causes the ground above it to subside, resulting in the formation of well-drained mounds surrounded by depressed troughs (French, 2017). IW polygons behave in a “quasi-cyclic” manner, cycling through developing, degrading, and stabilized stages. (Kanevskiy et al., 2017). As they cycle through their different development stages, the surface expression and landscape parameters are modified. Effects include changes in topography, hydrology, vegetation, energy balance, snow accumulation patterns, and soil carbon and nutrient fluxes (Gamon et al., 2012; Gouttevin et al., 2018; Jorgenson et al., 2015; Koch et al., 2018; Kokelj et al., 2009; Liljedahl et al., 2016; Sachs et al., 2010; Schuur et al., 2015; Walvoord and Striegl, 2007).

Permafrost ground ice content is a determinant factor of the thaw-susceptibility of permafrost landscapes, along with the ground thermal regime and surface conditions (Couture and Pollard, 2007; Shur and Jorgenson, 2007). Large volumes of ice located close to the surface are especially vulnerable to degradation because they are directly exposed to surface conditions changes (Couture and Pollard, 2007; Jorgensen et al., 2006, 2015; Kokelj et al., 2014; Lachenbruch, 1962). Ice-rich permafrost degradation may lead to the formation of thermokarst features such as thaw slumps and thaw lakes and basins, which also represent major landscape disturbances that lead to modifications of hydrological, geomorphic and ecological processes (Kokelj et al., 2015; Jorgenson and Shur, 2007). However, the presence of a protective vegetation or organic layer such as mosses and peat acts as a positive feedback to permafrost preservation by acting as an effective insulation to climate warming (Shur and Jorgenson, 2007).

Widespread permafrost thaw-related landscape changes have been documented in the Arctic and Sub-Arctic through increased thaw slumps, ponding associated with IW degradation, thaw lakes and thaw basins (e.g., Kokelj et al., 2015, 2017; Fraser et al., 2018; Jones et al., 2015; Lewkowicz and Way, 2019; Segal et al., 2016; Ward Jones et al., 2019; Jones et al., 2011; Lantz and Turner, 2015). On the other hand, some regions also seem to resist permafrost degradation (e.g., Edwards et al., 2016), or at least show very heterogenous and asynchronous changes (e.g., Edwards et al., 2016; Frost et al., 2018; Jorgenson et al., 2022), illustrating the importance of understanding the complex interactions between permafrost and the geo-ecological context.

1.2.3 Mapping and modelling permafrost and landscape changes

Mapping and modeling permafrost based on geomorphological, topographic and climatic variables is useful in determining the large-scale distribution of permafrost (e.g. Brown et al., 2002; Bonnaventure et al., 2012; Heginbottom et al., 1995; O'Neill et al., 2019). However, in a landscape characterized by ice-rich permafrost associated with IW and a wide range of landcover types, the small scale variations mean that higher spatial and temporal resolution data is needed (Abolt and Young, 2020). The Landsat satellite imagery offers a compromise between high spatial and temporal resolution, by providing the longest continuous imagery archive at a medium scale. Moreoever, when used in combination with multi-scale, multi-sensor remote sensing analyses, it becomes a valuable source to characterize permafrost and landscape disturbances (Carroll et al., 2016; Jones et al., 2021; National Research Council, 2014; Nitze et al., 2018; Short et al., 2011; van der Sluijs et al., 2018). Also, because mapping at higher spatial and temporal resolution can be time consuming, the usage of semi-automated and automated remote sensing techniques is ideal. For landscape change analysis, these techniques involve analysis of the spectral signature of different components of the permafrost landscape, or of high resolution digital elevation models (DEMs), and their change over time (e.g. Bernard-Grand'Maison and Pollard, 2018; Fraser et al., 2012, 2014, 2018; Frost et al., 2018; Steedman et al., 2017; Zhang et al., 2018). For permafrost conditions mapping and modelling, the geo-ecological factors affecting permafrost distribution and sensitivity need to be addressed, which is why process-based models that integrate the effects of climate, vegetation, ground features and hydrological dynamics, such as the Northern Ecosystem Soil Temperature (NEST) model, are optimal (Zhang et al., 2003).

1.3 Study area

1.3.1 Physiography

The study area is located in the Ogilvie Mountains, about 45 km north of Dawson City, central Yukon, and includes the Tombstone Territorial Park. Elevations vary between 416 and 2344 m a.s.l., although >95% of the area is above 800 m a.s.l. The northern part of the study area is formed of Precambrian to Paleozoic metasedimentary, ultramafic and sedimentary rocks, andthe rugged mountains in the southern area have developed in areas underlain by Mesozoic igneous and sedimentary rocks with the highest peaks formed from stocks of Cretaceous porphyritic syenite

(Green, 1972). The area is dissected by four main north-south oriented river valleys associated with Quaternary unconsolidated glacial, colluvial and alluvial sediments (Duk-Rodkin, 1996): the Chandindu and North Klondike Rivers flowing to the south; and the Blackstone and East Blackstone Rivers flowing northward and merging at the northern boundary of TTP, near Chapman Lake. The northern part of the study area is also host to tributaries of the Ogilvie River. Surficial deposits in the region is dominated by Holocene colluvium, as well as glacial deposits from the last two glaciations (McConnell and Reid) (Duk-Rodkin, 1996).

1.3.2 Climate

The study area is located in the continental subarctic climate zone and is characterized by short cool summers and long cold winters. In winter, the mountainous topography often traps Arctic air masses that create cold spells with air temperatures below -40°C (Hu and Pollard, 1997). The North Klondike River meteorological station (64.45°N, 138.22°W, 972.6 m a.s.l.) reports a mean annual air temperature of −5.4°C, a mean January air temperature of −23.3°C, and a mean July air temperature of 11.5°C (1967-2006; Environment and Climate Change Canada, 2022). Mean annual temperatures have experienced a slight increase between 1967 and 2006 (m=0.06C°), which seem to be driven by an increase in winter temperatures (m=0.2C°). The region receives on average 472.8 mm of total precipitation per year, with the great majority of it falling as snow. Total precipitations have also experienced an increase since 1967 (m=0.4 mm).

1.3.3 Vegetation

Alpine tundra vegetation prevails in the study area (Latifovic et al., 2017). Grassland tundra is characteristics of the northern river valleys and on mid- to gentle-slopes, and is dominated by sedge, shrub and lichen tussock communities (Smith et al., 2004). The highest peaks are sparsely vegetated or bare of any vegetation (Latifovic et al., 2017).. The lowest elevations located in the southern portion of the park (Chandindu and North Klondike river valleys) are characterized by open boreal forest dominated by white spruce. The limit of the boreal forest is located between c. 535-1450 m a.s.l. Shrubland tundra consisting mainly of dwarf birch and willow is also observed below the treeline and in wetter areas such as rivers and lakes shores and along the road, together with scattered patches of stunted black spruces (Smith et al., 2004).

1.3.4 Permafrost and climate history

Physiography, vegetation and climate ensure that permafrost is continuous in the study area, at least in the valleys north of North Fork Pass. Ground temperatures taken along the Dempster Highway between North Fork Pass and c. 10 km north of Chapman Lake indicate that permafrost is cold (below -2°C) (Calmels et al., 2018; Lacelle et al., 2009). Periglacial features include thermokarst lakes, IW polygons, active layer detachment slides, thaw slumps, rock glaciers, cryoplanation terraces, kame and kettle topography, icings, and a few pingos on the highly elevated plateaus and in the river valleys bottoms. The area is particularly interesting because of the extensive presence of permafrost landforms that are more typical of areas much further north and their presence is most likely due to the higher elevation and climatic history.

The vast majority of the landscape of the Ogilvie Mountains has remained unglaciated since at least the mid-Pleistocene, and glaciogenic sediments from the last two glaciations have become buried by accumulating colluvium since at least the mid-Holocene (Grinter et al., 2019; St-Jean et al., 2011). Additionally, buried glacier ice associated to the Reid Glaciation (MIS 8/6) near Chapman Lake and a buried perennial snow patch in the Red Creek valley dated to 30,720 ± 340 ^{14}C a BP (MIS 2) indicate that permafrost has persisted, at least locally, since the mid-Pleistocene (Lacelle et al., 2007; 2009). Grinter et al. (2019) obtained a time-series of IW activity in the TTP based on $^{14}C_{DOC}$ ages (n=15) of six IW exposed at different depths in a thaw slump along Two Moose Lake. The results indicate that IW found truncated at ca. 3 m below surface were developing between 32k-27k and 22k-12k cal yr BP. During the early Holocene, climate was likely too warm and wet for IW to grow and the valley bottoms received sedimentation during the mid- to late-Holocene (St-Jean et al., 2011). A new group of IW initiated in the overlying alluvial deposits around 6300 cal yr BP, with a peak between 3985 and 873 cal yr BP, a period during which climate was cool and moist and allowed permafrost to aggrade (Grinter et al., 2019; Ritchie, 1984).

1.3.5 Current maps of permafrost distribution

Current permafrost distribution and ground ice content models for the Canadian Arctic and Sub-Arctic are largely based on coarse resolution data (Brown et al., 2002; Bonnaventure et al., 2012; Heginbottom et al., 1993, 1995; O'Neill et al., 2019; Obu et al., 2019). The Brown et al. (2002) map is based on existing physiographic maps and shows continuous permafrost in the northern section of the study area with extensive discontinuous permafrost in the central and southern sections. The data is derived from the 1:10,000,000 scale original map (Brown et al.,

2002) and, while providing a unified international map of permafrost (Heginbottom et al., 1993), it does not allow for an accurate depiction of permafrost distribution in our study area. The Obu et al. (2019) permafrost map predicts continuous permafrost throughout most of the park with discontinuous permafrost present in valley bottoms. Their permafrost distribution map assumes that permafrost is in equilibrium with the 2000-2016 TTOP measurements and does not take into account the history of ground thermal conditions and changes of ground temperature under a warming climate. This can reduce the model accuracy under transient conditions, especially where permafrost is rapidly warming or cooling, where ground temperatures is close to 0 °C, where the soil moisture content is high, and under thick relict permafrost. The permafrost probability model (Bonnaventure et al., 2012) was developed from basal temperature of snow measurements in winter and ground-truthing of frozen-ground presence in summer. It shows a higher probability of permafrost (continuous) in the higher elevations of the study area, and lower probability (extensive to sporadic) in the lower elevations and plateaus. This distribution is not likely to be accurate since we find IW and permafrost in the lower valleys and along the Dempster Highway. The O'Neill et al. (2019) ground ice map is based on an expert-system approach incorporating datasets of surficial geology, deglaciation, paleovegetation, glacial lake and marine limits, and modern permafrost distribution. It predicts a combination of medium to low wedge ice contents in the northern valleys of the TTP, and negligible to low contents in the southern part, and data is missing for a great part of the study area. This distribution of ground ice in the study area could be accurate, but smaller scale investigations are necessary to confirm it.

Minimal research has been done in the TTP area to characterize permafrost and ground ice (Grinter et al., 2019; Lacelle et al., 2007; 2009; Michel, 1986), and, given the local variabilities associated with IW distribution, vegetation cover, topography and glacial history, further small-scale analysis is necessary to assess the state of permafrost and sensitivity of the study area to climate and surface disturbances.

1.4 Thesis organization and research objectives

This doctoral thesis is written in an article format. Each of the following chapters are manuscripts which contribute to improving the knowledge of the Ogilvie Mountains landscape as a mountainous permafrost niche and how it evolves with climate changes. Chapter 2 was published in a peer-reviewed journal, Chapter 3 is currently under review for publication in a peer-reviewed journal and Chapter 4 is in preparation for publication. References are separately provided at the end of each chapter. The specific research objectives addressed in each manuscript are described below.

Objective 1: *Characterize the distribution, morphometry, state and ice content of ice-wedge polygons in the study area*

Chapter 2 describes the spatial distribution, morphometry, development stage and wedge ice content of IW polygons in the Tombstone Territorial Park (TTP), which is located within the Ogilvie Mountains in Central Yukon.

We hypothesize that: 1) IW polygons are distributed in flat lowlands and low-gradient slopes because steeper slopes associated with IW do not have the typical surface polygonal forms of IW in flat areas (Mackay, 1990), and in organic-rich material (such as peatlands), alluvium and finer-grained material because they usually have lower soil temperatures (French, 2017; Kokelj et al., 2014); 2) IW polygons sites with differing surficial characteristics have different morphometric parameters and soil properties and are associated with different development stages; 3) based on evidence of permafrost thaw-induced ponding and gullying observed along the Dempster Highway and in previous local studies (Lacelle et al., 2007; Grinter et al., 2019), IW polygons are mostly in the degradation development stage, and 3) wedge ice content can be inferred using polygons morphometry.

These hypotheses are tested by: 1) manual delineation of polygonal terrain using high resolution satellite imagery (WorldView-2, resolution 50 cm); 2) comparison of the distribution of polygonal terrain with terrain factors (i.e., elevation, slope, and surficial deposits) to determine if IW polygons have a tendency to develop preferentially in association with specific landscape parameters; 3) detailed investigation of individual polygons sites for their morphometry (polygons area and diameter, troughs length and relative depth, intersections angle, randomness) using semiautomated GIS methods in Esri's ArcMap 10.6 and physical characteristics (ice content, organic matter content, wetness, vegetation composition) to determine the development stage of IW polygons; and 4) estimation of the volume of wedge ice from three-dimensional subsurface models created for individual polygons sites. Chapter 2 was published in the *Permafrost and Periglacial Processes* journal.

Frappier, R. and Lacelle, D. (2021). Distribution, morphometry and ice content of ice-wedge polygons in Tombstone Territorial Park, central Yukon, Canada, *Permafrost and Periglacial Processes*, *32*(4), 587-600. doi: 10.1002/ppp.2123

Objective 2*: Define the type and magnitude of landscape changes in the study area*

Chapter 3 presents a detailed analysis of landscape changes in the Tombstone Territorial Park and surrounding region of the Ogilvie Mountains based on trend analysis of Tasseled Cap (TC) transformation applied to a 35-years Landsat imagery time-series, multi-level image interpretation and forest-based classification.

Based on evidence of the presence of many permafrost thaw-related features in the study area (i.e., ponding and gullying along the Dempster Highway, degrading IW polygons, thaw slumps and thaw lakes (Calmels et al., 2018; Lacelle et al., 2007; 2009, Grinter et al., 2019)), documentation of recent widespread landscape changes in other similar ice-rich permafrost environments (e.g., Kokelj et al., 2015, Lewkowicz and Way, 2019; Fraser et al., 2018; Jones et al., 2011; Lantz and Turner, 2015), and knowledge of the changes associated with permafrost degradation (e.g., Stow et al., 2004; Liljedahl et al., 2016), we hypothesize that landscape changes associated with permafrost degradation will be observed in the study area through increased distribution of thaw lakes and/or drained thaw lake basins, evidence of thaw slumping, extensive vegetation greening and ponding associated with IW degradation.

This hypothesis is tested by: 1) detecting changes in the study area using Landsat-derived TC trend analysis; 2) interpreting these changes based on the TC RGB visual representation, interpretation of TC indices trends, classification of change and multi-level image interpretation; and 3) relating these changes to the geomorphic setting, ecology and glacial history of the area. Chapter 3 is currently under review for publication in a peer-reviewed journal.

Frappier, R., Lacelle, D. and Fraser, R.H. (in press). *Landscape Changes in the Tombstone Territorial Park region (central Yukon, Canada) from Multi-Level Remote Sensing Analysis* [Manuscript accepted for publication in Arctic Science].

***Objective 3**: Model permafrost distribution, thermal conditions and sensitivity to climate changes in the study area*

Chapter 4 presents results of modelling of permafrost distribution and thermal conditions in the Tombstone Territorial Park and surrounding region of the North Ogilvie Mountains for current and future conditions under different climate scenarios. Modelling was performed using the Northern Ecosystem Soil Temperature (NEST) model, a process-based model that integrates the effects of climate, vegetation, ground features and hydrological dynamics (Zhang et al., 2003). The NEST model has been proven efficient to simulate distribution and sensitivity of permafrost in a variety of landscapes (Zhang, Chen and Riseborough, 2006; Ou et al., 2016; Way, Lewkowicz and Zhang, 2018; Zhang et al., 2012). It was applied for the first time to a mountainous region in this study.

Our hypotheses are that 1) permafrost is distributed across the landscape, and reach from the highest mountains to the bottom of valleys and the forest where it has been preserved by the Mid-Holocene cooling and associated vegetation changes (Cwynar and Spear, 1995; Dyke, 2005; Ritchie, 1984); 2) permafrost has been warming and is expected to continue to warm despite showing little surface evidence of degradation, most likely because of the lack of massive ground ice; and 3) the NEST model provides a more accurate representation of permafrost distribution compared to other coarser resolution models.

These hypotheses were tested by running the NEST model to 1) generate detailed maps of permafrost distribution and thermal conditions in the study area; 2) describe permafrost change under two different climate scenarios (RCP4.5 and RCP8.5); and 3) evaluate the success of the application of the NEST model in a mountainous region.

Frappier, R., Zhang, Y. and Lacelle, D. (in preparation). *A process-based model of active layer thickness and permafrost conditions in Tombstone Territorial Park (Central Yukon).* [Manuscript in preparation].

1.5 Authorship and co-authorship contributions

The three manuscripts presented in this thesis (Chapters 2, 3 and 4) are first-authored by the PhD candidate, Roxanne Frappier. Research objectives, field data collection methods, and spatial and statistical analysis approaches were developed by R. Frappier in consultation with her thesis supervisor, Dr. D. Lacelle. Field data was collected by R. Frappier and D. Lacelle with help from field assistants during the 2019-2022 period. Contributions presented in each chapter originate from original ideas by R. Frappier and D. Lacelle (a co-author of each of the manuscripts).

R. Frappier wrote the manuscript presented in Chapter 2 with contributions from D. Lacelle. RF and DL collected data in the field with the help of field assistants. RF conducted remote sensing, laboratory and statistical analyses.

R. Frappier wrote the manuscript presented in Chapter 3 with contributions from D. Lacelle and Robert H. Fraser from the Canada Centre for Remote Sensing (Natural Resources Canada). RF performed the remote sensing and statistical analyses and interpreted the results. RHF provided support for the remote sensing analysis and interpretation of results. DL provided insight in the interpretation of results.

R. Frappier wrote the manuscript presented in Chapter 4 with contributions from D. Lacelle and Yu Zhang from the Canada Centre for Remote Sensing (Natural Resources Canada). RF and DL collected samples and installed instruments in the field with the help from field assistants. RF performed the laboratory analyses, permafrost modelling, and interpretation of results. YZ provided support with permafrost modelling. DL helped with interpretation of results.

1.6 References

Abolt CJ, Young MH. (2020). High-resolution mapping of spatial heterogeneity in ice wedge polygon geomorphology near Prudhoe Bay, Alaska. *Sci Data*. 2020. doi:10.1038/s41597-020-0423-9

Arctic Monitoring and Assessment Programme (AMAP), 2017. Snow, Water, Ice and Permafrost in the Arctic (SWIPA). Oslo.

Bernard-Grand'Maison C., Pollard W. (2018). An estimate of ice wedge volume for a High Arctic polar desert environment, Fosheim Peninsula, Ellesmere Island. *Cryosphere*. doi:10.5194/tc-12-3589-2018

Bonnaventure, P. P., Lewkowicz, A. G., Kremer, M., & Sawada, M. C. (2012). A Permafrost Probability Model for the Southern Yukon and Northern British Columbia, Canada. *Permafrost and Periglacial Processes, 23*(1), 52–68. https://doi.org/10.1002/ppp.1733

Brown, J., O. Ferrians, J. A. Heginbottom, and E. Melnikov. (2002). Circum-Arctic Map of Permafrost and Ground-Ice Conditions, Version 2 [Data Set]. Boulder, Colorado USA. National Snow and Ice Data Center. https://doi.org/10.7265/skbg-kf16

Calmels, F., Froese, D. G., & Clavano, W. R. (2012). Cryostratigraphic record of permafrost degradation and recovery following historic (1898-1992) surface disturbances in the Klondike region, central Yukon Territory. Canadian Journal of Earth Sciences, 49(8), 938–952. https://doi.org/10.1139/e2012-023

Calmels, F., Roy, L.P., Grandmont, K., Pugh, R., 2018. Summary of climate-and geohazard-related vulnerabilities for the Dempster Highway corridor.

Council of Canadian Academies, 2014. Aboriginal Food Security in Northern Canada: An Assessment of the State of Knowledge.

Couture NJ, Pollard WH. (2007). Modelling geomorphic response to climatic change. *Clim Change*, 85(3-4):407-431. doi:10.1007/s10584-007-9309-5

Cwynar, L. C., & Spear, R. W. (1995). Paleovegetation and Paleoclimatic Changes in the Yukon at 6 ka BP. *Géographie Physique et Quaternaire*, *49*(1), 29–35. https://doi.org/10.7202/033027ar

Duk-Rodkin, A., 1996. Surficial geology, Dawson, Yukon Territory, 1:250,000.

Dyke, A.S., 2005. Late quaternary vegetation history of northern North America based on pollen, macrofossil and faunal remains. Geographie Physique et Quaternaire 59, 211–262.

Edwards, M., Grosse, G., Jones, B.M., McDowell, P., 2016. The evolution of a thermokarst-lake landscape: Late Quaternary permafrost degradation and stabilization in interior Alaska. Sedimentary Geology 340, 3–14. https://doi.org/10.1016/j.sedgeo.2016.01.018

Environment and Climate Change Canada (2022). *Canadian Climate Station Data*. http://climate.weather.gc.ca.

Fraser, R., Kokelj, S., Lantz, T., McFarlane-Winchester, M., Olthof, I., Lacelle, D., 2018. Climate Sensitivity of High Arctic Permafrost Terrain Demonstrated by Widespread Ice-Wedge Thermokarst on Banks Island. Remote Sensing 10, 954. https://doi.org/10.3390/rs10060954

Fraser, R., Olthof, I., Carrière, M., Deschamps, A., Pouliot, D., 2012. A method for trend-based change analysis in Arctic tundra using the 25-year Landsat archive, in: Polar Record. pp. 83–93. https://doi.org/10.1017/S0032247411000477

Fraser, Robert H, Lantz, T.C., Olthof, I., Kokelj, S. v, Sims, R.A., 2014. Warming-Induced Shrub Expansion and Lichen Decline in the Western Canadian Arctic. Ecosystems 17, 1151–1168. https://doi.org/10.1007/s10021-014-9783-3

French HM. (2017). *The Periglacial Environment: Fourth Edition*.; Hoboken, NJ: John Wiley and Sons.

Fritz, M., Wolter, J., Rudaya, N., Palagushkina, O., Nazarova, L., Obu, J., Rethemeyer, J., Lantuit, H., & Wetterich, S. (2016). Holocene ice-wedge polygon development in northern Yukon permafrost peatlands (Canada). Quaternary Science Reviews, 147, 279–297. https://doi.org/10.1016/j.quascirev.2016.02.008

Frost, G. v., Christopherson, T., Jorgenson, M.T., Liljedahl, A.K., Macander, M.J., Walker, D.A., Wells, A.F., 2018. Regional patterns and asynchronous onset of ice-wedge degradation since the mid-20th century in Arctic Alaska. Remote Sensing 10. https://doi.org/10.3390/RS10081312

Gamon, J., Kershaw, G., Williamson, S., & Hik, D. (2012). Microtopographic patterns in an arctic baydjarakh field: do fine-grain patterns enforce landscape stability? *Environmental Research Letters*, *7*(1), 6. https://doi.org/10.1088/1748-9326/7/1/015502

Gouttevin, M.I., Langer, H. Löwe, J. Boike, M. Proksch, & M. Schneebeli. (2018). Observation and modelling of snow at a polygonal tundra permafrost site: spatial variability and thermal implications. *The Cryosphere*, *12*(11), 3693–3717. https://doi.org/10.5194/tc-12-3693-2018

Green LH. (1972). *Geology of Nash Creek, Larsen Creek, and Dawson Area Maps.* Ottawa: Geological Survey of Canada, Memoir 364.

Grinter, M., Lacelle, D., Baranova, N., Murseli, S., Clark, I.D., 2019. Late Pleistocene and Holocene ice-wedge activity on the Blackstone Plateau, central Yukon, Canada. Quaternary Research (United States) 91, 179–193. https://doi.org/10.1017/qua.2018.65

Heginbottom, J. A., Dubreuil, M. A., & Haker, P. T. (1995*). Canada permafrost*, 1:7 500 000 scale. The National Atlas of Canada, 5th Edition. Sheet MCR 4177, National Resources Canada: Ottawa.

Heginbottom, J.A., J. Brown, E.S. Melnikov, O. Ferrians (1993). Circumarctic Map of Permafrost and Ground Ice Conditions in *Permafrost: Sixth International Conference*, Beijing, Proceedings. Wushan, Guangzhou, China, South China University Press, volume 2, pp. 1132 1136.

Hjort, J., Karjalainen, O., Aalto, J., Westermann, S., Romanovsky, V.E., Nelson, F.E., Etzelmüller, B., Luoto, M., 2018. Degrading permafrost puts Arctic infrastructure at risk by mid-century. Nature Communications. https://doi.org/10.1038/s41467-018-07557-4

Hjort, J., Streletskiy, D., Doré, G., Wu, Q., Bjella, K., Luoto, M., 2022. Impacts of permafrost degradation on infrastructure. Nature Reviews Earth and Environment. https://doi.org/10.1038/s43017-021-00247-8

Hovelsrud, G.K., Poppel, B., van Oort, B., Reist, J.D., 2011. Arctic Societies, Cultures, and Peoples in a Changing Cryosphere. AMBIO 40, 100–110. https://doi.org/10.1007/s13280-011-0219-4

Hu, X., Pollard, W.H., 1997. The hydrologic analysis and modelling of river icing growth, North Fork Pass, Yukon Territory, Canada. Permafrost and Periglacial Processes 8, 279–294. https://doi.org/10.1002/(sici)1099-1530(199709)8:3<279::aid-ppp260>3.0.co;2-7

Jones, B.M., Grosse, G., Arp, C.D., Jones, M.C., Anthony, K.M.W., Romanovsky, V.E., Jones, C.:, 2011. Modern thermokarst lake dynamics in the continuous permafrost zone, northern Seward Peninsula, Alaska. Alaska, J. Geophys. Res 116, 0–03. https://doi.org/10.1029/2011JG001666

Jones, B.M., Grosse, G., Arp, C.D., Miller, E., Liu, L., Hayes, D.J., Larsen, C.F., 2015. Recent Arctic tundra fire initiates widespread thermokarst development. Scientific Reports 5. https://doi.org/10.1038/srep15865

Jorgenson, M T, Kanevskiy, M., Shur, Y., Moskalenko, N., Brown, D.R.N., Wickland, K., Striegl, R., Koch, J., 2015. Role of ground ice dynamics and ecological feedbacks in recent ice wedge degradation and stabilization. Journal of Geophysical Research F: Earth Surface. https://doi.org/10.1002/2015JF003602

Jorgenson, M.T. and Shur Y., (2007). Evolution of lakes and basins in northern Alaska and discussion of the thaw lake cycle. *Journal of Geophysical Research: Earth Surface, 112*(F2). https://doi.org/10.1029/2006JF000531

Jorgenson, M.T., Kanevskiy, M., Roland, C., Hill, K., Schirokauer, D., Stehn, S., Schroeder, B., Shur, Y., 2022. Repeated Permafrost Formation and Degradation in Boreal Peatland Ecosystems in Relation to Climate Extremes, Fire, Ecological Shifts, and a Geomorphic Legacy. https://doi.org/10.3390/atmos13081170

Jorgenson, M.T., Romanovsky, V., Harden, J., Shur, Y., O'Donnell, J., Schuur, E. a G., Kanevskiy, M., Marchenko, S., 2010. Resilience and vulnerability of permafrost to climate change. Canadian Journal of Forest Research 40, 1219–1236. https://doi.org/10.1139/X

Jorgenson, M.T., Shur, Y., & Pullman, E. (2006). Abrupt increase in permafrost degradation in Arctic Alaska. *Geophysical Research Letters*, *33*(2). doi: 10.1029/2005GL024960

Kanevskiy M., Shur Y., Jorgenson M.T., et al. (2017). Degradation and stabilization of ice wedges: Implications for assessing risk of thermokarst in northern Alaska. *Geomorphology*.

Koch, J.C., Jorgenson, M.T., Wickland, K.P., Kanevskiy, M. & Striegl, R. (2018). Ice Wedge Degradation and Stabilization Impact Water Budgets and Nutrient Cycling in Arctic Trough Ponds. *Journal of Geophysical Research: Biogeosciences* 123 : 2604–2616. doi: 10.1029/2018JG004528

Kokelj, S. v, Lantz, T.C., Tunnicliffe, J., Segal, R., Lacelle, D., 2017. Climate-driven thaw of permafrost preserved glacial landscapes, northwestern Canada. Geology 45, 371–374. https://doi.org/10.1130/G38626.1

Kokelj, S., Tunnicliffe, J., Lacelle, D., Lantz, T.C., Fraser, R.H., 2015. Retrogressive thaw slumps: From slope process to the landscape sensitivity of northwestern Canada. 68e Conférence Canadienne de Géotechnique et 7e Conférence Canadienne sur le Pergélisol, 20 au 23 septembre 2015, Québec, Québec.

Kokelj, S.V., Lantz, T.C., Wolfe, S.A., Kanigan, J.C., Morse, P.D., Coutts, R., Molina-Giraldo, N., Burn, C.R. (2014). Distribution and activity of ice wedges across the forest-tundra transition, western Arctic Canada. Journal of Geophysical Research, Earth Surface 119: 2032–2047. doi:10.1002/2014JF003085.

Kokelj, S.V., Zajdlik, B., & Thompson, M. (2009). The impacts of thawing permafrost on the chemistry of lakes across the subarctic boreal-tundra transition, Mackenzie Delta region, Canada. *Permafrost and Periglacial Processes*, *20*(2), 185–199. https://doi.org/10.1002/ppp.641

Lacelle, D., Lauriol, B., Clark, I.D., Cardyn, R., Zdanowicz, C., 2007. Nature and origin of a Pleistocene-age massive ground-ice body exposed in the Chapman Lake moraine complex, central Yukon Territory, Canada. Quaternary Research 68, 249–260. https://doi.org/10.1016/j.yqres.2007.05.002

Lacelle, D., St-Jean, M., Lauriol, B., Clark, I.D., Lewkowicz, A., Froese, D.G., Kuehn, S.C., Zazula, G., 2009. Burial and preservation of a 30,000 year old perennial snowbank in Red Creek valley, Ogilvie Mountains, central Yukon, Canada. Quaternary Science Reviews 28, 3401–3413. https://doi.org/10.1016/j.quascirev.2009.09.013

Lachenbruch AH. (1962). Mechanics of thermal contraction cracks and ice-wedge polygons in permafrost. *Geol Soc Am Spec Pap*.,70:1-66. doi:10.1016/0378-7788(86)90031-9

Lantz, T.C., Turner, K.W., 2015. Changes in lake area in response to thermokarst processes and climate in Old Crow Flats, Yukon. Journal of Geophysical Research: Biogeosciences 120, 513–524. https://doi.org/10.1002/2014JG002744Latifovic, R., Pouliot, D., Olthof, I., 2017. Circa 2010 Land Cover of Canada: Local Optimization Methodology and Product Development. Remote Sensing 9, 1098. https://doi.org/10.3390/rs9111098

Lewkowicz, A.G., Way, R.G., 2019. Extremes of summer climate trigger thousands of thermokarst landslides in a High Arctic environment. Nature Communications 2019 10:1 10, 1–11. https://doi.org/10.1038/s41467-019-09314-7

Liljedahl, A.K., Boike, J., Daanen, R.P., Fedorov, A.N., Frost, G. v, Grosse, G., Hinzman, L.D., Iijma, Y., Jorgenson, J.C., Matveyeva, N., Necsoiu, M., Raynolds, M.K., Romanovsky, V.E., Schulla, J., Tape, K.D., Walker, D.A., Wilson, C.J., Yabuki, H., Zona, D., 2016. Pan-Arctic ice-wedge degradation in warming permafrost and its influence on tundra hydrology. Nature Geoscience 9, 312–318. https://doi.org/10.1038/ngeo2674

Mackay JR. (1990). Some observations on the growth and deformation of epigenetic, syngenetic and anti-syngenetic ice wedges. *Permafr Periglac Process*.,1(1):15-29. doi:10.1002/ppp.3430010104

Michel FA. (1986). Isotope geochemistry of frost-blister ice, North Fork pass, Yukon, Canada. *Can J Earth Sci*. 1986. doi:10.1139/e86-054

Monteath, A. J., Kuzmina, S., Mahony, M., Calmels, F., Porter, T., Mathewes, R., Sanborn, P., Zazula, G., Shapiro, B., Murchie, T. J., Poinar, H. N., Sadoway, T., Hall, E., Hewitson, S., & Froese, D. (2023). Relict permafrost preserves megafauna, insects, pollen, soils and pore-ice isotopes of the mammoth steppe and its collapse in central Yukon. Quaternary Science Reviews, 299, 107878–. https://doi.org/10.1016/j.quascirev.2022.107878

O'Neill, H.B., Wolfe, S.A., and Duchesne, C. (2019). New ground ice maps for Canada using a paleogeographic modelling approach. *The Cryosphere, 13*(3), 753–773. https://doi.org/10.5194/tc-13-753-2019

Obu, J., Westermann, S., Bartsch A. et al. (2019). Northern Hemisphere permafrost map based on TTOP modelling for 2000–2016 at 1 km2 scale, *Earth-Science Review, 193*, 299-316. https://doi.org/10.1016/j.earscirev.2019.04.023

Ou, C., LaRocque, A., Leblon, B., Zhang, Y., Webster, K., & McLaughlin, J. (2016). Modelling and mapping permafrost at high spatial resolution using Landsat and Radarsat-2 images in Northern Ontario, Canada: Part 2 – regional mapping. *International Journal of Remote Sensing, 37*(12), 2751–2779. https://doi.org/10.1080/01431161.2016.1151574

Ritchie, J.C., 1984. Past and present vegetation of the far northwest of Canada. Past and present vegetation of the far northwest of Canada. https://doi.org/10.2307/2260178

Sachs, T., Giebels, M., Boike, J., & Kutzbach, L. (2010). Environmental controls on CH 4 emission from polygonal tundra on the microsite scale in the Lena river delta, Siberia. *Global Change Biology*, *16*(11), 3096–3110. https://doi.org/10.1111/j.1365-2486.2010.02232.x

Schuur, E.A.G., Mcguire, A.D., Schädel, C., Grosse, G., Harden, J.W., Hayes, D.J., Hugelius, G., Koven, C.D., Kuhry, P., Lawrence, D.M., Natali, S.M., Olefeldt, D., Romanovsky, V.E., Schaefer, K., Turetsky, M.R., Treat, C.C., and Vonk, J.E. (2015). Climate change and the permafrost carbon feedback. Nature, 520(7546), 171–179. doi: 10.1038/nature14338

Segal, R.A., Lantz, T.C., Kokelj, S. v, 2016. Acceleration of thaw slump activity in glaciated landscapes of the Western Canadian Arctic. Environmental Research Letters 11, 34025. https://doi.org/10.1088/1748-9326/11/3/034025

Shur, Y. L., & Jorgenson, M. T. (2007). Patterns of permafrost formation and degradation in relation to climate and ecosystems. *Permafrost and Periglacial Processes, 18*(1), 7–19. https://doi.org/10.1002/ppp.582

Smith, C. A. S., Meikle, J. C., & Roots, C. F. (2004). *Ecoregions of the Yukon Territory : biophysical properties of Yukon landscapes*. Agriculture and Agri-Food Canada.

Steedman, A.E., Lantz, T.C., Kokelj, S. v., 2017. Spatio-Temporal Variation in High-Centre Polygons and Ice-Wedge Melt Ponds, Tuktoyaktuk Coastlands, Northwest Territories. Permafrost and Periglacial Processes 28, 66–78. https://doi.org/10.1002/PPP.1880

St-Jean, M., Lauriol, B., Clark, I.D., Lacelle, D., Zdanowicz, C., 2011. Investigation of ice-wedge infilling processes using stable oxygen and hydrogen isotopes, crystallography and occluded gases (O2, N2, Ar). Permafrost and Periglacial Processes 22, 49–64. https://doi.org/10.1002/ppp.680

Stow, D.A., Hope, A., McGuire, D., Verbyla, D., Gamon, J., Huemmrich, F., Houston, S., Racine, C., Sturm, M., Tape, K., Hinzman, L., Yoshikawa, K., Tweedie, C., Noyle, B., Silapaswan, C., Douglas, D., Griffith, B., Jia, G., Epstein, H., Walker, D., Daeschner, S., Petersen, A., Zhou, L., Myneni, R., 2004. Remote sensing of vegetation and land-cover change in Arctic Tundra Ecosystems. Remote Sensing of Environment 89, 281–308. https://doi.org/10.1016/j.rse.2003.10.018

van Everdingen, R. (2005). Multi-language glossary of permafrost and related ground-ice terms. In *National Snow and Ice Data Center/World Data Center for Glaciology*, Boulder (Vol. 1998, Issue ed 1998 revised). https://doi.org/10.2307/1551636

Walvoord, M.A., Striegl, R.G., 2007. Increased groundwater to stream discharge from permafrost thawing in the Yukon River basin: Potential impacts on lateral export of carbon and nitrogen. Geophysical Research Letters 34, 12402. https://doi.org/10.1029/2007GL030216

Ward Jones, M.K., Pollard, W.H., Jones, B.M., 2019. Rapid initialization of retrogressive thaw slumps in the Canadian high Arctic and their response to climate and terrain factors. Environmental Research Letters 14. https://doi.org/10.1088/1748-9326/ab12fd

Way, R. G., Lewkowicz, A. G., & Zhang, Y. (2018). Characteristics and fate of isolated permafrost patches in coastal Labrador, Canada. *The Cryosphere, 12*, 2667–2688. https://doi.org/10.5194/tc-12-2667-2018

Wesche, S.D., Chan, H.M., 2010. Adapting to the Impacts of Climate Change on Food Security among Inuit in the Western Canadian Arctic. Ecohealth 7, 361–373. https://doi.org/10.1007/s10393-010-0344-8

White, D.M., Craig Gerlach, S., Loring, P., Tidwell, A.C., Chambers, M.C., 2007. Food and water security in a changing arctic climate. https://doi.org/10.1088/1748-9326/2/4/045018

Zhang, W., Witharana, C., Liljedahl, A. K., & Kanevskiy, M. (2018). Deep convolutional neural networks for automated characterization of arctic ice-wedge polygons in very high spatial resolution aerial imagery. *Remote Sensing, 10*(9). https://doi.org/10.3390/rs10091487

Zhang, Y., Chen, W., & Riseborough, D. W. (2006). Temporal and spatial changes of permafrost in Canada since the end of the Little Ice Age. *Journal of Geophysical Research Atmospheres*, 111(22). https://doi.org/10.1029/2006JD007284

Zhang, Y., Sachs, T., Li, C., & Boike, J. (2012). Upscaling methane fluxes from closed chambers to eddy covariance based on a permafrost biogeochemistry integrated model. *Global Change Biology*, *18*(4), 1428–1440. https://doi.org/10.1111/J.1365-2486.2011.02587.X

CHAPTER 2: DISTRIBUTION, MORPHOMETRY AND ICE CONTENT OF ICE-WEDGE POLYGONS IN TOMBSTONE TERRITORIAL PARK, CENTRAL YUKON, CANADA

Abstract

Investigations of the regional distribution of ice-wedge polygons and wedge-ice volume allows for the assessment of the vulnerability of permafrost landscapes to thaw-induced disturbances and related ecological feedbacks. Ice-wedge polygons have been described in multiple studies in flat terrain and low-gradient hillslopes, but few studies have examined ice-wedge polygons in mountainous terrain. This study investigates the distribution, morphometry and wedge-ice content of ice-wedge polygons in Tombstone Territorial Park, a mountainous permafrost region in central Yukon. Results show that ice-wedge polygons occupy 2.6% of the park and preferentially develop in woody sedge peat, glaciofluvial and alluvial deposits along the lower reaches of the Blackstone and East Blackstone rivers on hillslopes of ≤1°. The morphometry of five out of six polygonal sites studied showed statistically similar polygon sizes and trough angles, while showing different development stages based on vegetation type, surface wetness and spatial pattern. Estimation of wedge-ice volumes in the ice-wedge polygons is 8-22%, and is comparable to that of other Arctic regions. However, the estimated wedge-ice volume represents a minimum value because older generation of IW are truncated 3-4 m below the surface with no evidence of surface polygons and the polygonal network can be obscured by slope processes, vegetation and IW inactivity. This study provides insight on the application of morphometric and soil parameters for the assessment of ice-wedge polygons distribution and development stages.

2.1 Introduction

Ice-wedge (IW) polygons are one of the most widespread surface features in continuous permafrost terrain (French, 2013; Mackay, 1990; 1995). They can occur along hilltops, hillslopes and valley bottoms and their development is largely influenced by climate, surface materials, relief and surface moisture (Pewe, 1963; Mackay, 1976; Christiansen, 2005). IW polygons occur either as low-centered polygons with raised rims (typically associated with the early stages of IW development) or as high-centered polygons with well-drained elevated centers (typically associated with partial degradation of IW) (Mackay, 2000; Liljedahl et al., 2016; Kanevskiy et al., 2017). Polygonal terrain is susceptible to permafrost degradation and local subsidence because the top of IW is near the permafrost table and vulnerable to thermokarst (Kanesvkiy et al., 2017; Jorgenson et al., 2015; Couture and Pollard, 2007). Degradation of IW polygons landscape is accelerated by thermal erosion of the IW network and leads to the development of open gullies whereby the rapid drainage of surface runoff flowing into open cracks enhances the melting of IW and causes the ground surface to collapse (Fortier et al., 2007). The degradation of IW polygons not only modifies the local hydrology but over time, permafrost in the center of the IW polygons may degrade, release solutes and nutrients in the environment, and make stocks of soil organic carbon available to microbial decomposition (Jorgenson et al., 2015, 2013; Koch et al., 2018; Schuur et al., 2009; Zimov et al., 2006). Quantifying the distribution of IW polygons and wedge-ice volume at regional scale allows the assessment of the vulnerability of permafrost landscapes to thaw-induced disturbances and related ecological feedbacks (Jorgenson et al., 2015; Gogineni et al. 2014).

Recent advances in remote sensing data quality and techniques have facilitated mapping the distribution of IW polygons, quantifying their morphology and estimating wedge-ice volume (Ulrich et al., 2014; Bernard-Grand'Maison and Pollard, 2018; Zhang et al., 2018, 2020; Abolt et al., 2018; Abolt and Young, 2020). For example, investigations in northern Alaska found that wedge-ice typically occupies 5-20% of the upper 3 m of permafrost, depending on surficial geology and age of deposit (Kanevskiy et al., 2013; Jorgenson et al., 2014). Recently, an airborne lidar-derived digital elevation model (DEM) was used to delineate individual polygons on the Alaska North Slope based on a deep learning method, providing a high-resolution database of polygons in the 1200 km^2 study area (Abolt et al., 2018; Abolt and Young, 2020). In western Canada, the Mackenzie Valley air photo project (NWT Center for Geomatics, 2008) has mapped the distribution of IW polygons in the Tuktoyaktuk Coastlands (NWT, Canada) which were found to occupy 12.5% of landscape, with 92% of the polygons classified as high-centered (Steedman et al., 2017). IW polygons were also identified in other low-lying coastland regions of northwestern Canada where they were found both in flat terrain and on receding hillslopes (Mackay, 1990; Kanevskiy et al., 2017; Morse and Burn, 2013). In eastern Arctic Canada, IW polygons were observed in low-gradient fluvial terraces (Gagnon and Allard, 2020). Finally, in high Arctic Canada, GIS semi-automated techniques and high-resolution satellite imagery were used to map IW polygons where they were estimated to occupy c. 50% of the Fosheim Peninsula on Ellesmere Island (NU, Canada), with 3.8% of the top 5.9 m of permafrost hosting IW (Bernard-Grand'Maison and Pollard, 2018). To our knowledge, few studies have investigated the distribution and morphometry of IW polygons in mountainous regions.

The Ogilvie Mountains in central Yukon include IW polygons, thaw slumps and thaw lakes, providing evidence that the region contains ice-rich permafrost and is sensitive to climate change and surface disturbances (Lacelle et al., 2007, 2009; St-Jean et al., 2011; Grinter et al., 2019; Michel, 1986). The central Yukon is an enigmatic permafrost environment that reflects both Pleistocene and Holocene permafrost and climate conditions. In places, the permafrost is relict while elsewhere, it is in near-equilibrium with the contemporary climate. The objective of this study is to characterize the distribution, morphometry and wedge-ice volume of IW polygons in Tombstone Territorial Park (TTP) and relate these parameters to their stage of development. The objective was reached by first delimiting the distribution of polygonal terrain in TTP and exploring relations with terrain factors (i.e., elevation, slope, surficial deposits), then selecting polygonal sites and determining their geometry using semi-automated remote sensing techniques, and finally deriving an estimation of polygons' wedge-ice volume. This study provides insight on the distribution and morphometry of IW polygons and wedge-ice content in a sensitive permafrost region that includes the Dempster Highway, a major transportation corridor linking multiple northern communities.

2.2 Study area

The TTP is located in the Ogilvie Mountains, about 45 km north of Dawson City in the Yukon and is an important wildlife and transportation corridor (**Fig. 2.1**). The elevations in the park vary between 535 and 2345 m a.s.l., with 95% of the area being above 1000 m a.s.l. The northern section of the park consists of the Blackstone Plateau, formed of Precambrian to Paleozoic metasedimentary, ultramafic and sedimentary rocks (Green, 1972). The rugged mountains in the southern area are underlain by Mesozoic igneous and sedimentary rocks and the highest peaks consist of Cretaceous porphyritic syenite (Green, 1972). The TTP is characterized by three main north-south oriented river valleys: the Chandindu River flows south, the Blackstone and East Blackstone rivers flow north and join near Chapman Lake. Surficial deposits in the park are dominated by Holocene colluvium (83%) and Late Pleistocene glacial deposits (14%) over 20 m thick that form moraine plains and hummocky, ridged and hilly till complexes from the McConnell and Reid glaciations (Duk-Rodkin, 1996). Holocene alluvial plains deposits (3%) in the river valleys are characterized by 0-12 m thick coarse sand and gravel with minor silt and fine sand (Duk-Rodkin, 1996).

The region is located in the continental subarctic climate zone and is characterized by short cool summers and long cold winters. The closest meteorological station is situated just outside the TTP boundary along the North Klondike River (64.45°N, 138.22°W, 972 m a.s.l.) (**Fig. 2.1a**) and reports a mean annual air temperature of −5.4°C over the 1967-2006 period (mean January temperature: −23.3°C; mean July temperature: 11.5°C) (Environment Canada, 2016). The region receives on average 472 mm of total precipitation with c. 48% falling as snow. From December to March, the mountainous topography often traps Arctic air masses which create cold spells with air temperatures below −40°C (Hu and Pollard, 1997). Vegetation in the park consists mainly of alpine tundra with scattered patches of stunted black spruce and dwarf birch and willow below tree-line (<1450 m a.s.l) and in wetter areas along the shorelines of rivers and lakes.

Physiography, vegetation and climate ensure that permafrost is continuous in the TTP, at least in the valleys north of North Fork Pass (Duk-Rodkin, 1996), a highly elevated mountain pass that lies on the continental divide between the Arctic (Mackenzie river) and Pacific Ocean (Yukon River) watersheds. A borehole located 35 km north of TTP at c. 780 m a.s.l. reports a mean annual ground temperature in the −5 to −2°C range (Lacelle et al., 2009). In TTP, permafrost

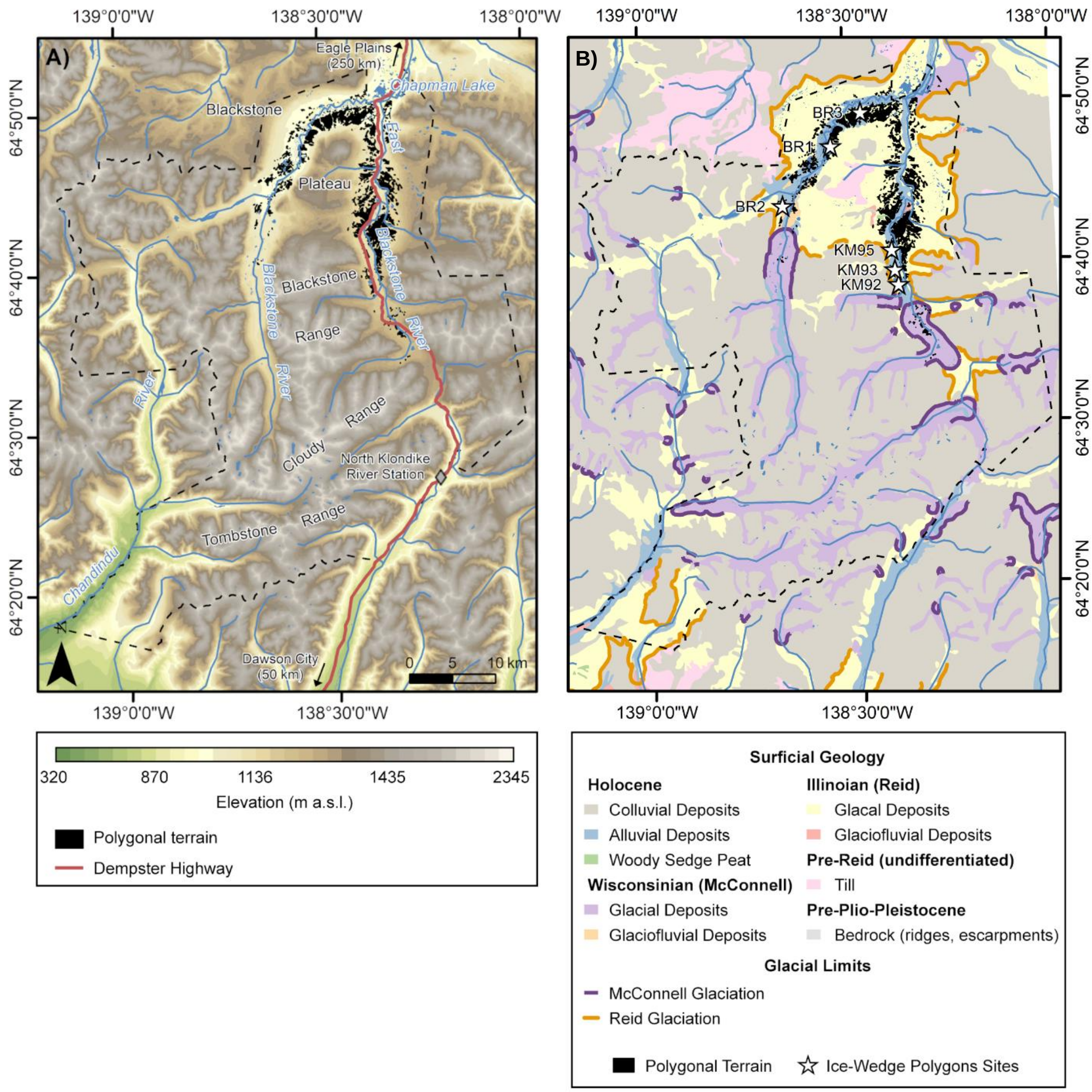

Figure 2.1 Maps showing distribution of ice-wedge polygons in the Tombstone Territorial Park, central Yukon. a) Ice-wedge polygons and elevations (Canadian Digital Elevation Model, Natural Resources Canada, 1945-2011). b) Ice-wedge polygons and surficial geology (Yukon Digital Surficial Geology Compilation, Yukon Geological Survey). Stars indicate the ice-wedge polygons sites studied within the Blackstone and East Blackstone River valleys.

geomorphology is highly influenced by the mountainous physiography. Surface features indicative of the presence of permafrost include IW polygons, active layer detachment slides, thaw slumps, thaw lakes, icings, and some pingos and frost mounds, which are all permafrost landforms that are more typical of regions much further North. The discovery of buried glacier ice associated to the Reid Glaciation near Chapman Lake and a buried perennial snow patch 35-40 km north of the study area dated to 30,720 ± 340 ^{14}C BP indicates that permafrost persisted, at least locally, since the late Pleistocene (Lacelle et al., 2007, 2009). A time-series of IW activity was established based on $^{14}C_{DOC}$ ages of six IW exposed in the headwall of a thaw slump along Two Moose Lake (Grinter et al., 2019). The results indicate that an older generation of IW truncated c. 3 m below surface were developing in the Reid-age glacial deposits between 32k-27k and 22k-12k cal yr BP. A new group of IW initiated in the overlying mid-Holocene age fine-grained colluvial deposits around 6300 cal yr BP, with a peak between 3985 and 873 cal yr BP, a period during which climate was cool and moist (Grinter et al., 2019).

2.3 Methodologies

2.3.1 Distribution of ice-wedge polygons

IW polygons in TTP were identified by surveying the entire extent of the park using WorldView-2 high-resolution satellite imagery (acquisition date: June 30th 2009; resolution 50 cm). The spatial extents of individual IW polygons zones were manually delineated in Esri's ArcMap 10.6. The Canadian Digital Elevation Model (CDEM; resolution 20 m) and the Yukon surficial geology map (Yukon Geological Survey; scale 1:250k) were used to investigate relations between the distribution of IW polygons and terrain factors (i.e., elevation, slope and surficial geology). The relative frequency distribution of IW polygons was normalized to the relative frequency distribution of terrain factors to determine whether the distribution of polygons reflects the distribution of landscape parameters or if some components are associated with enhanced probability of polygons occurrence (Hu and Pollard, 1997). This was done by dividing the relative frequency of IW polygons distribution by the relative frequency of terrain factors, with values >1 indicating that polygons occur preferentially in association with the particular terrain factor.

2.3.2 Morphometry of ice-wedge polygons

Out of all the polygons zones identified in TTP, six sites were selected for morphometric analysis; three sites located within the East Blackstone River valley, and three sites located within the Blackstone River valley. A semi-automated method using Esri's ArcMap 10.6 Spatial Analyst

Hydrology toolset was used to delineate polygons geometry at the six sites (**Fig. 2.2**). The method is based on the principle of watershed segmentation, where high-centered polygons troughs are treated as high elevations and the centers as low elevations (Bernard-Grand'Maison and Pollard, 2018). The Blackstone River valley sites are situated along the Dempster Highway and were visited in June 2019 to acquire high-resolution aerial photographs using a UAV (DJI Phantom 4 Pro). UAV flights were planned using the Pix4DCapture application, flying two consecutive nadir rectangle missions with 80% front and side overlap. A Digital Surface Model (DSM) for these sites was first built using Pix4Dmapper using the 0.8 cm resolution imagery, based on the hypothesis that high-resolution elevation models would produce higher confidence results (Bernard-Grand'Maison and Pollard, 2018). However, the high-resolution DSM proved not to be suitable for this method, since the very high-resolution imagery resulted in over-segmentation of polygons. A reduced-resolution DSM (57 cm) was therefore generated using the Aggregate tool in Esri's ArcMap 10.6. The DSM values were then inverted to mimic the mountain-valley morphology where the troughs (mountains) have higher pixel values and the centers (valleys) have lower pixel values (**Fig. 2.2**). For the three sites located within the Blackstone River valley, WorldView-2 high-resolution satellite imagery (acquisition date: June 30th 2009; resolution 50 cm) was used to delineate polygons geometry. Since troughs appear darker on the imagery, the values were scaled to 16-bit unsigned integer and inverted, resulting in an image that imitates the UAV-derived DSMs described above, with high values in the troughs and low values in the centers. Then, for all six inverted DSMs, ArcMap's Geostatistical Wizard was used to de-trend the data and obtain only the trough-center relief. A global polynomial interpolation was applied to extract the large-scale relative trend that was then subtracted from the image. The last two steps were performed one to three times until only the trough-center morphology was visible.

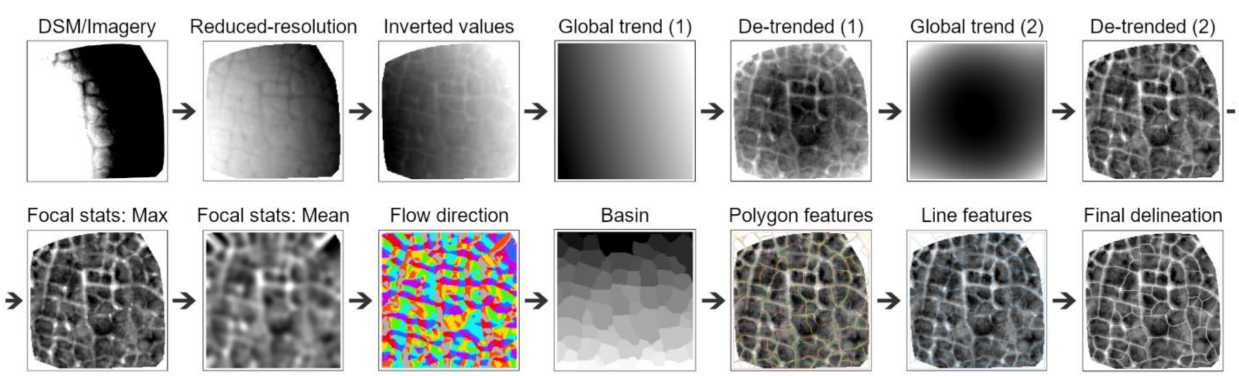

Figure 2.2 Flow diagram of method used to delineate the geometry of ice-wedge polygons in Esri's ArcMap 10.6 software.

The resulting image was smoothed using the Focal Statistics tool to accentuate the trough-center morphology by reducing noise (Bernard-Grand'Maison and Pollard, 2018). The Focal Statistics max tool was used once, followed by an iteration of the Focal Statistics mean tool. For each iteration, watersheds were created using the Flow Direction and Basin tools and the iteration is stopped before the watersheds begin to merge and represent more than one individual polygon. The result is a polygon shapefile delineating each individual polygon at each site (**Fig. 2. 2**).

The description of the morphometry of polygons at each site includes polygon network geometry, polygon size (diameter and surface area), trough length and relative depth and polygon angles (e.g., Mackay, 2000; Matthews et al., 1998; Lachenbruch, 1962; Forter and Allard, 2004). The spatial point pattern analysis (SPPA) can determine whether the polygon network geometry is random or regular, which provides a basis for identification of underlying geomorphic implications (Dutilleul et al., 2009; Haltigin et al., 2010). The SPPA is a proxy of the relation between the polygons size and spatial pattern and it was suggested that the relation may be dependant on the nature of the substrate and age of the polygons. A polygonal network would initially show a random pattern determined by the random distribution of thermal stresses in the ground, and evolve towards regularity due to the progressive subdivision of primary polygons into secondary and tertiary polygons (Lachenbruch, 1962; Plug et al., 2001). Additionally, IW polygons developed in homogeneous fine-grained deposits would exhibit a more regular pattern than those developed in heterogeneous coarse-grained materials (Dutilleul et al., 2009; Haltigin et al., 2010). The evaluation of polygon clustering, regularity, and randomness is based on nearest-neighbor distance using the x-y coordinates of the trough intersections as input data and the cumulative relative frequency distribution of nearest-neighbour distances, which is then compared to that expected under the assumption of complete spatial randomness (CSR) (Diggle, 1979, 2013; Van Lieshout and Baddeley, 1996). The SPPA of the six sites was done using the Gest function (nearest-neighbour distribution function G), with the 5^{th} rank CSR simultaneous critical envelope curves generated from 999 independent random simulations using the same number of points and area of interest as the site (Baddeley and Turner, 2005). An interval of distance values r was also set with a minimum of 0.5 m representing estimated minimum trough widths, and a maximum larger than the site mean polygon diameter (Baddeley et al., 2014). Clustered (random) pattern is indicated by $G(r) > G_{CSR}(r)$ and regular pattern by $G(r) < G_{CSR}(r)$. However, CSR cannot be rejected only based on $G(r) < G_{CSR}(r)$ because taking into account all r simultaneously leads to a multiple testing problem (de Jongh and van Lieshout, 2022). Additional testing was done to further support results; Histograms of nearest-neighbour distances were plotted, where a lack of small NN distances is indicative of regularity (Dutilleul et al., 2009). and maximum absolute deviation (MAD) between G(r) and $G_{CSR}(r)$ were computed, where CSR is rejected at a significance level of $\alpha = 2(5)/999+1$, expressed as a p-value <0.01 (Baddeley et al., 2014). All SPPA tests were performed using the Spatstat package 1.63-3 in the R integrated development environment (IDE). Histograms and MAD tests results are presented in Appendix A (**Fig. S2.2, S2.3, S2.4 and Table S2.2, S2.3**).

The geometry of individual polygons (i.e., surface area, perimeter, diameter, trough depth and angles) was characterized based on the polygon's delineation. Diameter of the polygons was determined using the Minimum Bounding Geometry tool in ArcMap 10.6. The minimum bounding length, which represents the longest axis of the polygons, is used as the diameter of polygons. The relative depth of the troughs was determined from transects between centers and troughs at the three sites located within the Blackstone River by extracting the elevation from the UAV-derived DSM. The angles that form each individual polygon were determined based on the bearing angles of each polygons segment using the Add Geometry Attribute function in ArcMap 10.6 to calculate the start-to-end bearing of each segment feature.

2.3.3. Estimation of wedge-ice volume

The volume of wedge-ice at each of the six sites of IW polygons was estimated from three-dimensional subsurface models (3D SSM) (Ulrich et al., 2014; Bernard-Grand'Maison and Pollard, 2018). Based on measurements of IW exposed in slumps and gullies in TTP (Grinter et al., 2019), and electrical resistivity tomography surveys performed within the study area (Camels et al., 2018), three scenarios were modeled where the IW have constant depth of 3 m with increasing widths of 1, 2 and 3 m, respectively. Using the Buffer and Erase tool in ArcMap 10.6, a polygon feature was created, representing only the soil portion of the polygons from the top of permafrost to the maximum depth of the IW (3 m), separated by a gap representing the different IW widths. A dissolved polygon feature was also created to outline the edges of the polygons site. A depth of –3 m was assigned to the IW center lines (created using the watershed segmentation method) and to the dissolved polygon feature and a depth of 0 was assigned to the polygon centers. These three features were used to create a TIN (triangulated irregular network) which forms the

3D SSM for the polygon centers. To estimate the volume of wedge-ice, the total volume of the site (soil and ice) was calculated based on the surface area of the site and the depth of the IW (3 m), and the volume of the polygon centers were calculated based on the 3D SSM using the Polygon Volume tool. The wedge-ice volume was then calculated as:

$$WI\ volume\ (\%) = \left(\frac{V_t - V_s}{V_t}\right) \times 100 \qquad (1)$$

where V_t represents the total site volume (soil and ice) and V_s represents the soil volume.

2.3.4. Statistical analyses

The Shapiro-Wilk test for normality was performed on the data of the six polygon sites and it was determined that it should be log transformed to meet the assumption of normality. An ANOVA within subjects and post-hoc Tukey's HSD tests were performed to determine whether the log-transformed means of geometry parameters between the six polygon sites (surface area, perimeter, diameter and angles) were statistically different. All statistical analyses were performed in the R IDE.

2.4 Results

2.4.1. Distribution of ice-wedge polygons in TTP

Areas with IW polygons, which range in surface area from 960 m^2 to 4.8 km^2, occupy 2.6% of the park and all are situated along the lower reaches of the Blackstone and East Blackstone river valleys (**Fig. 2.1**). The IW polygons are found between 975 and 1265 m elevation and on slopes of 0 to 12° (**Fig. 2.3b, c**). However, the majority of the polygons are located between 985-1135 m (95%) and on slopes of ≤3° (98.5%) (**Fig. 2.3b, c**). Normalizing the distribution of IW polygons to terrain factors indicates that the polygons preferentially develop at elevations of 995-1045 and 1065-1135 m by factors of 3 to 10.5 and on slopes of 0 and 1° by factors of 8 and 5, respectively (**Fig. 2.3b, c**). The majority of the polygons (80%) occur in glacial deposits and the remainder are located in the alluvial plains of the Blackstone and East Blackstone rivers (18%) and woody sedge peat deposits (0.4%) (**Fig. 2.3a**). Normalizing the surface area occupied by polygons by the area occupied by the surface deposits indicate that the polygons occur preferentially in woody sedge peat and glaciofluvial deposits by factors of 10 to 15, and in glacial deposits and alluvium by factors of 4 to 7 (**Fig. 2.3a).**

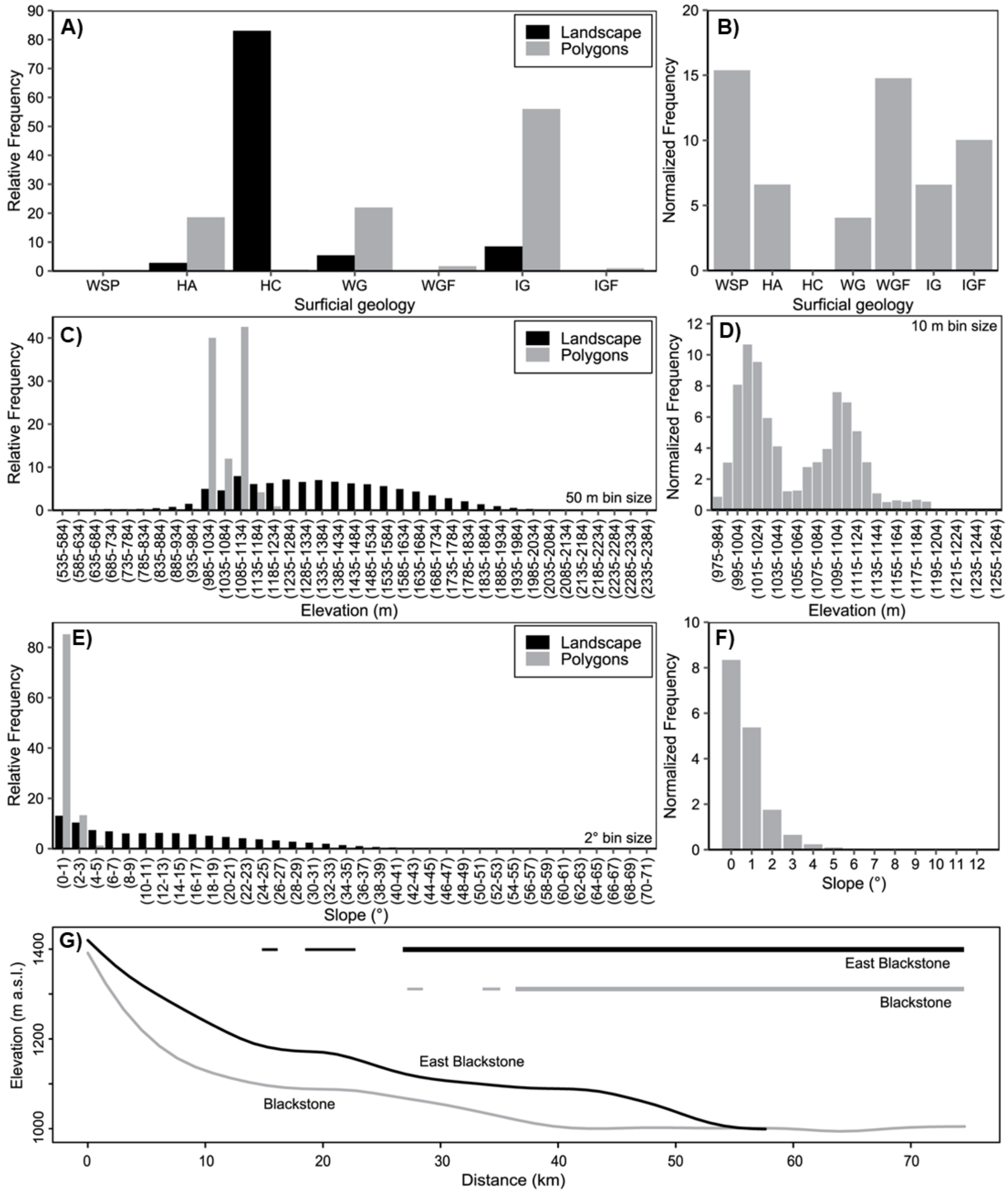

Figure 2.3 Frequency distribution of ice-wedge polygons and landscape factors in the Tombstone Territorial Park, central Yukon. A) Histogram of the fraction of ice-wedge polygons zones mapped in each type of surficial deposits (WSP; woody sedge peat, HA; Holocene Alluvium, HC; Holocene Colluvium, WG; Wisconsinian Glacial, WGF; Wisconsinian Glaciofluvial, IG; Illinoian Glacial, IGF; Illinoian Glaciofluvial) and the fraction of the study area corresponding to each type of surficial deposits. B) Enhancement factor of surficial deposits on occurrence of ice-wedge polygons in the landscape. Values greater than 1 indicate that ice-wedge polygons occur preferentially in these types of surficial deposits. C) Histogram of the

fraction of ice-wedge polygons zones mapped in each elevation class (50 m bins) and the fraction of the study area falling within each elevation class. D) Enhancement factor of elevation (10 m bins) on occurrence of ice-wedge polygons in the landscape. Values greater than 1 indicate that ice-wedge polygons occur preferentially at these elevations. E) Histogram of the fraction of ice-wedge polygons zones mapped in each slope class (2° bins) and the fraction of the study area falling within each slope class. F) Enhancement factor of slope on occurrence of ice-wedge polygons in the landscape. Values greater than 1 indicate that ice-wedge polygons occur preferentially at these slopes. G) Blackstone and East Blackstone rivers elevation profiles, with indications of the presence of ice-wedge polygons in the valleys.

2.4.2. Morphometry and physical parameters of ice-wedge polygons

Three sites located within the East Blackstone River valley, and three sites located within the Blackstone River valley were selected for morphometric analysis (**Fig. 2.1b**). Along the East Blackstone River valley, the three sites have similar surface areas (3470 to 5676 m^2) but show different stages of development (**Fig. 2.4**). Site KM93 is a mixture of both high- and low-centered polygons located in organic-rich Holocene alluvial deposits that accumulated over Reid-age glacial deposits. The polygons at the site showed no visible sign of change between the July 1989 aerial photo and the July 2009 satellite imagery (**Fig. 2.4a, b**). Vegetation consists of lichens in the troughs and mosses and graminoids in the centers, with dwarf shrubs in both the polygon centers and the troughs (**Fig. 2.4d**). Coring at the site in June 2019 revealed a thaw depth of 25 cm in the center and 10 cm in the trough, and the top of the IW was found 40 cm below the surface (**Fig. S2.1, Appendix A**). The polygons show a well-defined trough-ridge-center micro-relief, with the depth of the troughs varying between 10 and 20 cm, apparent rims on either side of the troughs, and low centers up to 30 cm deep (**Fig. 2.5c**). The SPPA identified 60 trough intersections and the cumulative relative frequency distribution of nearest-neighbour distances falls within the random point pattern (**Fig. 2.5b**). The presence of small nearest-neighbour distances also indicates a random point pattern and the MAD test results accept the CSR (**Fig. S2.2 and Table S2.2, Appendix A**). The diameters of polygons range from 6.1 to 21 m (average of 14.8 ± 3.6 m), with their surface area ranging from 20.5 to 294 m^2 (average of 124 ± 69.9 m^2) (**Table 2.1**). The cumulative length of troughs reaches 1233.4 m. The polygons form mainly hexagonal angles: ranging from 70-160° with a median of 113° (average of 118 ± 36°) (**Fig. 2.5d**).

Site KM92 is characterized by dry high-centered polygons and is located in Holocene alluvial deposits overlying Reid-age glacial deposits. Comparison of the 1989-2009 imagery reveals the subdivision of some polygons and widening of some troughs (**Fig. 2.4a, b**). Vegetation

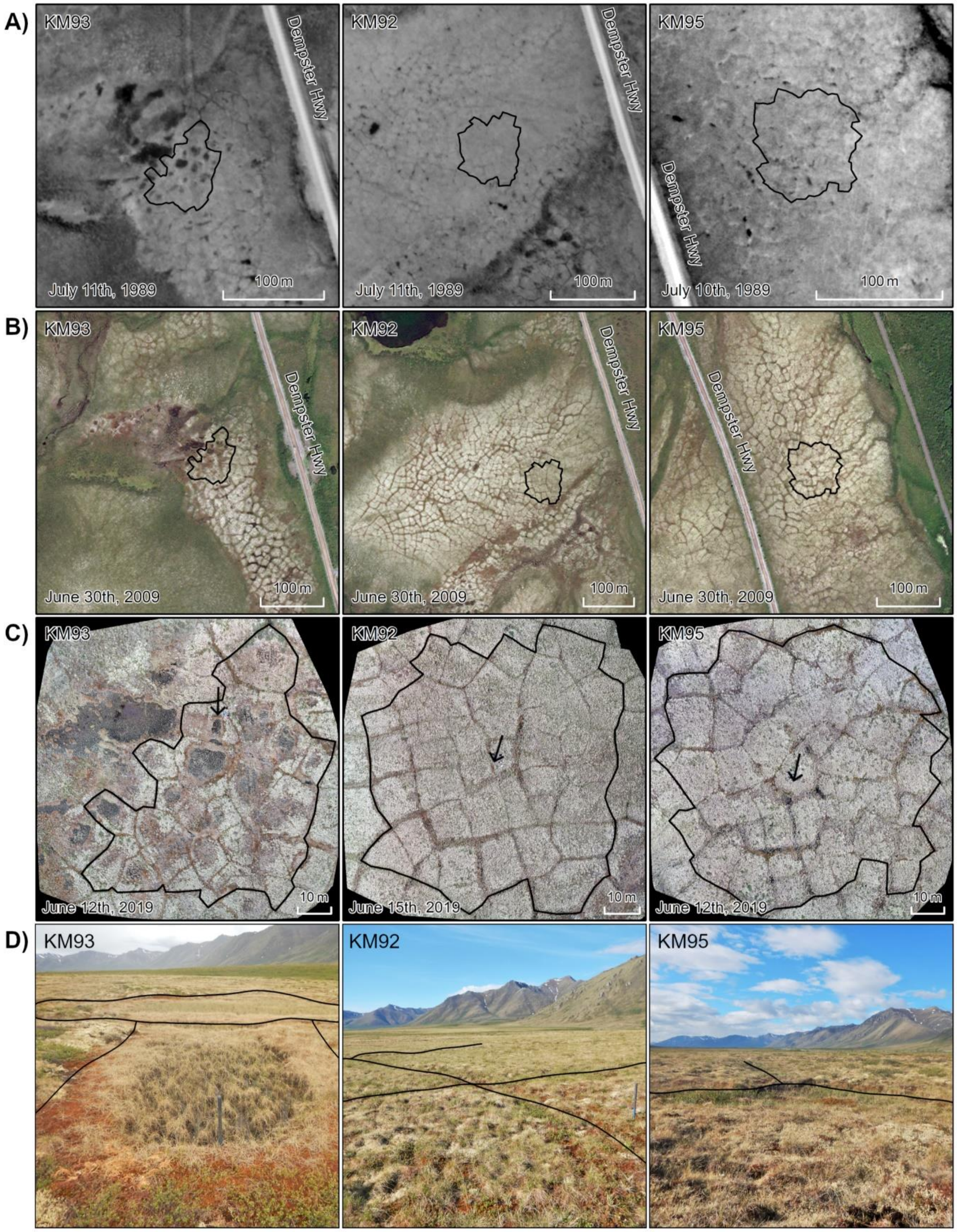

Figure 2.4 Historical imagery comparing three ice-wedge polygons sites located within the East Blackstone River valley, Tombstone Territorial Park, central Yukon. A) Aerial photography (July 1989; National Air Photo Library); B) WorldView-2 satellite imagery (July 2009; DigitalGlobe); C) UAV imagery (June 2019). Arrows indicate the direction from which the photographs shown in D) were taken; D) Field photographs (June 2019) with approximate locations of observed polygons troughs.

in the troughs is dominated by mosses and graminoids (**Fig. 2.4d**). In June 2019, the thaw depth reached 10 cm in the polygon center and 12 cm in the trough and the IW was found 70 cm below the surface (**Fig. S2.1, Appendix A)**. The polygons have a subdued morphology with the depth of the troughs varying between 15 and 25 cm; there are no evident rims on either side of the troughs and centers are relatively flat (**Fig. 2.5c**). The SPPA identified 73 trough intersections and the cumulative relative frequency distribution of nearest-neighbour distances falls along the lower boundary of the random point pattern envelope (**Fig. 2.5b**). The distribution of nearest-neighbour distances indicates an intermediate point pattern and the MAD test results accept the CSR (**Fig. S2.2 and Table S2.2, Appendix A**). The diameters of polygons range from 5.7 m to 23.3 m (average of 14.5 ± 4 m), with their surface area ranging from 20 to 267 m^2 (average of 122.5 ± 58 m^2) (**Table 2.1**). The cumulative length of troughs reaches 1684.7 m. The polygons form mainly orthogonal angles: ranging from 80-160° with a median of 105° (average of 119 ± 44°) (**Fig. 2.5d**).

Table 2.1 Results of one-way ANOVA comparing means of geomorphometry of six sites of ice-wedge polygons in Tombstone Territorial Park, central Yukon, Canada.

	Median	Mean	SD	Median	Mean	SD	Median	Mean	SD	ANOVA	
	Site KM93			Site KM92			Site KM95			*F*	*p*
Surface area (m^2)	109.89	123.93	69.86	114.56	122.51	58.63	120.23	132.02	66.02	0.48	0.62
Diameter (m)	14.98	14.84	3.58	14.18	14.44	3.97	14.5	15.75	5.15	0.9	0.41
Perimeter (m)	41.26	44.05	11.59	44.46	44.33	11.39	45.69	46.93	13.01	0.69	0.5
Angles (°)	113.25	118.54	36.67	105.58	119.81	44.19	118.51	124.89	44.1	1.05	0.35
	Site BR1			Site BR2			Site BR3			*F*	*p*
Surface area (m^2)	143.4	156.4	93.4	128	151	76.2	340	356.5	159.8	36.1	<0.05
Diameter (m)	15.6	16.3	5	15.3	16	3.9	24.9	24.9	6.3	34.8	<0.05
Perimeter (m)	48.6	49.5	14.8	45.8	48.5	11.8	74.7	75.8	18.8	36.2	<0.05
Angles (°)	112.7	117.8	40.3	112.1	119.2	38.9	116.5	126.3	44.4	2.25	0.11

	ANOVA	
	F	*p*
Surface area (m^2)	*20.3*	*<0.05*
Diameter (m)	18.3	<0.05
Perimeter (m)	19.7	<0.05
Angles (°)	1.33	0.25

Note. ANOVA performed on log-transformed (base 10) data based on Shapiro-Wilk test for normality (significance level α < 0.05).

Site KM95 is characterized by high-centered polygons with a mixture of narrow and wide troughs and occurs in Holocene-age alluvial deposits that accumulated over Reid-age glacial deposits. Between 1989-2009, there has been significant polygon degradation of the site where the faint polygonal pattern with a few small ponds at trough intersections observed in 1989 evolved to deeper dark troughs in 2009, making the polygonal pattern more visible (**Fig. 4a, b**). The thaw depth in June 2019 reached 15 cm in the center and 10 cm in the trough and the IW is located >105 cm below surface, the maximum depth of coring. The polygons have a subdued morphology with no evident rims on either side of the troughs, but present deep (up to 30 cm) and wide troughs (up to 4 m) in some places (**Fig. 2.5c**). Vegetation in the troughs is dominated by mosses and lichens, with some graminoids and dwarf shrubs (**Fig. 2.4d**). Some troughs are very wet, especially at polygons intersections, and these are characterized by bare soil and graminoids. The SPPA identified 83 trough intersections and the cumulative relative frequency distribution of nearest-neighbour distances falls predominantly within regular point pattern (**Fig. 2.5b**). The lack of small nearest-neighbour distances is also indicative of regularity and the MAD test results reject the CSR (**Fig. S2.2 and Table S2.2, Appendix A**). The diameters of polygons range from 7.9 to 37.8 m (average of 15.7 ± 5.2 m) with their surface area ranging from 32.5 to 387.2 m^2 (average of 132 ± 66 m^2) (**Table 2.1**). The cumulative length of troughs reaches 2018 m. The polygons form mainly hexagonal angles: ranging from 60-160° with a median of 118° (average of 124 ± 43°) (**Fig. 2.5d**).

Within the Blackstone river valley, the three sites have surface areas ranging from 9059 to 14,541 m^2 and show different stages of development. One of them (BR3) also occurs in a different type of surficial sediments, that is glacial deposits. Site BR1 is characterized by high-centered polygons with inundated troughs that in some places form large trough ponds (**Fig. 2.6a**). It is located within Holocene alluvial deposits. The SPPA identified 161 trough intersections and the cumulative relative frequency distribution of nearest-neighbour distances falls along the lower boundary of the random point pattern (**Fig. 2.6b**). The presence of small nearest-neighbour distances indicates randomness and the MAD test results are at the limit between accepting and rejecting CSR (**Fig. S2.2 and Table S2.2, Appendix A**). The diameters of polygons range from 5.7 m to 28 m (average of 16.3 ± 5 m), with their surface area ranging from 15.7 to 526 m^2 (average of 122.5 ± 58 m^2) (**Table 2.1**). The cumulative length of troughs reaches 1513 m. The polygons have a wide range of angles but form a majority of orthogonal angles: ranging from 30-252° with a median of 113° (average of 118 ± 40°) (**Fig. 2.6c**).

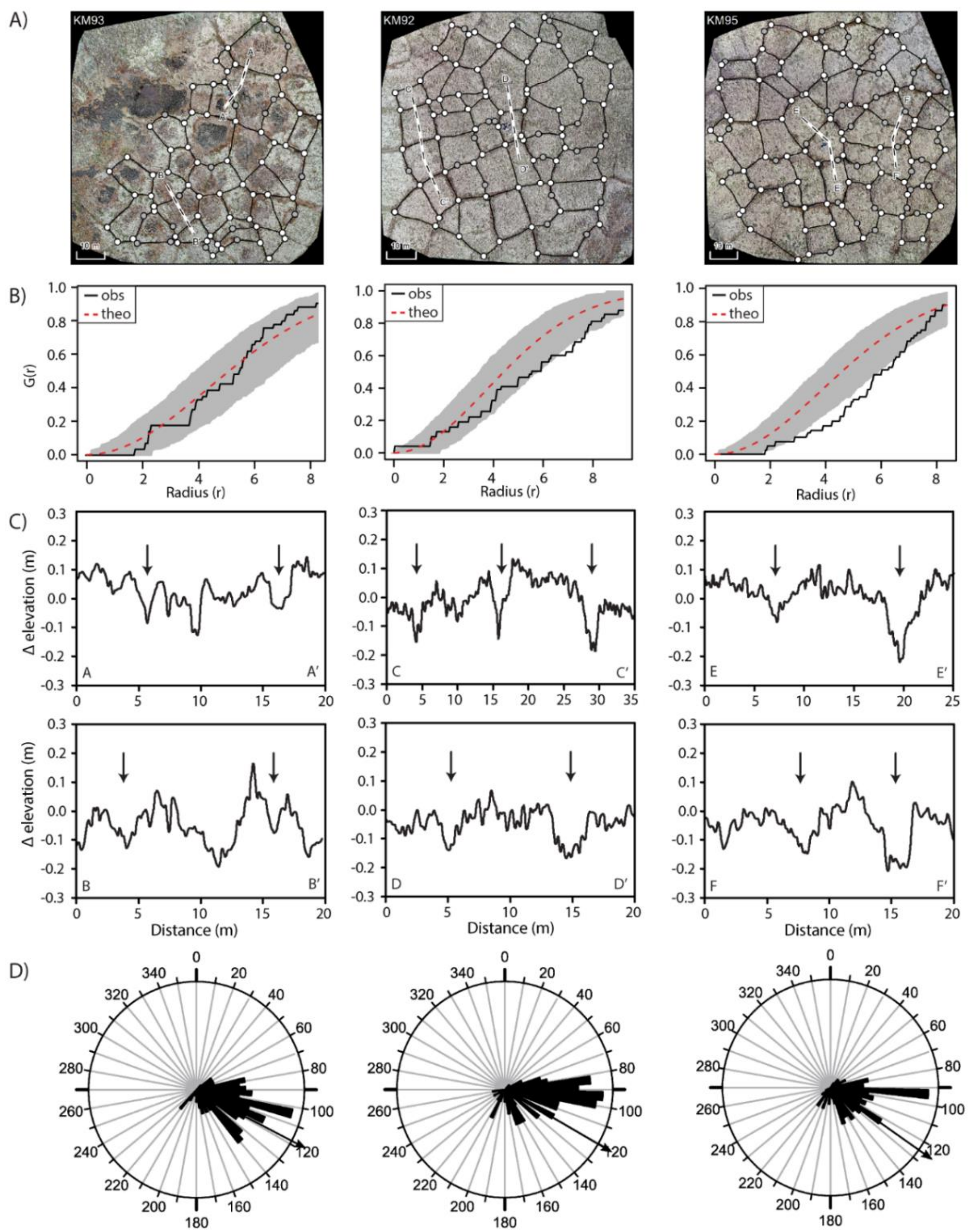

Figure 2.5 Morphometry of three ice-wedge polygons sites located within the East Blackstone River valley, Tombstone Territorial Park, central Yukon. A) UAV imagery (June 2019) overlapped with individual polygons delineation (black line), intersections used for the spatial point pattern analysis (white dots), angles forming each individual polygon (white and grey dots), and micro-relief transects (dashed black and white line). B) G-function with observed cumulative relative frequency distribution (G) of ice-wedge polygons intersections nearest-neighbour distances (r), theoretical values of G(r) for 999 simulations of complete spatial randomness (CSR), and 5th rank CSR envelope curves defining completely random distribution. C) Relative elevation of micro-relief transects. D) Angles forming each individual polygon. Arrow indicate mean angle for the entire site.

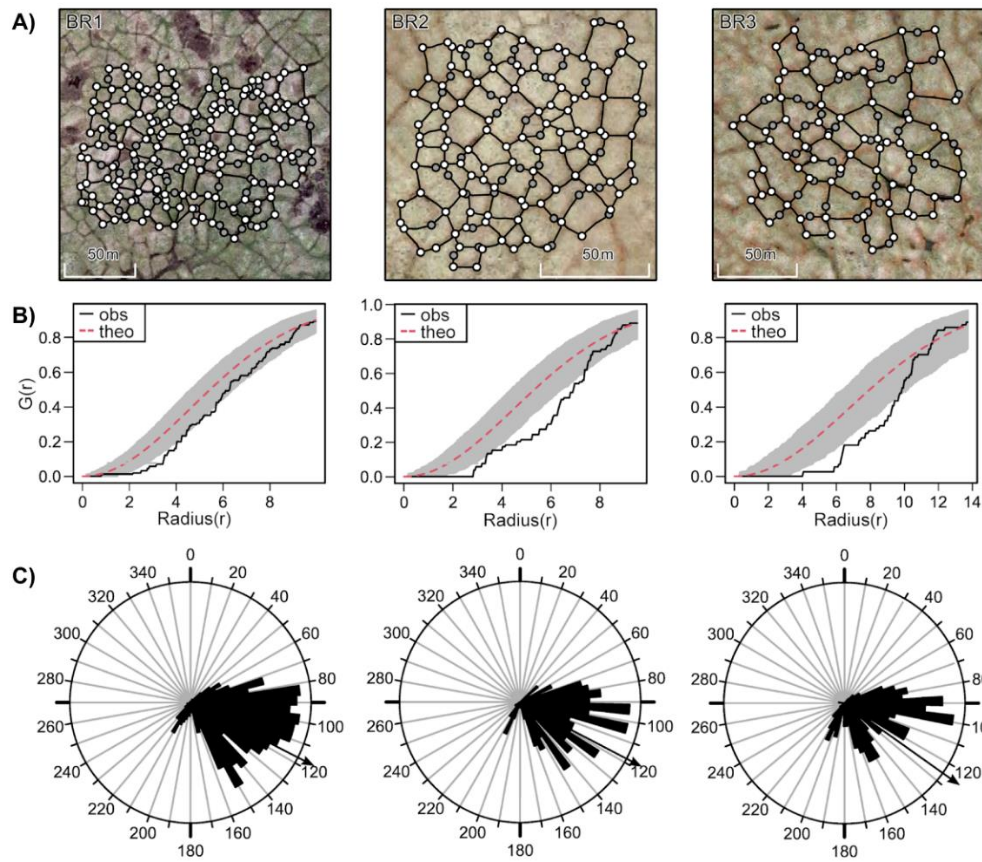

Figure 2.6 Morphometry of three ice-wedge polygons sites located within the Blackstone River valley, Tombstone Territorial Park, central Yukon. A) WorldView-2 satellite imagery (July 2009; DigitalGlobe) overlapped with individual polygons delineation (black line), intersections used for the spatial point pattern analysis (white dots) and angles forming each individual polygon (white and grey dots). B) G-function with observed cumulative relative frequency distribution (G) of ice-wedge polygons intersections nearest-neighbour distances (r), theoretical values of G(r) for 999 simulations of complete spatial randomness (CSR), and 5th rank CSR envelope curves defining completely random distribution. C) Angles forming each individual polygon. Arrow indicate mean angle for the entire site.

Site BR2 is formed of high-centered polygons with a few wet troughs and occurs in Holocene-age alluvial deposits. The SPPA identified 109 trough intersections and the cumulative relative frequency distribution of nearest-neighbour distances mostly falls within the regular point pattern (**Fig. 2.6b**). The lack of small nearest-neighbour distances is also indicative of regularity and the MAD test results reject the CSR (**Fig. S2.2 and Table S2.2, Appendix A)**. The diameters of polygons range from 9 m to 26 m (average of 16 ± 4 m), with their surface area ranging from 50 to 324.3 m^2 (average of 151 ± 76.2 m^2) (**Table 2.1**). The cumulative length of troughs reaches

2907 m. The polygons have a wide range of angles but form a majority of orthogonal angles: ranging from 42-243° with a median of 112° (average of 119.2 ± 39°) (**Fig. 2.6dc**).

Site BR3 is characterized as high-centered polygons with wide troughs and wet polygons intersections. It occurs within Reid-age glacial deposits. The SPPA identified 78 trough intersections and the cumulative relative frequency distribution of nearest-neighbour distances mostly falls within the regular point pattern (**Fig. 2.6b**). The lack of small nearest-neighbour distances is also indicative of regularity and the MAD test results reject the CSR (**Fig. S2.2 and Table S2.2, Appendix A**). The diameters of polygons range from 14.5 m to 43.3 m (average of 25 ± 6.3 m), with their surface area ranging from 108 to 727 m^2 (average of 356.5 ± 159.8 m^2) (**Table 2.1**). The cumulative length of troughs reaches 2804 m. The polygons have a wide range of angles but form a majority of orthogonal angles: ranging from 43-277° with median of 116.5° (average of 126.3 ± 44.4°) (**Fig. 2.6c**).

2.4.3 Estimation of wedge-ice volume in ice-wedge polygons

Wedge-ice volume was estimated in each of the six polygon sites using IW depth of 3 m and increasing widths of 1 to 3 m. Based on the three scenarios, the wedge-ice volume at the sites ranges from 8 to 22% (**Table 2.2**). The estimation of wedge-ice volume is based on the center line of IW (i.e., length of polygonal trough), and the ANOVA tests indicate that the morphometric parameters of the six sites are statistically different (**Table 2.1**). However, the post-hoc Tukey's HSD test revealed that five out of six polygons' sites had statistically similar morphometric parameters (all situated in Holocene-age alluvial deposits), with site BR3 being statistically different to the other sites. Site BR3 is located in Reid-age glacial deposits and had higher polygon diameter, perimeter and surface area values (**Table 2.1**). Considering that the IW polygons in TTP occur preferentially in glacial deposits and alluvium by factors of 4-7, the estimation of wedge-ice is likely transferable to the other IW polygons, with larger polygons in Reid-age glacial deposits containing slightly less wedge-ice volume (5-15%) than those developed in Holocene-age alluvial deposits (8-25%).

Table 2.2 Ice wedge volume estimation in six polygonal sites in Tombstone Territorial Park, central Yukon. Ice wedge depth is 3m for all scenarios.

Site	IW width (m)	Total site volume (m^{-3})	Sediment volume (m^{-3})	IW volume (m^{-3})	IW volume (%)
KM93	1	10414.9	9517	897	8.6
	2		8676	1739	16.7
	3		7878	2537	24.4
KM92	1	13971.5	12746	1225	8.8
	2		11594	2377	17.1
	3		10497	3475	24.9
KM95	1	17037.9	15570	1468	8.6
	2		14187	2850	16.7
	3		12876	4162	24.4
BR1	1	43623.7	40269	3355	7.7
	2		37102	6522	15.0
	3		34124	9500	21.8
BR2	1	27177.5	25058	2119	7.8
	2		23057	4121	15.2
	3		21168	6010	22.1
BR3	1	39576.5	37511	2066	5.2
	2		35521	4056	10.2
	3		33608	5968	15.1
Mean (SD)	1				7.8 (1.3)
	2				13 (2.5)
	3				22.1 (3.7)

2.5 Discussion

2.5.1. Distribution and morphometry of ice-wedge polygons in TTP

IW polygons occupy 2.6% of TTP, which is much lower than in other regions; for instance, they occupy 12.5% of landscape in the Tuktoyaktuk Coastlands and c. 50% of the Fosheim Peninsula on Ellesmere Island (Bernard-Grand'Maison and Pollard, 2018; Steedman et al., 2017). The reduced distribution of IW polygons in TTP results from the development of IW being constrained by hillslope processes and the hydrological network: IW polygons occur along the lower reaches of the Blackstone and East Blackstone valleys within slopes ≤1°, and they are absent from the upper and middle reaches (**Fig. 2.3d**). In the latter sections, the hillslopes either expose bedrock or are covered by thin colluviated sediments that prevent the development of IW. The lower reaches of the fluvial valleys are wider with low-gradient meandering and anastomosing channels, which are characterized by high aggradation rates, especially on low-gradient floodplains (Makaske, 2001). This section is covered by blankets of glacial deposits and veneers of alluvial and colluvial sediments that accumulated during the Holocene and/or Pleistocene (**Fig. 2.1**). Therefore, the thicker sediment deposits favor the development of IW polygons since at least the middle of the Holocene. This contrasts with non-mountainous regions where IW polygons are more broadly distributed in low-lying areas, flat terrain or rolling hills (Kanevskiy et al., 2017; Bernard-Grand'Maison and Pollard, 2018; Steedman et al., 2017; Morse and Burn, 2013; Fraser et al., 2018).

Four of the six selected sites are located in Holocene-age fine-grained alluvial deposits (KM92, KM95, BR1 and BR2), whereas KM93 is found almost exclusively in Holocene-age organic material and BR3 is located in Reid-age glacial deposits. The ANOVA with post-hoc Tukey's HSD test indicates that site BR3 had statistically different morphometric parameters (polygon surface area, diameter and perimeter) compared to the other five sites (**Table 2.1**). Polygon diameters and IW depths of these five sites are in the range of those along the Beaufort Sea coast of Alaska where polygons diameters average 14-15 m and IW reaching depths of 3 to 4 m (Zhang et al., 2018). Site BR3 is characterized by wider troughs and a mean polygon diameter 2.5-3 times as large as the other sites. At Two Moose Lake, Grinter et al. (2019) observed the presence of IW truncated c. 3 m below surface that developed in Reid-age glacial deposits, with the IW dated between 32k-27k and 22k-12k cal yr BP. IW polygons at site BR3 are most likely contemporaneous to these buried IW, suggesting that this polygon network may be in disequilibrium with Holocene climate.

The distribution of G(r) versus the nearest-neighbour distances *r* of the polygons intersections at sites KM95, BR2, and BR3 falls mostly below the CSR envelope (**Fig. 2.5b, 2.6b**). This, along with the lack of small nearest-neighbour distances and MAD test results (**Fig. S2.2 and Table S2.2, Appendix A**), suggests regular patterns. Sites KM92 and BR1 are distributed along the lower boundary of the CSR envelope (**Fig. 2.5b, 2.6b**). This, along with the lack of small nearest-neighbour distances and MAD test results (**Fig. S2.2 and Table S2.2, Appendix A**), suggests intermediate patterns. Conversely, site KM93, the only site that developed in organic material, is the only site that closely follows the theoretical curve of CSR, shows a clear predominance of small nearest-neighbour distances, and has the largest p-value (0.6) accepting CSR in the MAD test (**Fig. S2.2 and Table S2.2, Appendix A)**, revealing a random pattern throughout the SPPA. Therefore, the spatial pattern of polygons in TTP seems to be influenced by the nature of the substrate rather than its age.

2.5.2. Development stage of ice-wedge polygons and relationship with morphometry

IW cycle trough different stages (developing, degrading and stabilizing), and the surface expression of IW polygons may vary with these stages (Liljedahl et al., 2016; Kanevskiy et al., 2017; Matthews et al., 1998). Therefore, the development stage of IW polygons can potentially be inferred by examining their morphometry. This study selected six IW polygons sites that revealed different stages of development based on vegetation composition, wetness and polygon topography. Polygons at site KM93 are in the development stage as they are characterized by low- and high-centered polygons with narrow troughs (e.g., Liljedahl et al., 2016). Polygons at sites KM92 and BR1 are likely in a degrading stage as they are characterized by dry high-centered polygons with wide wet troughs (**Fig. 2.4c, 2.6a**). In places, trough ponds are colonized by mosses and graminoids (**Fig. 2.4d**), which are water-tolerant plants associated with the initial stage of degradation (e.g., Jorgenson et al., 2015). Polygons at site KM95, BR2 and BR3 are likely in the stabilization stage. These three sites exhibit very wet IW intersections, which is consistent with the initial stage of stabilization, where surface water is still being redistributed from the troughs to the intersections resulting in troughs to become better drained and vegetation composition to change (e.g., Jorgenson et al., 2015). KM95 is located in medium to fine-grained alluvium and is characterized by wide troughs dominated by mosses and lichens and wet polygons intersections, some of which are characterized by bare soil and graminoids (**Fig. 2.4c**). The hypothesis for site KM95 being in the stabilization stage is also supported by the presence of ice lenses and very organic-rich soil deep in the trough discovered while coring in June 2019 (**Fig. S2.1, Appendix A**), which is indicative of permafrost aggradation with the recovery of the intermediate layer (e.g., Kanevskiy et al., 2017). BR2 and BR3 have wide troughs that appear reddish with some bright green spots and also present wet troughs intersections, which indicates that the IW are also in the initial stabilization stage, with surface water being concentrated at the intersections and trough vegetation being characterized by water-tolerant plants such as graminoids, lichens and mosses (e.g., Jorgenson et al., 2015).

Despite the sites showing different developmental stages, their morphometry is statistically similar (except for site BR3) (**Table 2.1**). This suggests that the evolution of polygons through the different stages may not always influence the morphometric characteristics of polygons. However, we hypothesise that the different stages of development are associated with the regularity of the polygons network. Indeed, the developing site (KM93) has a random pattern according to the SPPA, the degrading sites (KM92 and BR1) have an intermediate pattern, and the stabilizing sites (KM95, BR2 and BR3) have a regular pattern.

2.5.3. Ground ice content and implications for degradation of ice-wedge polygons

The most important factor in investigating landscape change in permafrost region is ground ice content, specifically the occurrence of excess ice. Wedge-ice is estimated to occupy c. 8-22%vol of the uppermost 3 m of polygonal terrain in the TTP, depending on the IW width. Although no validation data exists for our six test sites, our coring in polygonal troughs within the East Blackstone river valley confirmed the presence of IW at two of three sites (exceeded coring depth at KM95) and our observations in gullies and headwalls of thaw slumps also confirmed the presence of IW in polygonal terrain. Moreover, the estimated wedge-ice volume represents a minimum value because late Pleistocene-age IW are truncated 3-4 m below the surface with no evidence of surface polygons (e.g., Grinter et al., 2019). At these sites, the accumulation of colluvium since the mid-Holocene buried the older IW and a new set of IW developed (St-Jean et al., 2011; Grinter et al., 2019). The burial of IW polygons in older landscapes was also observed at Prudhoe Bay on the Arctic Coastal Plain close to the Beaufort Sea coast of Alaska, where IW were found in the center of polygons and attributed to earlier generations of IW development (Kanevskiy et al., 2017). Additionally, surface expression of IW in TTP are generally restricted to flat terrain, but IW can also occur on hillslopes without resulting in polygonal patterns (e.g., Mackay, 1990, 1995). IW polygons can also be hidden by dense vegetation, or where IW are inactive (Morse and Burn, 2013, Kokelj and Burn, 2004). Therefore, while the method of tundra polygon delineation to estimate wedge-ice volume can be effective in low-lying tundra terrain with active IW development, it may become limited in older landscapes where polygonization becomes obscured by downslope mass transport and colluviation or in densely vegetated regions.

In TTP, other types of massive ground ice have been discovered in the permafrost. For example, buried bodies of glacial ice were observed in headwall of thaw slumps (Lacelle et al., 2007, 2009) and pingos are located in the Blackstone River valley. The presence of thermokarst lakes scattered in the lowlands also provides evidence that permafrost is most likely ice-rich. The occurrences of massive ice bodies however appear to have limited distribution and therefore IW likely represent the main type of massive ice in TTP, most of which are located in valley bottoms. Degradation of IW has been occurring in TTP as evidenced by wetting and gullying along polygon troughs. Thermal erosion of the near-surface IW network can also enhance the melting of buried IW and cause collapse of the ground surface. The IW polygons in TTP have high organic matter contents (**Fig. S2.1, Table S2.1, Appendix A**), and depending on the composition of the organic carbon (e.g., Schmidt et al., 2011), the degradation of IW and collapse of polygons centers would redistribute the organic matter and make labile organic carbon previously trapped in permafrost available for biodegradation.

2.6 Conclusion

Based on the results presented in this study, the following conclusions can be reached:

1. IW polygons in the mountainous TTP are found preferentially in woody sedge peat, glaciofluvial and alluvial deposits along the lower reaches of the Blackstone and East Blackstone rivers; between elevations of 995-1045 and 1065-1135 m and; on hillslopes of ≤1°. The distribution of IW polygons is constrained by hillslope processes and the hydrological network and restricted to low-gradient slopes with mid-Holocene deposits the accumulated in the fluvial plains of the lower reaches of the Blackstone and East Blackstone rivers.
2. Vegetation type, surface wetness, and polygon spatial pattern analysis are influenced by the development stage of IW polygons, while the size and angles of polygons seem independent of the development stage. Additionally, the spatial pattern of polygons in TTP seems to be more closely influenced by the nature of the substrate than by its age, while the size of the polygons is more closely influenced by the age of the substrate.
3. Estimation of wedge-ice content can be inferred from delineation of the centerlines of polygons troughs, but it might be limited to flat tundra terrain since IW on hillslopes do not result in polygonal pattern, and these patterns can be obscured by vegetation and IW inactivity. Wedge-ice content estimation based on remote sensing of the surface expression of IW are therefore most likely underestimated, especially in mountainous and densely vegetated areas, or where IW are inactive.

2.7 Acknowledgements

This work was supported by Natural Sciences and Engineering Research Council of Canada (NSERC) Discovery Grants with logistical support provided by NSERC Northern Supplement, and the Northern Scientific Training Program. We thank Y. Wang for valuable field assistance. Fieldwork was performed under the Yukon Scientists and Explorers Act Licence No. 6800-20-1147, Yukon Park Permit No. 19-RE-TP-06 and with approval from the Tr'ondek Hwech'in government. We also thank M. Kanevskiy and an anonymous reviewer for their constructive comments on the manuscript.

2.8 Supporting Information

Data is available in supplementary material, included in Appendix A.

Figure S2.1. Photographs of permafrost cores taken from a trough at the three East Blackstone River valley sites.

Table S2.1. Gravimetric water, organic matter and carbonates content results from permafrost cores taken in one centre and one trough at the three East Blackstone River valley sites.

Figure S2.2 Histograms of nearest-neighbour distances of six ice-wedge polygons sites in Tombstone Territorial Park, central Yukon, Canada

2.9 References

Abolt CJ, Young MH, Atchley AL, Harp DR. Microtopographic control on the ground thermal regime in ice wedge polygons. *Cryosphere*. 2018. doi:10.5194/tc-12-1957-2018

Abolt CJ, Young MH. High-resolution mapping of spatial heterogeneity in ice wedge polygon geomorphology near Prudhoe Bay, Alaska. *Sci Data*. 2020. doi:10.1038/s41597-020-0423-9

Baddeley A, Turner R. spatstat : An R Package for Analyzing Spatial Point Patterns. *J Stat Softw*. 2005;12(6). doi:10.18637/jss.v012.i06

Baddeley, Adrian, Peter J. Diggle, Andrew Hardegen, Thomas Lawrence, Robin K. Milne, and Gopalan Nair. On Tests of Spatial Pattern Based on Simulation Envelopes. *Ecological Monographs,* 2014; 84(3): 477–89. doi: 10.1890/13-2042.1.

Bernard-Grand'Maison C, Pollard W. An estimate of ice wedge volume for a High Arctic polar desert environment, Fosheim Peninsula, Ellesmere Island. *Cryosphere*. 2018. doi:10.5194/tc-12-3589-2018

Camels F, Roy LP, Grandmont K and Pugh R. *A summary of climate- and geohazard-related vulnerabilities for the Dempster Highway corridor*. Yukon Research Centre, Yukon College, 2018;204 p.

Christiansen HH. Thermal regime of ice-wedge cracking in Adventdalen, Svalbard. *Permafr Periglac Process*. 2005;16(1):87-98. doi:10.1002/ppp.523

Couture NJ, Pollard WH. Modelling geomorphic response to climatic change. *Clim Change*. 2007;85(3-4):407-431. doi:10.1007/s10584-007-9309-5

de Jongh, MC, van Lieshout, MNM. Testing biodiversity using inhomogeneous summary statistics and global envelope tests. *Spatial Statistics*. 2022;50:100607. doi:10.1016/j.spasta.2022.100607

Diggle PJ. On Parameter Estimation and Goodness-of-Fit Testing for Spatial Point Patterns. *Biometrics*. 1979. doi:10.2307/2529938

Diggle PJ. *Statistical Analysis of Spatial and Spatio-Temporal Point Patterns, Third Edition*.; 2013. doi:10.1201/b15326

Duk-Rodkin A. Surficial geology, Dawson, Yukon Territory, 1:250,000. 1996.

Dutilleul P, Haltigin TW, Pollard WH. Analysis of polygonal terrain landforms on Earth and Mars through spatial point patterns. *Environmetrics*. 2009. doi:10.1002/env.924

Environment Canada. Canadian Climate Normals 1981-2010 Station Data. http://climate.weather.gc.ca. Published 2010. Accessed February 23, 2016.

Etzelmüller B, Ødegård RS, Berthling I, Sollid JL. Terrain parameters and remote sensing data in the analysis of permafrost distribution and periglacial processes: principles and examples from southern Norway. *Permafr Periglac Process*. 2001;12(1):79-92. doi:10.1002/ppp.384

Fortier D, Allard M, Shur Y. Observation of rapid drainage system development by thermal erosion of ice wedges on Bylot Island, Canadian Arctic Archipelago. *Permafr Periglac Process*. 2007;18(3):229-243. doi:10.1002/ppp.595

Fortier D, Allard M. Late Holocene syngenetic ice-wedge polygons development, Bylot Island, Canadian Arctic Archipelago. *Can J Earth Sci*. 2004;41(8):997-1012. doi:10.1139/e04-031

Fraser R, Kokelj S, Lantz T, McFarlane-Winchester M, Olthof I, Lacelle D. Climate Sensitivity of High Arctic Permafrost Terrain Demonstrated by Widespread Ice-Wedge Thermokarst on Banks Island. *Remote Sens*. 2018;10(6):954. doi:10.3390/rs10060954

French HM, Heginbottom JA (eds.). *Guidebook to permafrost and related features of the Northern Yukon Territory and Mackenzie Delta, Canada*. Alaska Division of Geological & Geophysical Surveys, 1983;Guidebook 3:186 p. doi: 10.14509/265

French HM. *The Periglacial Environment: Third Edition*.; 2013. doi:10.1002/9781118684931

Gagnon S, Allard M. Changes in ice-wedge activity over 25 years of climate change near Salluit, Nunavik (northern Québec, Canada). *Permafr Periglac Process*. 2020. doi:10.1002/ppp.2030

Gogineni P, Romanovsky V, Cherry J, et al. *Opportunities to Use Remote Sensing in Understanding Permafrost and Related Ecological Characteristics: Report of a Workshop*. Washington D.C.: National Academy of Science; 2014.

Green LH. *Geology of Nash Creek, Larsen Creek, and Dawson Area Maps.* Ottawa: Geological Survey of Canada, Memoir 364; 1972.

Grinter M, Lacelle D, Baranova N, Murseli S, Clark ID. Late Pleistocene and Holocene ice-wedge activity on the Blackstone Plateau, central Yukon, Canada. *Quat Res*. 2019;91:179-193.

Haltigin T, Pollard W, Dutilleul P. Comparison of ground- and aerial-based approaches for quantifying polygonal terrain network geometry on Earth and Mars via spatial point pattern analysis. *Planet Space Sci*. 2010. doi:10.1016/j.pss.2010.08.008

Hu X, Pollard W. The Hydrologic Analysis and Modelling of River Icing Growth, North Fork Pass, Yukon Territory, Canada. *Permafrost and Periglacial Processes*, 1997;8(3): 279–294. doi: 10.1002/(SICI)1099-1530(199709)8:3<279::AID-PPP260>3.0.CO;2-7

Jorgenson MT, Kanevskiy M, Shur Y, et al. Role of ground ice dynamics and ecological feedbacks in recent ice wedge degradation and stabilization. *J Geophys Res F Earth Surf*. 2015. doi:10.1002/2015JF003602

Jorgenson MT, Shur Y, Kanevskiy MZ, Grunblatt J, Michaelson G, Ping C-L. Permafrost database development, characterization, and mapping for northern Alaska. *US Fish Wildl Serv*. 2014. doi:10.1145/3132847.3132886

Jorgenson TM, Harden J, Kanevskiy M, et al. Reorganization of vegetation, hydrology and soil carbon after permafrost degradation across heterogeneous boreal landscapes. *Environ Res Lett*. 2013. doi:10.1088/1748-9326/8/3/035017

Kanevskiy M, Shur Y, Jorgenson MT, et al. Ground ice in the upper permafrost of the Beaufort Sea coast of Alaska. *Cold Reg Sci Technol*. 2013;85:56-70. doi:10.1016/j.coldregions.2012.08.002

Kanevskiy M, Shur Y, Jorgenson T, et al. Degradation and stabilization of ice wedges: Implications for assessing risk of thermokarst in northern Alaska. *Geomorphology*. 2017. doi:10.1016/j.geomorph.2017.09.001

Koch, J.C., Jorgenson, M.T., Wickland, K.P., Kanevskiy, M. & Striegl, R. 2018. Ice Wedge Degradation and Stabilization Impact Water Budgets and Nutrient Cycling in Arctic Trough Ponds. *Journal of Geophysical Research: Biogeosciences* 123 : 2604–2616. doi: 10.1029/2018JG004528

Kokelj SV, Burn CR. Tilt of Spruce Trees near Ice Wedges, Mackenzie Delta, Northwest Territories, Canada. *Arctic, Antarctic, and Alpine Research*, 2004;36(4):615-623. doi: 10.1657/1523-0430(2004)036[0615:TOSTNI]2.0.CO;2

Lacelle D, Lauriol B, Clark ID, Cardyn R, Zdanowicz C. Nature and origin of a Pleistocene-age massive ground-ice body exposed in the Chapman Lake moraine complex, central Yukon Territory, Canada. *Quat Res*. 2007;68(2):249-260. doi:10.1016/j.yqres.2007.05.002

Lacelle D, St-Jean M, Lauriol B, et al. Burial and preservation of a 30,000 year old perennial snowbank in Red Creek valley, Ogilvie Mountains, central Yukon, Canada. *Quat Sci Rev*. 2009;28(27-28):3401-3413. doi:10.1016/j.quascirev.2009.09.013

Lachenbruch AH. Mechanics of thermal contraction cracks and ice-wedge polygons in permafrost. *Geol Soc Am Spec Pap*. 1962;70:1-66. doi:10.1016/0378-7788(86)90031-9

Liljedahl AK, Boike J, Daanen RP, et al. Pan-Arctic ice-wedge degradation in warming permafrost and its influence on tundra hydrology. *Nat Geosci*. 2016;9(4):312-318. doi:10.1038/ngeo2674

Mackay JR. Ice wedges on hillslopes and landform evolution in the late Quaternary, western Arctic coast, Canada. *Can J Earth Sci*. 1995. doi:10.1139/e95-091

Mackay JR. *Ice-wedges as Indicators of Recent Climatic Change, Western Arctic Coast. Paper 76-1A.*; 1976.

Mackay JR. Some observations on the growth and deformation of epigenetic, syngenetic and anti-syngenetic ice wedges. *Permafr Periglac Process*. 1990;1(1):15-29. doi:10.1002/ppp.3430010104

Mackay JR. Thermally induced movements in ice-wedge polygons, western arctic coast: a long-term study. *Géographie Phys Quat*. 2000;54(1):41. doi:10.7202/004846ar

Makaske, B. Anastomosing rivers: a review of their classificaiton, origin and sedimentary products. *Earth-Science Reviews.* 2001;53(3-4):149-196. doi: 10.1016/S0012-8252(00)00038-6

Matthews JA, Shakesby RA, Berrisford MS, McEwen LJ. Periglacial patterned ground on the Styggedalsbreen glacier foreland, Jotunheimen, southern Norway: Micro-topographic, paraglacial and geoecological controls. *Permafr Periglac Process*. 1998. doi:10.1002/(SICI)1099-1530(199804/06)9:2<147::AID-PPP278>3.0.CO;2-9

Michel FA. Isotope geochemistry of frost-blister ice, North Fork pass, Yukon, Canada. *Can J Earth Sci*. 1986. doi:10.1139/e86-054

Morse PD, Burn CR. Field observations of syngenetic ice wedge polygons, outer Mackenzie Delta, western Arctic coast, Canada. *J Geophys Res Earth Surf*. 2013;118(3):1320-1332. doi:10.1002/jgrf.20086

Pewe TL. Ice wedges in Alaska; classification, distribution, and climatic significance. In: *Proceedings Permafrost International Conference*. National Academy of Science; 1963:76-81.

Plug, LJ, Werner, BT. Fracture Networks in Frozen Ground. *Journal of Geophysical Research: Solid Earth*, 2001;106(B5):8599-613. doi:10.1029/2000JB900320.47. Haltigin TW, Pollard WH, Dutilleul P, Osinski GR. Geometric Evolution of Polygonal Terrain Networks in the Canadian High Arctic: Evidence of Increasing Regularity over Time. *Permafr Periglac Process*. 2012. doi:10.1002/ppp.1741

Schmidt MWI, Torn MS, Abiven S, et al. Persistence of soil organic matter as an ecosystem property. *Nature*. 2011;478(7367):49-56. doi:10.1038/nature10386

Schuur, E.A.G., Vogel, J.G., Crummer, K.G., Lee, H., Sickman, J.O. & Osterkamp, T.E. 2009. The effect of permafrost thaw on old carbon release and net carbon exchange from tundra. *Nature* 459 : 556–559. DOI: 10.1038/nature08031

Smith SL, Romanovsky VE, Lewkowicz AG, et al. Thermal state of permafrost in North America: A contribution to the international polar year. *Permafr Periglac Process*. 2010;21(2):117-135. doi:10.1002/ppp.690

Steedman AE, Lantz TC, Kokelj S V. Spatio-Temporal Variation in High-Center Polygons and Ice-Wedge Melt Ponds, Tuktoyaktuk Coastlands, Northwest Territories. *Permafr Periglac Process*. 2017. doi:10.1002/ppp.1880

St-Jean M, Lauriol B, Clark ID, Lacelle D, Zdanowicz C. Investigation of ice-wedge infilling processes using stable oxygen and hydrogen isotopes, crystallography and occluded gases (O2, N2, Ar). *Permafr Periglac Process*. 2011;22(1):49-64. doi:10.1002/ppp.680

Ulrich M, Grosse G, Strauss J, Schirrmeister L. Quantifying Wedge-ice volumes in Yedoma and thermokarst basin deposits. *Permafr Periglac Process*. 2014;25(3):151-161. doi:10.1002/ppp.1810

Van Lieshout MNM, Baddeley AJ. A non-parametric measure of spatial interaction in point patterns. *Adv Appl Probab*. 1996. doi:10.1017/s0001867800048345

Zhang W, Liljedahl AK, Kanevskiy M, et al. Transferability of the Deep Learning Mask R-CNN Model for Automated Mapping of Ice-Wedge Polygons in High-Resolution Satellite and UAV Images. *Remote Sens*. 2020;12(7):1085. doi:10.3390/rs12071085

Zhang W, Witharana C, Liljedahl AK, Kanevskiy M. Deep convolutional neural networks for automated characterization of arctic ice-wedge polygons in very high spatial resolution aerial imagery. *Remote Sens*. 2018. doi:10.3390/rs10091487

Zimov, S.A., Davydov, S.P., Zimova, G.M., Davydova, A.I., Schuur, E.A.G., Dutta, K. & Chapin, I.I.I.S. 2006. Permafrost carbon: Stock and decomposability of a globally significant carbon pool. *Geophysical Research Letters* 33 : 1–5. DOI: 10.1029/2006GL027484

CHAPTER 3: LANDSCAPE CHANGES IN THE TOMBSTONE TERRITORIAL PARK REGION (CENTRAL YUKON, CANADA) FROM MULTI-LEVEL REMOTE SENSING ANALYSIS

Abstract

Northern ecosystems are vulnerable to surface disturbances caused by warming climate and human activities. The Ogilvie Mountains in central Yukon are an important region that should be monitored, as it is a major transportation corridor connecting northern communities. This study aims to characterize 35 years of landscape changes in the Tombstone Territorial Park and the surrounding region of the Ogilvie Mountains by detecting and interpreting landscape changes using a Landsat-derived trend analysis and multi-level image interpretation. Statistically significant spectral changes occurred in 24% of the study area between 1986 and 2021, and most of these changes are gradual and associated with vegetation succession and hydrological processes (i.e., erosion and deposition). Other landscape changes included wildfires, slumps, changes to riverbanks and lake shores, earlier melting of icings in the summer, degradation on the peripheries of some ice-wedge polygonal terrain, and potential insect damage to forests. Our investigation reveals that the extent and magnitude of landscape changes in the study area are influenced by climate, geomorphic setting, ecological succession, and glacial history of the region. Given a varied combination of ecotypes, spatial and temporal variations are to be expected in terms of the response of the landscape to climate and anthropogenic disturbances.

3.1 Introduction

Northern ecosystems are vulnerable to surface disturbances caused by warming climate and anthropogenic activities such as changes in moisture and temperature patterns, wildfire regimes or land use (Arctic Monitoring and Assessment Programme (AMAP), 2017). These disturbances can lead to a series of feedbacks that may affect the surface energy balance, the ground thermal regime, and possibly the stability of permafrost (Jorgenson et al., 2010). Following a surface disturbance, ice-rich permafrost environments may experience thermokarst, which can lead to changes in micro-topography, hydrology, and vegetation cover (Farquharson et al., 2019; Jorgenson et al., 2013; M T Jorgenson et al., 2015; Liljedahl et al., 2016; Osterkamp et al., 2009). For example, the melting of ice wedges across uplands of Banks Island in the Canadian Arctic has led to increased micro-relief and the formation of thaw ponds (Fraser et al., 2018). On the Alaska North Slope, tundra fires have led to permafrost thaw-induced subsidence, which was greatest in ice-rich areas, and associated with significant increase in micro-topography following ice wedge degradation (Jones et al., 2015). The changes following surface disturbances represent substantial challenges for infrastructure, economy, health, food security and traditional usage of the landscape (Council of Canadian Academies, 2014; Hjort et al., 2022, 2018; Hovelsrud et al., 2011; Wesche and Chan, 2010; White et al., 2007).

With the emergence of long-term remote sensing data archives and improvements in their spatial resolution, monitoring landscape changes associated with permafrost degradation can be undertaken at local to regional scales (Nitze et al., 2018). The Landsat series of satellites provide the longest continuous satellite imagery record (1985-present) at a medium spatial resolution (30 m) and various spectral indices have been developed to capture surface changes. Trend analysis of the Tasseled Cap (TC) transformation applied to a Landsat imagery time-series can detect changes related to vegetation (greenness index), surface condition (brightness index) and soil and canopy moisture (wetness index) following permafrost degradation (e.g., Brooker et al., 2014; Campbell et al., 2021; Fraser et al., 2011, 2012; Nitze et al., 2017; Nitze and Grosse, 2016; Olthof and Fraser, 2014; Raynolds and Walker, 2016). While the spatial resolution of Landsat data may present limitations for identifying surface disturbances, when used in combination with multi-scale, multi-sensor remote sensing analyses, the identification of disturbances and landscape change can be improved (Carroll et al., 2016; Jones et al., 2021; National Research Council, 2014; Nitze et al., 2018; Short et al., 2011; van der Sluijs et al., 2018).

The Ogilvie Mountains in central Yukon contain both Pleistocene and Holocene-age permafrost (Grinter et al., 2019; Lacelle et al., 2007). Previous studies identified the region to be sensitive to climate change as it contains evidence of ice-rich permafrost, notably through the presence of ice-wedge polygons (Frappier and Lacelle, 2021) and other types of massive ice (Lacelle et al., 2009, 2007). The area is also an important traditional territory of the Tr'ondëk Hwëch'in First Nation, who co-administers the Tombstone Territorial Park (TTP) that protects the natural, historical and cultural resources of the area under the TTP Management Plan (Yukon Parks, 2009). Signs of permafrost degradation have been observed along the Dempster Highway that runs through the park, notably gullying and ponding along high-centered polygons troughs and thaw slumping (Lacelle et al., 2007, 2009; Grinter et al., 2019; Calmels et al., 2018). However, little is known about the state of landscape change throughout the region. This study aims to detect landscape changes in the TTP and the surrounding region of the Ogilvie Mountains using a multi-level remote sensing analysis. The goals are to: 1) identify changes in the study area using Landsat-based Tasseled Cap (TC) trend analysis, 2) interpret these changes based on visual representation of the TC indices trends portrayed as red-green-blue (RGB) images, interpretation of TC indices timeseries, classification of change and multi-level image interpretation, and 3) relate these changes to the geomorphic setting, ecology and glacial history of the area.

3.2 Study area

The study area is in the Ogilvie Mountains in central Yukon. It includes the TTP and extends tens of kilometers to the north and south of the park boundaries (**Fig. 3.1**). The Dempster Highway, built in the 1970s, is a north-south road linking Dawson (50 km south of TTP) and Inuvik (615 km north of TTP). Elevation in the study area varies between 416 and 2344 m a.s.l., with >95% being above 800 m a.s.l. The area is dissected by four main north-south oriented river valleys: the Chandindu and North Klondike Rivers flowing to the south; the Blackstone and East Blackstone Rivers flowing northward and merging at the northern boundary of TTP, near Chapman Lake. Surficial deposits in the TTP are dominated by Holocene colluvium (ca. 80%) and Late Pleistocene glacial deposits (ca. 15%) that include over 20-m thick moraine plains and hummocky, ridged and hilly till complexes from the McConnell and Reid glaciation; Holocene alluvial plains deposits (ca. 5%) in the river valleys are characterized by 0-12 m thick coarse sand and gravel with minor silt and fine sand (Duk-Rodkin, 1996).

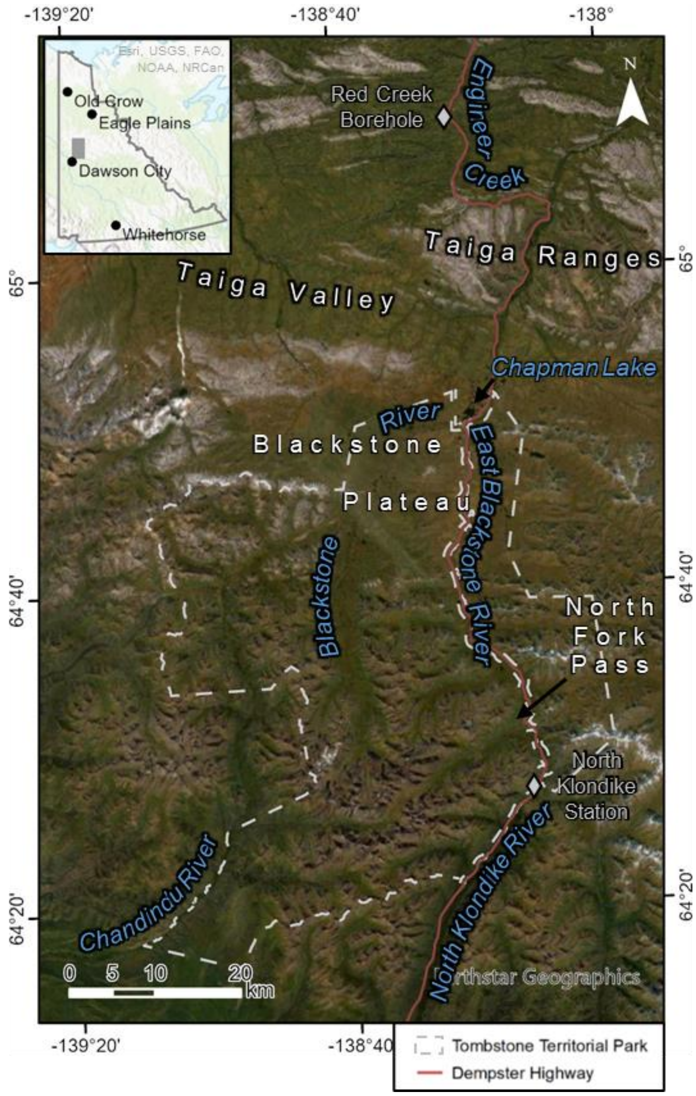

Figure 3.1 Study area location map (shaded grey on inset map).

Vegetation consists mostly of alpine tundra with scattered patches of stunted black spruce (*Picea mariana*) and dwarf birch (*Betula nana*) and willow (*Salix spp.*) above the treeline (c. 535-1450 m a.s.l) and along the shorelines of rivers and lakes (Smith et al., 2004). Grassland tundra (34.4%), barren land (23.5%) and shrubland tundra (18%) are the prevalent landcover types, while the rest of the landscape is made up mainly of needleleaf forest (9%), mixed forest (7.3%), grassland-lichen-moss tundra (2.9%) and shrubland-lichen-moss tundra (2.6%) (Latifovic et al., 2017) (**Fig. 3.2**).

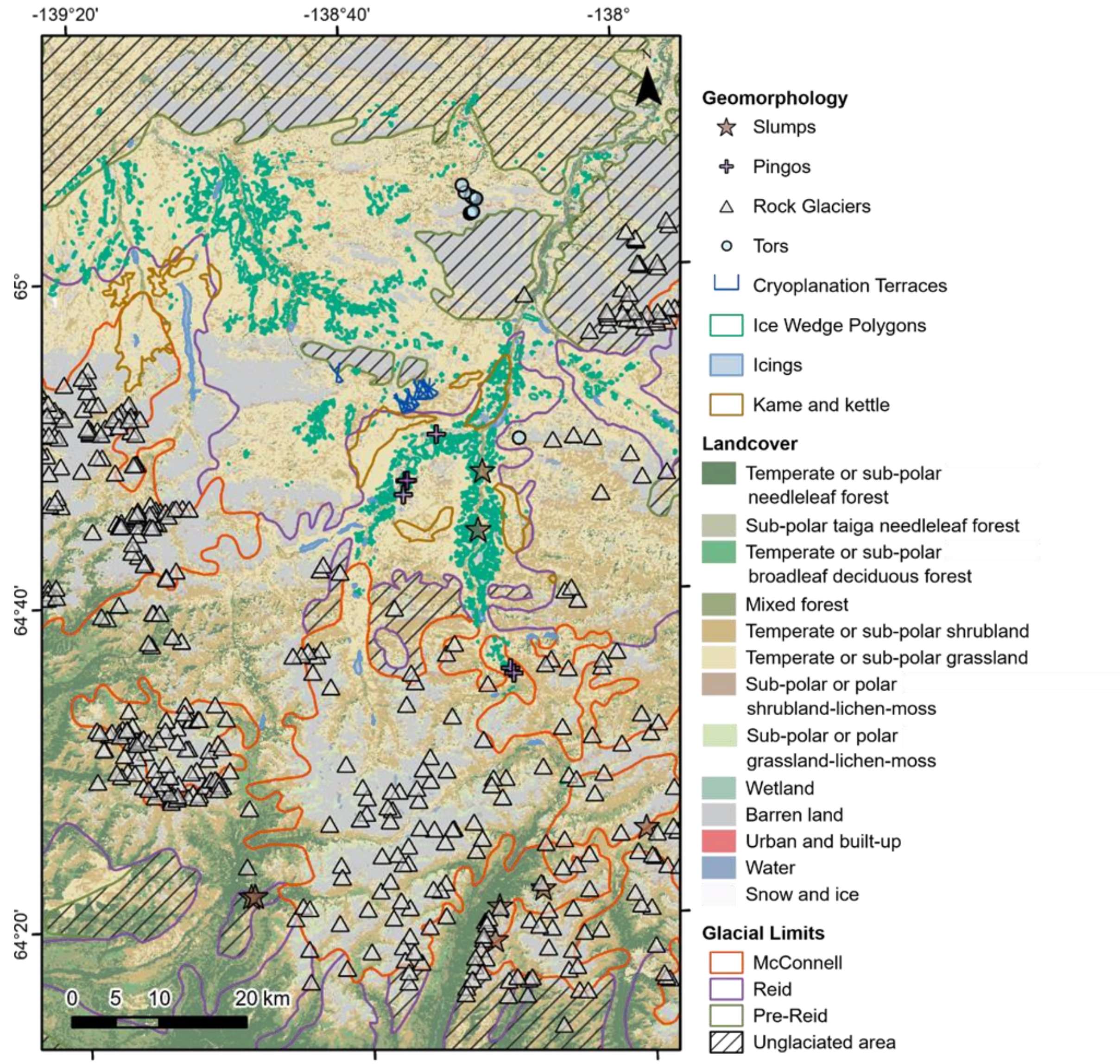

Figure 3.2 Geomorphology, landcover units and glacial limits of the study area. Data sources: Pingos, rock glaciers and cryoplanation terraces: Page, 2009, Thomas and Rampton, 1982; Ice Wedge Polygons: Frappier and Lacelle, 2021; Icings: Crites, Kokelj and Lacelle, 2020; Landcover: 30-m Land Cover of North America (Latifovic, Pouliot and Olthof, 2017); Glacial Limits: Duk-Rodkin, 1996. Slumps, rock glaciers, ice-wedge polygons and kame and kettle topography were identified using high-resolution satellite imagery (WorldView-2).

The region is in the continental subarctic climate zone and is characterized by short cool summers and long cold winters. Weather data from the Dawson City meteorological station (50 km south of TTP) reports a mean annual air temperature of −3.9°C for the 1986-2021 period (mean January temperature: −25.8°C; mean July temperature: 15.8°C). The meteorological data shows a non-significant increase in mean annual air temperatures of 0.6°C over the period of record (slope: 0.03C°/year, p-value: 0.2), with a warming occurring mostly in winter (mean January temperatures increased by 2.6°C (slope: 0.1C°/year, p-value: 0.2); mean July temperatures shows no trend (slope: 0.01C°/year, p-value: 0.5)) (**Fig. 3.3a**). Precipitation data is sparse and only extends to 2015. An average of 319 mm of total precipitation with c. 54% falling as snow is reported at Dawson City for the 1986-2015 period; Total rainfall shows a small non-significant increase during the 1986-2015 period (slope: 0.3 mm/year, p-value: 0.8), and total snowfall shows non-significant decrease (slope: −1.8 mm/year, p-value: 0.2) (**Fig. 3.3b**). Residual plots for temperature

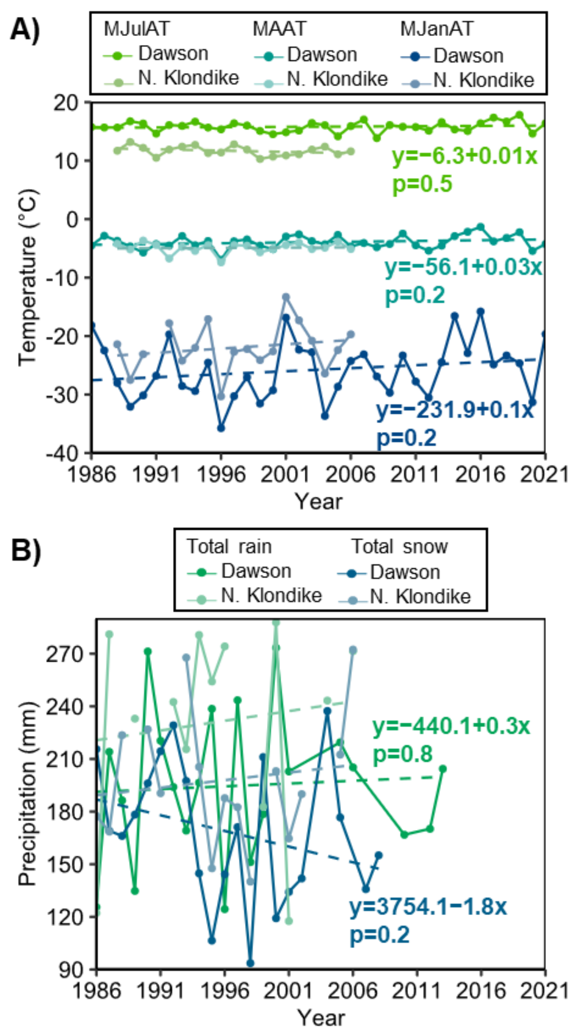

Figure 3.3 A) Mean July Air Temperatures (MJulAT), Mean Annual Air Temperatures (MAAT) and Mean January Air Temperatures (MJulAT), and **B)** Total snow and rain precipitation at the Dawson City and North Klondike River weather stations, Yukon Territory. Data from Climate Change and Environment Canada retrieved using the "weathercan" R package (LaZerte and Albers (2018).

and precipitation linear regression models are provided in Appendix B (**Fig. S3.1 to S3.10**) Snow depth measurements made in TTP in March 2022 revealed that snow accumulation is lower

(x̄=37.7 ±16.6 cm, n=60) in the grassland tundra and barren land, but is higher in the Taiga Ranges north of TTP (x̄=93.1 ± 9 cm, n=10) and in the shrubland tundra and mixed forest south of North Fork Pass (x̄=105.7 ± 11.4 cm, n=20).

The cooler climate of the high elevations and the tundra vegetation ensure that permafrost is continuous, at least in the valleys north of North Fork Pass. Based on the presence of buried glacial ice, permafrost has persisted, at least locally, since the late Pleistocene (Lacelle et al., 2009, 2007). Most of the region has been ice-free since the late Pleistocene (McConnell Glaciation), and some of the areas north of the region remained unglaciated since at least the mid-Pleistocene (Reid Glaciation) (**Fig. 3.2**). Ground temperatures recorded along the Dempster Highway in 2016-2017, between North Fork Pass and c. 10 km north of Chapman Lake, showed values ranging between −3 and 0°C, with a mean of −1.8°C (Calmels et al., 2018). At Red Creek (c. 775 m a.s.l), 35 km north of TTP, an average ground temperature of −2°C was recorded at 7 m below the surface in 2008 (Lacelle et al., 2009).

Many permafrost-related landforms are present in the study area. Ice-wedge polygons occupy 2.6% of TTP and are found along the lower reaches of the Blackstone and East Blackstone rivers on hillslopes ≤1° (Frappier and Lacelle, 2021) as well as along the smaller tributaries of the Ogilvie River in the Taiga Valley. Solifluction lobes are present on almost all mountain slopes in the area. Rock glaciers (n=389) are present in the barren lands and grassland-lichen-moss. Icings (n=32) occur mostly along high-degree braided river channels (62.5%, n=20), as well as along smaller tributary streams (15.6%, n=5), on hillslopes (12.5%, n=4), or along low-degree braided river channels (9.4%, n=3). Eight thaw slumps developed in the southern part of the area and along the Dempster Highway. Pingos (n=6) are found in drained lake bottoms and along migrated streams. Active layer detachment slides, thaw lakes, and seasonal frost mounds are also scattered across the area. Cryoplanation terraces are found on the highly elevated Blackstone Plateau (Page, 2009). Finally, a kame and kettle topography is also identified on the Blackstone Plateau and in the Taiga Valley and corresponds with the glacial limits of the McConnell and Reid glaciations (Duk-Rodkin, 1996).

3.3 Methods

3.3.1. Imagery acquisition

Landsat 5 TM, Landsat 7 ETM+ and Landsat 8 OLI images (Tier 1 Level 1 Top-of-Atmosphere (TOA) reflectance) were acquired from USGS Earth Explorer (https://earthexplorer.usgs.gov/) based on selection criteria including coverage (WRS-2 paths 63-64 and rows 14-15), low cloud cover (manual verification of clouds in study area) and peak summer growing season (June-August). The mountains and high elevation of the area leads to frequent cloud cover, but we were able to extract imagery matching the criteria from a total of 11 years between 1986 and 2021 (**Fig. 3.4a**), with acquisition dates from June 10th to August 31st. A plot of the acquisition dates shows that no bias in spectral reflectance should be introduced due to the phenological cycles (**Fig. 3.4b**). The Landsat images are radiometrically calibrated and orthorectified using ground control points and Digital Elevation Models (U.S. Geological Survey, 2016). However, some years showed a displacement, so the stack was georeferenced to the most recent image using a zero-order polynomial transformation shift in Esri ArcGIS Pro. Clouds and cloud shadows were masked from the images using the quality assessment pixel band (U.S. Geological Survey, 2020). Manual editing of the masks was also performed in Esri ArcGIS Pro to ensure quality of masking. Ice, icings, and snow were retained to assess potential changes in summer melting of these features.

Historical aerial photographs (1:30000 scale) were also obtained from the Canada National Air Photo Library and were available for the years 1963, 1977, 1989 and 2000. High-resolution satellite imagery were acquired from the WorldView-2 (0.5 m resolution: 2009, 2012; 2020) and the PlanetScope (3 m resolution: 2019) satellites.

3.3.2. Landscape change detection

The Tasseled Cap (TC) transformation method consists of three indices: brightness (TCB) which represents total soil reflectance, greenness (TCG) which captures vegetation's spectral signature, and wetness (TCW) which is sensitive to soil and canopy moisture (Crist and Cicone, 1984). The TC indices were calculated for the stack of Landsat TOA reflectance images using ArcPy in Esri ArcMap and the coefficients from Huang et al. (2002). Transformation functions were first applied to the Landsat 8 (OLI) TOA reflectance products before applying the TC coefficients to ensure continuity between the Landsat imagery (Roy et al., 2016). The three indices were plotted against time for 60 random pixels representing developed areas (road, campground, active quarries), assuming that this type of surface cover has remained stable in terms of reflectance throughout the study period (**Fig. 3.4c**). The Shapiro-Wilk test for normality was performed and showed that yearly means could be used to asses the indices stability through time. Linear regression analysis of the means shows that only small, non-significant biases towards brightness (TCB) decrease (slope: −0.6, p-value: 0.32), greenness (TCG) decrease (slope: −0.8, p-value: 0.6) and wetness (TCW) increase (slope: 0.4, p-value: 0.21) could have been introduced in the analysis.

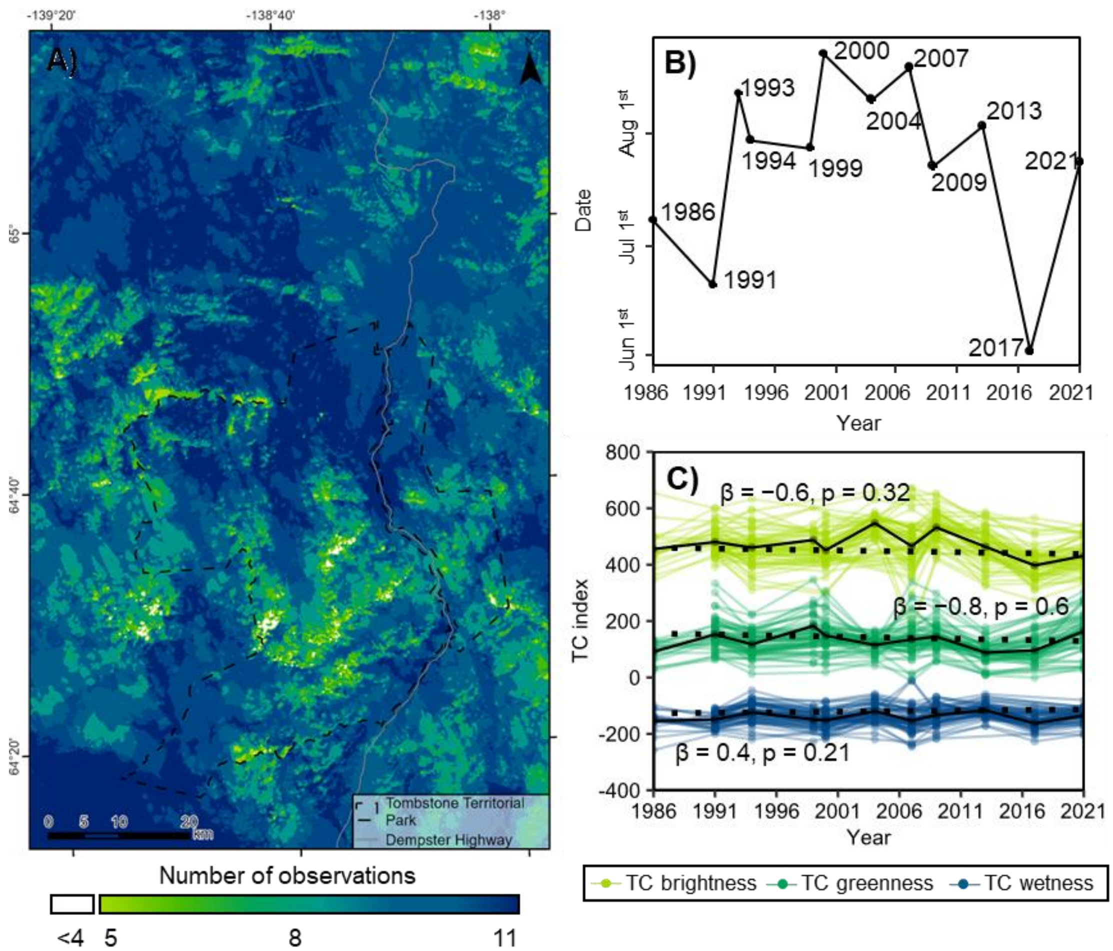

Figure 3.4 A) Number of Landsat peak growing season, cloud-masked pixels used for the Tasseled Cap time series analysis (1986-2021). Areas with less than four years of observations are masked; **B)** Acquisition dates of imagery; and **C)** Tasseled Cap Indices time series over 60 random targets in developed areas, with yearly mean (solid black) and regression line (dotted black). Regression is based on repeated median regression of Siegel (1982) and performed with the "mblm" R package.

The TC indices can be used to make a qualitative (visual) or quantitative assessment of changes in the landscape. First, monotonic trends (showing a continuous, gradual or progressive, increasing or decreasing trend) can be assessed with pixel-based Theil-Sen's regressions. These were calculated in the R environment using an adaptation of the Regional Kendall Tests (RKT) package (Pironkova et al., 2018). The results are raster images showing the direction and magnitude of changes in brightness (TCB), greenness (TCG), and wetness (TCW) . The statistical significance of the Theil-Sen's regressions was assessed using the Mann-Kendall test. Masking p-values >0.05 from the TC trends reveals areas with significant trends in each of the three TC indices.

Many landscape changes are non-monotonic (i.e., cyclical or irregular); for example, forest fires, slumps, and anthropogenic disturbances. To assess such changes based on the TC trends (Theil-Sen's slopes), additionally to the gradual and progressive changes, we used the Landsat Arctic Rgb CHanges (LARCH) method (Fraser et al., 2014), where the values of the three TC indices trends are composited into a RGB image using the Composite Bands tool in Esri ArcGIS Pro, and visualized with a linear histogram stretch within ±5 standard deviations. The product is an image depicting the three-dimensional TC trajectory using additive color mixing and provides a qualitative representation of a variety of landscape changes: subtle or gradual natural changes such as tundra greening and shrub growth; abrupt changes such as thaw slumps or wildfires; and anthropogenic modifications, such as road construction or mining (Brooker et al., 2014; Fraser et al., 2014; NWT Centre for Geomatics, 2021; Olthof and Fraser, 2014). These changes can be identified based on the color family associated with their three-dimensional TC trend.

3.3.3. Classification of landscape changes

To map cumulative changes in the study area and generate a landscape change map, the individual TC indices trends were classified using a supervised random forest classification (Olthof and Fraser, 2014) implemented in the Esri ArcGIS Pro Spatial Statistics toolbox. The Forest-based Classification and Regression tool uses a random subset of the training dataset and explanatory variables in each tree, and uses the entire forest for prediction, which helps avoid overfitting of the model to the training dataset. The model was trained with a total of 1445 pixels corresponding to different landscape changes: 1) erosion, 2) wetting/gullying, 3) vegetation colonization, 4) greening (shrubification), 5) vegetation regeneration, 6) vegetation succession, 7) deposition/drying, 8) earlier melting of ice/snow, and 9) stable. A tenth class was included to isolate bedrock because all exposed bedrock in the study area is located on terrain with varying

Table 3.1 Landscape change class legend with associated processes and disturbances, the number of training pixels from training polygons and average TC indices Thiel-Sen regression coefficients. Negative coefficients are shaded to visualise similarities between and within change classes.

Landscape change class		Processes or disturbances	# of training pixels	TCB slope × 10	TCB offset	TCG slope × 10	TCG offset	TCW slope × 10	TCW offset
1	Erosion	Eroded lake shorelines or river banks	150	-95.1	504.5	-69.6	233.3	33.5	-124.1
		Active and wet portion of slump		-98.6	617.6	-75.6	284.7	32.8	-213.8
		Ponding		-99.4	553.0	-72.7	286.3	34.2	-152.7
2	Wetting/gullying	Surface wetness increase	105	-59.8	650.6	-40.3	306.0	28.3	-230.4
3	Vegetation colonization	Drained lake with vegetation growth	195	60.3	340.6	32.8	129.0	-31.0	-78.6
		Conversion of stream bed to vegetation		41.6	352.2	33.1	119.3	-14.9	-70.2
		Vegetation colonization in slump (older portion of slump)		48.6	444.7	49.0	197.2	-7.6	-93.2
		Vegetation colonization in recent forest fire (1999-2011)		62.0	407.8	44.4	190.9	-24.2	-76.0
4	Greening	Shrub proliferation (along rivers and in older portion of slumps)	195	-30.5	500.1	21.3	200.8	13.3	-129.5
		Abandoned quarries		-15.6	498.1	26.6	166.6	19.6	-166.7
		Greening in previous forest fire (1957-1983)		-17.3	505.6	25.0	173.9	31.6	-218.7
		Greening in old forest fire (1986-1994)		-29.4	564.0	25.3	163.4	29.5	-159.9
		Greening in recent forest fire (1999-2011)		-12.4	575.2	28.9	320.0	11.7	-147.1
5	Vegetation regeneration	Later regeneration in previous forest fire (1957-1983)	140	37.7	462.1	35.7	128.7	30.0	-216.8
		Regeneration in old forest fire (1986-1994)		45.2	409.7	39.6	131.6	26.0	-186.1
6	Vegetation succession	Succession in previous forest fire (1957-1983)	180	-47.8	582.5	-29.5	295.7	32.5	-195.7
		Succession in old forest fire (1986-1994)		45.2	409.7	39.6	131.6	26.0	-186.1
		Forest succession		-65.7	631.0	-46.3	363.0	22.5	-158.0
7	Deposition/drying	New stream and river sandbar	165	19.5	390.4	-12.6	146.7	-15.4	-81.7
		Recent forest fire (1999-2011)		38.2	491.4	-21.8	256.6	-28.4	-98.7
8	Earlier melting of ice/snow	Earlier melting of icings	100	-117.9	1393.1	52.5	-299.0	-58.9	485.1
9	Stable	Developed area	90	-5.2	450.0	0.4	135.3	-0.1	-140.8
10	Bedrock	Exposed bedrock	125	-25.0	362.7	-5.3	25.0	12.2	-212.7

slopes and aspects where reflectance is not properly normalized when using TOA reflectance products.

The landscape change classes were created based on extraction of TC Theil-Sen slopes and offsets (i.e., initial conditions on first year of record), and verified using ancillary datasets (National Air Photo Library photographs, WorldView-2 and Planet Scope satellite imagery, Google Earth high-resolution imagery, and Yukon Wildland Fire Management database), as described in Olthof and Fraser (2014). **Table 3.1** shows processes and disturbances associated with each class, and their average TCB, TCG, and TCW slopes and offsets. It should be noted that different types of vegetation changes are found within forest fires that occurred during the same period, which is likely due to varying degrees of burn severity, different levels of post-fire recovery or differences in species composition (Kasischke et al., 2000; Hollingsworth et al., 2013). Explanatory variables for the classification included TCB, TCG and TCW slopes and offsets, and landcover (Latifovic et al., 2017) (**Fig. 3.2**). The most important variables to classify landscape change in the study area were the TCB slopes, followed by the other TC slopes, the offsets and the landcover (**Table 3.2**).

Table 3.2 Explanatory variable importance

Variable	Importance[1]	%[2]
TCB slope	13.1	19
TCG slope	11.8	17
TCW slope	11.4	16
TCG offset	9.8	14
TCB offset	9.7	14
TCW offset	9.1	14
Landcover (NACLMS)	5.69	8

[1] sum of the Gini coefficients from all the trees for each variable listed

[2] percentage of the total sum of Gini coefficients (Ceriani and Verme, 2012)

A total of 100 classification trees were created in the forest model and 25% of training pixels were excluded for validation. The model was run 10 times until the distribution of R^2 was stable and the model that produced the highest R^2 (0.84) was used for predictions. The model created trees of depths ranging between 28 and 62 splits (average: 41), with leaf sizes of 1. The number of randomly sampled explanatory variables used to create each decision tree was 2.

Classification diagnostics, which were calculated using a confusion matrix, revealed that the model performed generally well (**Table 3.3**). However, some confusion exists for the wetting/gullying class (**Table 3.3**).

The final landscape change map represents nine change classes from which exposed bedrock and non-significant changes based on the Mann-Kendall test were masked. Since there are types of processes that can cause significant changes in only one of the three indices, a pixel was considered significant if at least one of the TC index had a p-value <0.05. Small, isolated clusters of less than 60 x 60 m (4 pixels) were also masked as non-significant.

Table 3.3 Confusion matrix and classification diagnostics from the forest-based classification of nine change processes

		1	**2**	**3**	**4**	**5**	**6**	**7**	**8**	**9**	**10**	**Precision (%)**
1	Erosion	31	4	0	0	0	3	0	0	0	0	**81.6**
2	Wetting/gullying	4	21	0	0	0	2	0	0	0	0	**77.8**
3	Vegetation colonization	0	0	42	0	0	0	7	0	0	0	**85.7**
4	Greening	1	5	0	37	1	0	1	0	4	0	**75.5**
5	Vegetation regeneration	0	2	0	3	27	0	1	0	2	0	**77.1**
6	Vegetation succession	2	6	0	0	0	37	0	0	0	0	**82.2**
7	Deposition/Drying	0	1	3	0	1	0	36	0	1	0	**85.7**
8	Earlier melting of ice/snow	1	0	1	1	0	0	1	21	0	0	**84.0**
9	Stable (Developed)	0	0	1	4	0	0	1	0	16	1	**69.6**
10	Bedrock	0	0	0	0	0	0	0	0	0	32	**100.0**
	Sensitivity (%)	**79.5**	**53.8**	**89.4**	**82.2**	**93.1**	**88.1**	**76.6**	**100.0**	**69.6**	**97.0**	
											Overall accuracy (%):	**82.2**
											Overall F1-score:	**0.8**

3.3.4. Multi-level interpretation and validation

Context and timing of landscape changes were further interpreted by plotting pixel-based time-series of each TC index and through examination of historical aerial photographs (1:30000 National Air Photo Library; 1963, 1977, 1989, 2000) and high-resolution satellite imagery (0.5 m resolution WorldView-2: 2009, 2012; 2020; and 3 m resolution Planet Scope: 2019). The change signals identified in the TC trends RGB composite and through extraction of pixel-based time-series were also validated using open source Google Earth Engine (GEE) applications: i) the Google Earth Engine HotSpot Regions of Permafrost Change Production and Visualization application (Nitze, 2022), ii) the Earth Engine RGB Timeseries application (Braaten, 2021) and iii) two GEE applications which are derived from the Landsat-based Detection of Trends in Disturbance and Recovery (LandTrendr) , namely the UI LandTrendr Pixel Time Series Plotter and the UI LandTrendr Change Mapper (Kennedy et al., 2018). The identified landscape changes were then compared to the geomorphology, landcover and glacial limits map of the study area (**Fig. 3.2**).

3.4 Results

3.4.1. Classified landscape changes

The landscape change map, in which non-significant trends, small clusters (<4 pixels) and exposed bedrock were masked, indicate that significant change occurred in 24% of the study area (**Fig. 3.5**). The most widespread change observed is wetting/gullying (17% of study area) in the river valleys and on valley slopes north of North Fork Pass and in the Taiga Valley. Wetting/gullying occurs mostly in association with smaller tributaries, beaded streams, runoff tracks and ice-wedge polygons zones. The second most common change is vegetation succession (5% of study area), which is associated with evergreen species replacing deciduous species (Cipar et al., 2004; Fraser et al., 2014; Hansen et al., 2001; Roberts et al., 2004). The third most widespread change class is deposition/drying (1% of study area), which is seen mostly along rivers and on valley slopes and is therefore associated with river migration and potential changes in moisture. The remaining landscape changes occupy <4% of the study area: greening (0.3%), vegetation regeneration (0.2%), erosion (0.2%), vegetation colonization (0.1%), stable (0.05%), and earlier melting of ice/snow (0.02%).

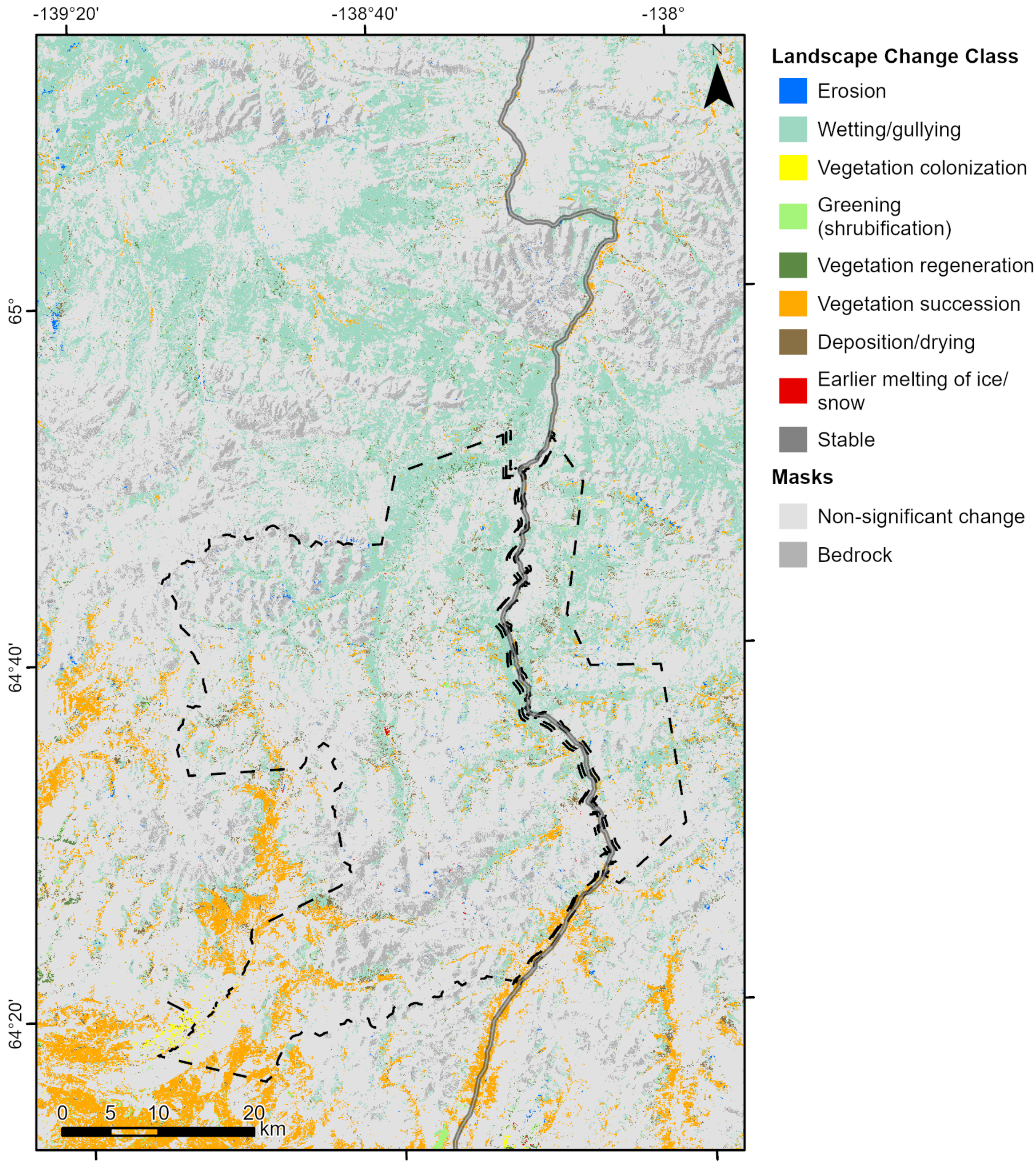

Figure 3.5 Change map of the Tombstone Territorial Park region, central Yukon, classified in nine change processes. Non-significant trends (p-values >0.05), isolated clusters (<60 x 60 m) and exposed bedrock are masked.

3.4.2. *Landsat Arctic Rgb CHanges (LARCH)*

3.4.2.1. Landscape disturbances

Wildfire regeneration was the most noticeable change detected in the TC trend composite image, occupying 5.4% of the study area (**Fig. 3.6 and 3.7**). The number (n=16) and extent of historical forest fires (0.004 to 250.8 km^2, $\bar{x}$= 28.7 ± 62.5 km^2) matched those inventoried by the Government of Yukon Wildland Fire Management branch (**Fig. 3.7 and 3.8a**), although the extent of most fires identified by the TC trend were slightly lower than those in the database because the latter might include unburnt patches. We were able to identify three new fires (0.5 to 1.6 km^2) in the western part of the study area (**Fig. 3.7**). The pixel-based time-series extracted from fires that occurred i) prior to 1977 are associated with a wetness increase linked with forest succession, ii) earlier in the period of the analysis (1983-1994) are associated with an increase in brightness (TCB) and

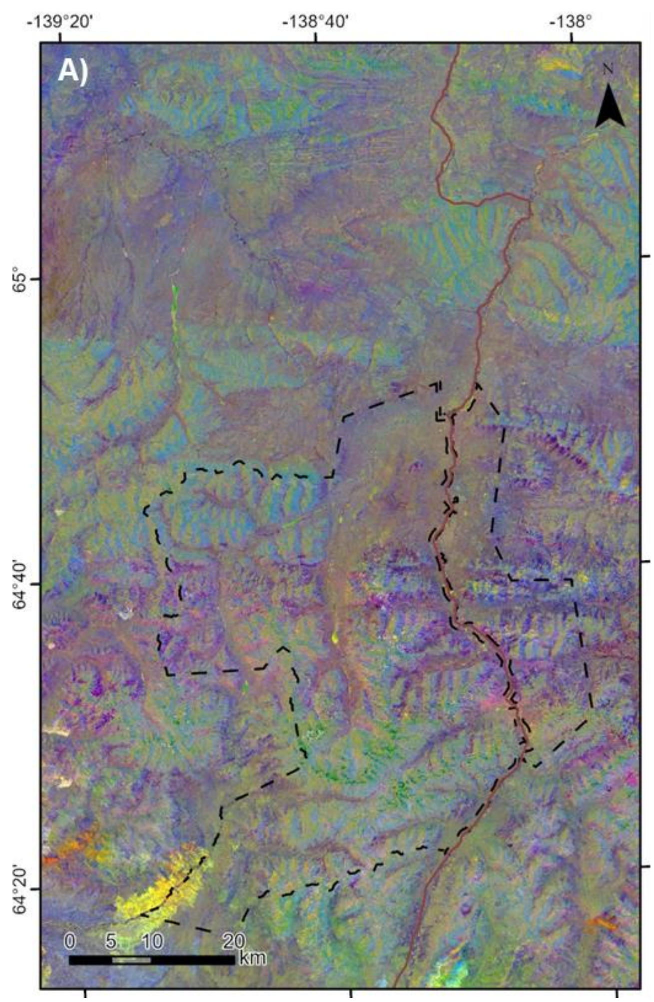

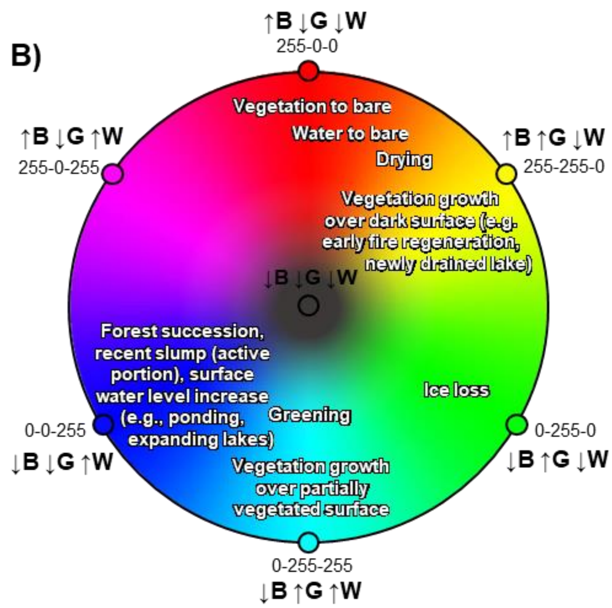

Figure 3.6 A) Tasseled Cap Indices trends RGB composite covering the Tombstone Territorial Park (black dashes) region. The Dempster Highway (red line) traverses the park. **B)** Color wheel legend used to interpret landscape changes associated with color families shown on the TC trends RGB composite. Modified from Fraser et al., 2014.

decrease in greenness (TCG) and wetness (TCW) following the burn, and iii) during the latter half of the analysis period (1999-2011) are associated with an increase in greenness (TCG) and wetness (TCW) associated with initial vegetation regeneration.

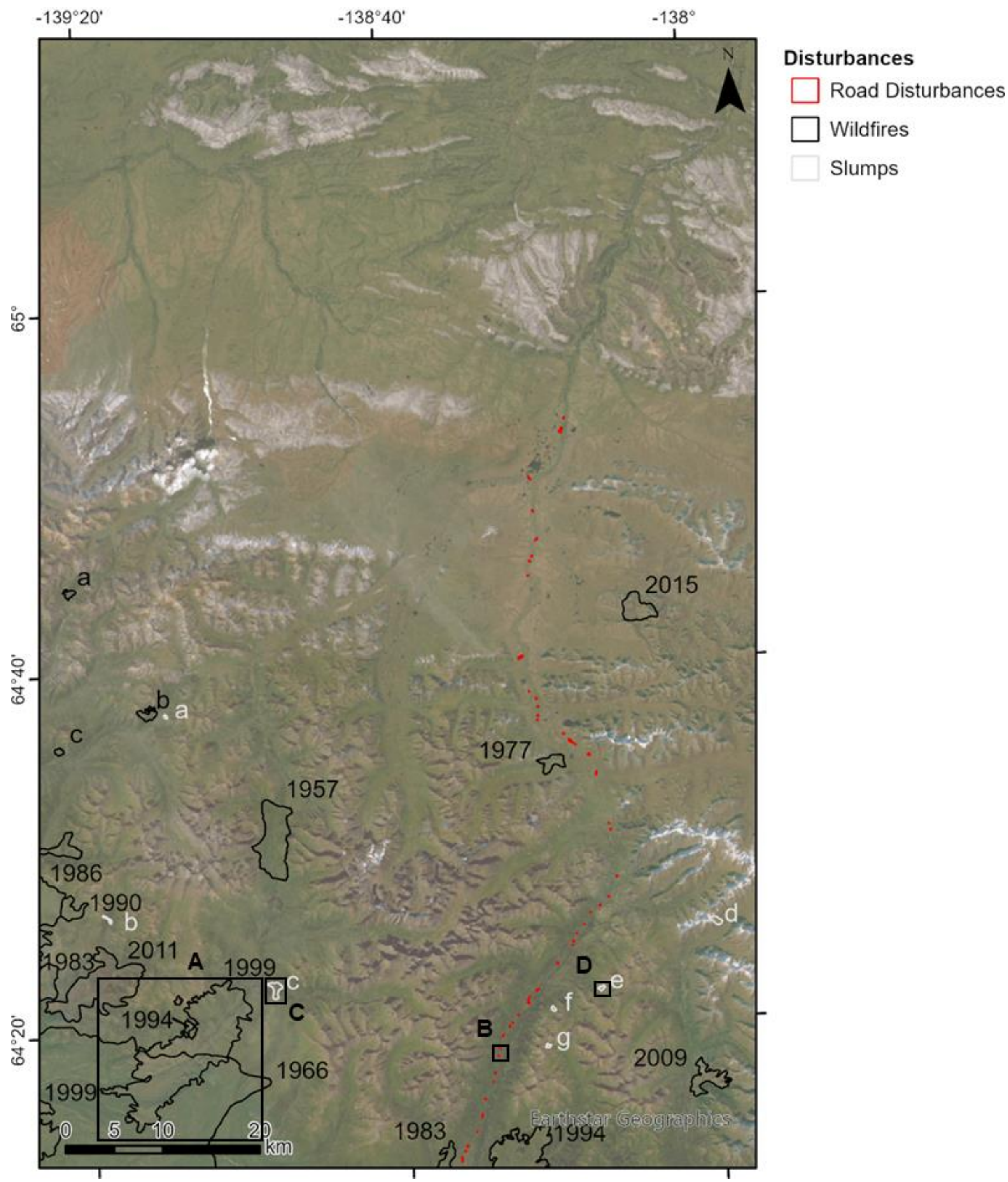

Figure 3.7 Landscape disturbances highlighted by the Tasseled Cap Indices trends RGB composite. Black rectangles labelled with capital letters are examples shown in Fig. 3.8.

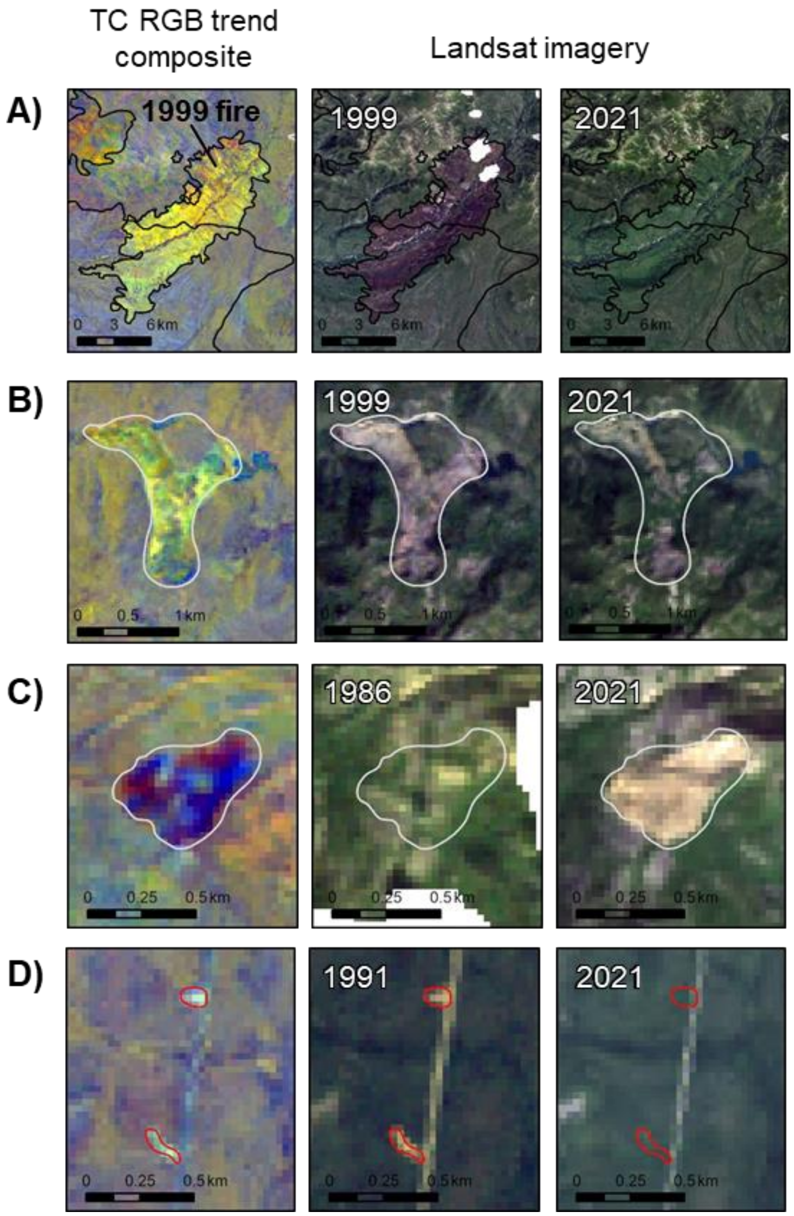

Figure 3.8 Examples of **A)** the 1999 wildfire, **B)** slump *c*, **C)** slump *e*, and **D)** road disturbances, in the Tasseled Cap indices trends RGB composite and Landsat imagery. Location of examples are shown in Fig. 3.7 as black outlines.

Thaw slumps are another landscape disturbance that could be detected using the LARCH method (**Fig. 3.6 and 3.7**). Our analysis identified seven thaw slumps (e.g., **Fig. 3.8b and 3.8c**), all located between 700 and 1750 m a.s.l. and within differing landcover types (**Table 3.4**). Comparison with historical imagery and the Google Earth Engine applications confirmed the presence of slumps in all seven locations, but there are other slumps in the study area that are too small to be identified from Landsat imagery (i.e., Two Moose Lake; Grinter et al., 2019; Lacelle et al., 2009). The largest slump (Slump *c*) is found in the needleleaf forest landcover along Little Twelve Mile River (**Table 3.4**). This thaw slump was active in 1995 and had mostly stabilized by

2021, although the erosion signal near the headwall indicates that it might still be receding (**Fig. 3.8b**). The TC trend of the RGB composite suggests that the other six slumps are still active or that the vegetation has yet to recover (e.g., **Fig. 3.8c**).

Table 3.4 Location, area, mean elevation and year slumps identified in the study area became active.

ID	Latitude	Longitude	Area (km^2)	Mean elevation and std. dev. (m a.s.l.)	Landcover	Year active
a	64.63	-139.17	0.10	1205 ± 64	Needleleaft Forest, Shrubland	>1986
b	64.44	-139.30	0.19	1111 ± 143	Shrubland	1997
c	64.37	-138.95	1.21	892 ± 144	Needleleaf Forest	1996
d	64.42	-138.00	0.65	1500 ± 117	Barren and Grassland	>1986
e	64.36	-138.25	0.23	1258 ± 75	Shrubland	1999
f	64.35	-138.36	0.16	1218 ± 65	Needleleaf Forest and Grassland	2006
g	64.31	-138.37	0.14	1469 ± 68	Barren and Grassland-lichen-moss	2004

The TC trend RGB composite also reveals revegetation of some of the small road-side quarries that supply the material to maintain the Dempster Highway (**Fig. 3.6 and 3.7**). This is evident from increase in greenness (TCG) in the TC RGB trend composite and TC indices time-series (e.g., **Fig. 3.8d**).

3.4.2.2. Hydrological changes

Out of the 1145 lakes identified in the study region, 1024 lakes (89.4%) showed little or no changes in extent, 79 lakes (6.9%) showed some change in extent (expansion or shrinkage), and 42 new waterbodies (3.7%) formed (**Fig. 3.9**). For example, comparison of satellite imagery and aerial photographs shows that Lone Moose Lake, located ca. 35 m to the east of the East Blackstone River at 1120 m a.sl., has experienced a substantial shrinkage which corresponded to signs of vegetation growth within its partially drained perimeter on the TC RGB trend composite image (**Fig. 3.10a**). By contrast, Two Moose Lake, located to the west of the Dempster Highway at 1093 m a.s.l., shows evidence of shoreline erosion and lake expansion along its western shore (**Fig. 3.10a**) where a thaw slump developed. An example of new ponds emerging due to beaver damming can be seen along a section of the braided North Klondike River (**Fig. 3.10b)**. Lakes that show changes (expansion, shrinkage or ponding) are mostly located in river valleys, in proximity to watercourses. Out of the 114 lakes found within or near (<50 m distance) ice-wedge polygons zones, 92 remained stable (80.7%), 21 experienced changes in extent (18.5%), and 1 new waterbody formed (0.9%).

The LARCH method also revealed changes to riverbanks, which vary depending on the location and morphology of the watercourse (**Fig. 3.9**). These changes are: little to no change detected (64.4% of watercourses), migration of braided system rivers (18.2%) and meandering

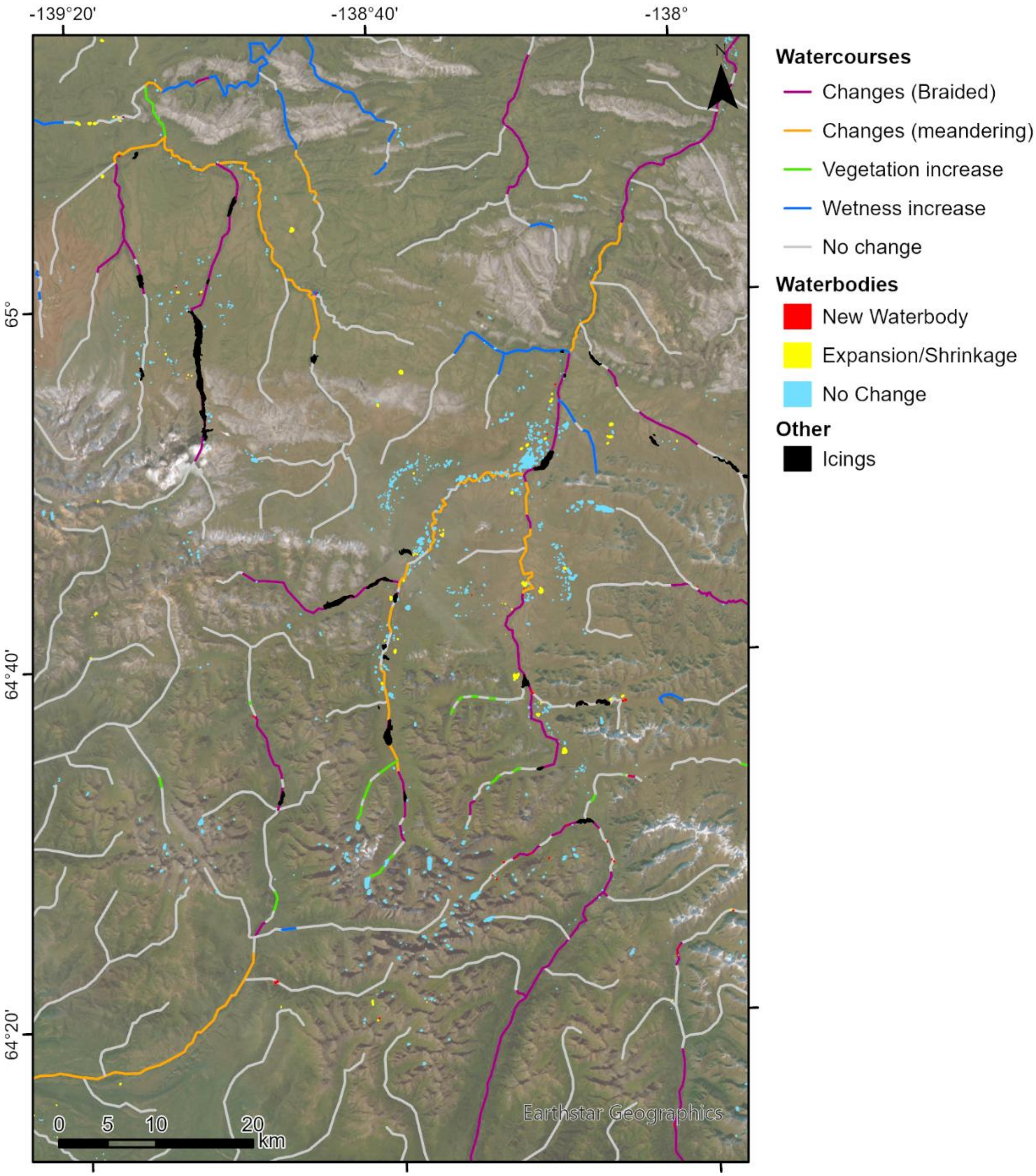

Figure 3.9 Hydrological changes highlighted by the Tasseled Cap Indices trends RGB composite. Black outlines are examples shown in Fig. 3.10.

rivers (9.7%), wetness increase (5.9%) and vegetation increase (1.7%) along the banks of streams and rivers. The TC trends RGB composite image identified deposition of sediment on point bars, erosion of cut banks, and cut off and drying of oxbow lakes followed by vegetation regeneration and greening along the major rivers (i.e., Chandindu, North Klondike, Blackstone, East Blackstone, Engineer Creek, and the larger tributaries of the Ogilvie River in the Taiga Valley) (e.g., **Fig. 3.9c and 3.9d**). In a few areas, a vegetation recovery signal was detected, indicating vegetation growth within bare areas of the riparian zone. The watercourses where only a wetness increase was detected are found exclusively in the northern half of the study area and could be attributed to an increase in shrub cover in the riparian zone (i.e., Hansen et al., 2001).

Finally, nearly half of the icings (n=15) in the study area are associated with a TC trend RGB signature suggestive of ice loss. Extracting time-series of these icings reveals that they are associated with an earlier melting in the summer, which has implication for the hydrological processes of these fluvial systems.

3.4.2.3. Landcover changes

The landscape change map revealed that 0.3% of the study area experienced greening, and about a third of this class was associated with wildfires. This is confirmed from the LARCH method that shows no widespread trend of tundra greening, except for small areas along the Dempster Highway.

The TC trends RGB composite image suggests landcover changes are occurring in the Taiga Valley and along the East Blackstone river valley (**Fig. 3.6**). In these valleys, the peripheral areas of some zones of ice-wedge polygons reveal a substantial increase in wetness (TCW) and a decrease in brightness (TCB) and greenness (TCG), especially along small streams and runoff tracks. It should be noted that this wetness increase is not associated with an increase in ponding, as evidenced by the lack of formation of new waterbodies in these areas, but rather an increase in surface moisture. This is also represented in the classified change map as widespread wetting/gullying and a lack of erosion.

In the boreal forest ecosystem, in the southwest part of the study area that was not affected by wildfires, patterns of vegetation recovery and wetness increase are identified and correspond to patches of distinct vegetation types in the landscape. Comparing the Landsat imagery over the time frame of the landscape change analysis, there are indeed years where patches of vegetation appear lighter green or have a reddish coloration. These are also associated with patterns of vegetation succession and greening in the classified change map (**Fig. 3.5**). This could be an indication that these patches of forest have been affected by damaging insects.

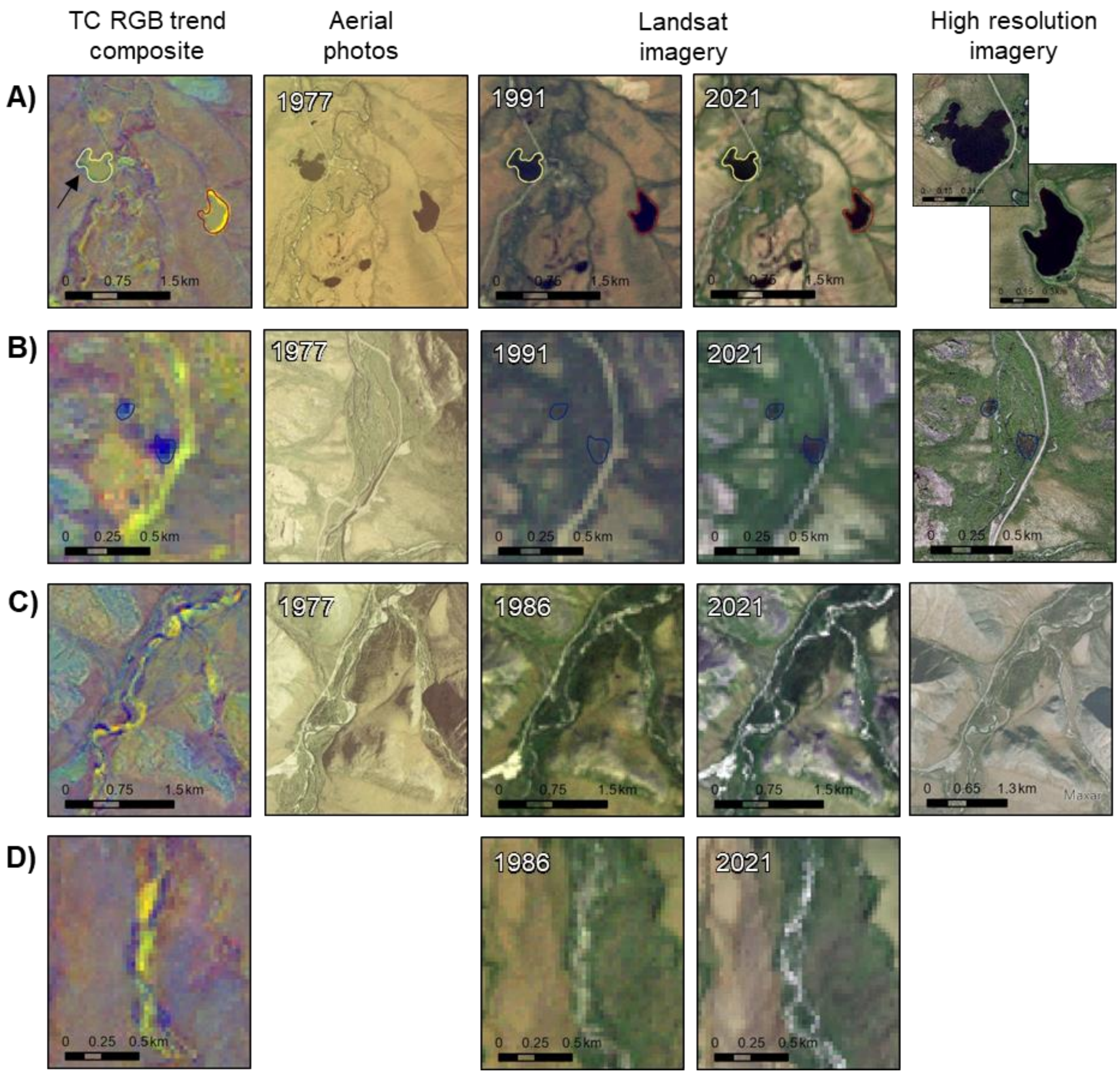

Figure 3.10 Examples of **A)** water level changes (Two Moose Lake, thaw slump indicated by black arrow) and draining of lake (Lone Moose Lake), **B)** ponding, **C)** meandering river migration, and **D)** braided river shifting in the Tasseled Cap indices trends RGB composite, aerial photographs, Landsat imagery and high resolution DigitalGlobe (DG) imagery. Location of examples are shown in Fig. 3.9 as black outlines.

3.5 Discussion

3.5.1. Landcover and hydrological changes and their meaning

In many regions of the Arctic and Sub-Arctic, air temperature warming has led to greening of the landscape (Druckenmiller et al., 2022). However, in our study area the TCG and NDVI both show overall decreasing trends (Ju and Masek, 2018). Although some recent studies have shown a browning of tundra vegetation in some regions (Lara et al., 2018); however, this has been associated with dryer conditions (Buchwal et al., 2020). In the study area, the majority of the tundra ecosystem shows negative TCG trends associated with a wetness (TCW) increase and brightness (TCB) decrease, as evidenced by the large area covered by the ”wetting/gullying” landscape change class. It is not likely that such a large part of the tundra ecosystem is experiencing either wetting or gullying. Instead, these might reflect changes in vegetation cover. These spectral changes are typical of vegetation succession where evergreen species are replacing deciduous vegetation (Cipar et al., 2004; Fraser et al., 2014; Hansen et al., 2001; Roberts et al., 2004). Arctic shrubification is usually associated with an increase in deciduous species, however some studies have reported an increase in evergreen shrubs associated with climate warming (e.g., (Vuorinen et al., 2017; Weijers et al., 2018; Wilson and Nilsson, 2009; Vowles and Björk, 2019). Our findings are consistent with these studies.

In the boreal forest ecosystem, we found patterns of vegetation appearing lighter or having a reddish coloration associated with vegetation succession and greening signals which correspond to the spectral signature of damaging insects such as bark beetles and defoliators (Senf et al., 2015). Damaging insects outbreaks are common in coniferous forests of North America and in the Yukon, but we found very little documentation of this phenomenon in our study area; A 2021 Forest Health aerial survey in the Yukon covered the southern part of TTP (Forest Management Branch, 2022). Only <1% of trees spruce bark beetle attack in two stands south-east of the study area were identified. Patches of aspen serpentine leaf miner and large aspen tortrix defoliation were more widespread and correspond to some of the patches we identified in the southwest area. Other patches not identified in the 2021 Forest Health aerial survey present the same TC change signals, suggesting that damaging insect outbreaks can be identified using the TC trends analysis.

Some of the most dynamic, yet localised areas of landcover and hydrological changes are associated with fluvial systems. While most watercourses show little to no change over the 1986-

2021 period (64.4%), migration of braided and meandering rivers was observed. In permafrost environments, these changes can have significant impact on the global carbon cycle and on aquatic ecosystems as organic carbon and nutrients are released from permafrost through erosion of riverbanks (McClelland et al., 2006; Toohey et al., 2016; Walvoord and Striegl, 2007). However, a recent study has shown that some of the organic carbon mobilized through erosion of cutbanks in meandering rivers is redeposited in point bars rather than being oxidized (Douglas et al., 2022). This suggests that the contribution of river erosion to the global carbon cycle could be reduced by sediment deposition and subsequent permafrost aggradation in river bars. Therefore, the presence of both erosion and deposition signals along rivers in the study area is not necessarily an indication of increased organic carbon contents in fluvial systems.

3.5.2. Thermokarst and comparison with other regions

The higher elevations in TTP ensure the presence of continuous permafrost in a region otherwise surrounded by discontinuous permafrost. TTP has many periglacial features, such as ice-wedge polygons, thaw slumps, pingos, seasonal frost mounds, and rock glaciers, which are more typical of higher latitudes. In these regions, the permafrost landscape is experiencing thermokarst in response to warming air temperatures (Romanovsky et al., 2017). For example, an intensification of thaw slump activity has been observed in the Richardson Mountains-Peel Plateau (Kokelj et al., 2015, 2017; Lacelle et al., 2015), on Banks Island (Lewkowicz and Way, 2019) and in the Eureka Sound Lowlands (Ellesmere Island and Axel Heiberg Island) (Ward Jones et al., 2019). In some regions, such as Banks Island, the degradation of ice-wedge polygonal terrain is leading to an increase in the number and extent of thaw ponds (Fraser et al., 2018; Segal et al., 2016), while on the northern Seward Peninsula (Alaska) and in the Old Crow Flats, an increase in lake drainage is leading to the formation of smaller ponds (Jones et al., 2011; Lantz and Turner, 2015).

There appears to be little evidence of thermokarst in our study area. We inventoried seven slumps located in the southern section of the region where ice-wedge polygons are absent using the Landsat imagery, and three smaller slumps in the northern sector (Grinter et al., 2019; Lacelle et al., 2009). This slump density (0.15 slumps/100 km^2) is substantially lower compared to other Arctic regions where slumps are encountered (see Segal et al., 2016). In northwestern Canada, the distribution of thaw slumps coincides with the maximum and recessional limits of the Laurentide Ice Sheet (Kokelj et al., 2017), and the recent increase in thaw slumping reflects a rejuvenation of deglaciation and post-glacial permafrost landscape evolution through stream incisions (Kokelj et al., 2015; Lacelle et al., 2015, 2010). However, none of the inventoried slumps in TTP are located along the McConnell or Reid glacial limits and all have developed in colluvium. In the high-Arctic Eureka Sound Lowlands, thaw slumps develop mostly in ice wedge polygonal terrain; however in TTP only one of the slumps developed in such terrain (i.e., Two Moose Lake). Therefore, the development of slumps in TTP could be related to a more patchy distribution of ice-rich permafrost or to the presence of permafrost and how it affects shear forces and resistance of material along hillslopes (i.e., (Krautblatter and Leith, 2015).

TC trend analysis identified wetting/gullying within 33% of the area of ice-wedge polygonal terrain. Despite showing signs of surface wetness increase, most waterbodies in the polygonal terrain have maintained the same extent; only one new pond was identified, and two showed signs of shrinkage. The majority of IW polygons in the study area are high-centered, with well-drained elevated centers and interconnected low wet troughs (Frappier and Lacelle, 2021). This morphology of IW polygons contributes to lateral surface and subsurface runoff which results in wetness increase within and around polygonal terrain without necessarily forming new ponds. However, the increased wetness would lead to erosion as observed in streams and runoff tracks adjacent to the polygon zones. Localized evidence of ice wedge degradation was observed through wetting and gullying along polygon troughs adjacent to the Dempster Highway (Frappier and Lacelle, 2021). The presence of the road perturbed the surface drainage which causes ponding on the west side. However, this process caused by human-activity seems spatially limited and for the most part do not translate into landscape-scale perturbations that can be identified using the Landsat archive.

3.5.3. Permafrost landscape change in the Ogilvie Mountains: relation with climate, geomorphic processes, ecological succession, and glacial history

The Landsat-derived TC trend analysis indicates that 24% of the study area experienced significant landscape change. These were mainly associated with hydrological or ecological processes (fluvial erosion and vegetation succession). Changes related to thermokarst were relatively few: only seven slumps are active, and ice-wedge polygonal terrain showed mainly wetting along streams and water-tracks. Wildfires, which are often a drivers of permafrost thaw (Jones et al., 2015; Myers-Smith et al., 2008; O'Donnell et al., 2011), did not show subsequent signs of thermokarst (increase in surface wetness) as the spectral signature was consistent with vegetation recovery. Although other regions in the western Arctic have experienced recent thermokarst, namely lake drainage and formation of thaw ponds (e.g., Jones et al., 2011; Labrecque et al., 2009; Lantz and Turner, 2015; Lauriol et al., 2009), others have remained rather stable since at least the early Holocene (e.g., Edwards et al., 2016), or experienced heterogenous and asynchronous changes (e.g., Edwards et al., 2016; Frost et al., 2018; Jorgenson et al., 2022). We suggest a similar response of permafrost landforms to that of those regions where interactions between climate, ground ice content, geomorphic processes and ecological succession have led to maintain a stability in the landscape (Edwards et al., 2016; Frost et al., 2018; Jorgenson et al., 2022).

The vast majority of TTP has remained unglaciated since at least the mid-Pleistocene (**Fig. 3.2**), and the Reid and McConnell glaciogenic sediments in valley bottoms have been buried by accumulating colluvium since at least the mid-Holocene (Grinter et al., 2019; St-Jean et al., 2011). The sandy silt colluvium contains mostly pore ice to low excess ice and as such would not be highly sensitive to permafrost degradation (Frappier and Lacelle, 2021; Grinter et al., 2019). The presence of near-surface excess ice comes mostly from ice wedges that began to develop 6500 cal yr BP in the colluvium (Frappier and Lacelle, 2021; Grinter et al., 2019), or as buried remnants of glacial ice, but these have a patchy distribution (Lacelle et al., 2007). In the study area, the early Holocene warm interval most likely melted vast amounts of near-surface massive ground ice, as evidenced from truncated Late Pleistocene age ice wedges (Grinter et al., 2019). The cooler and possibly wetter climate of the mid-Holocene allowed for black spruce forest and green alder to replace white spruce forest (Cwynar and Spear, 1995; Dyke, 2005) which caused permafrost to aggrade (Ritchie, 1984). As the cooling trend continued, the forest cover reached its current extent in the southern part of TTP and gave way to tundra in the central and northern parts (Cwynar and Spear, 1995). Since then, the presence of an organic surface layer and the colluviation act as a buffer layer protecting permafrost from air conditions. This contrasts with other barren, till-dominated lands where important permafrost degradation has been related to the lack of protective vegetation and organic layer (Fraser et al., 2018; Ward Jones et al., 2019). Moreover, during the period of study, air temperatures have remained rather stable, except for a slight increase in mean January temperatures, which could also contribute to the relative stability of the landscape revealed by our analysis.

Therefore, a very heterogeneous mosaic of differing permafrost response can develop based on previous permafrost formation and degradation, vegetation changes, geomorphic processes such as colluviation and ground ice development, and recent climate changes (Jorgenson et al., 2022). Still, it is important to note that while recent landcover and hydrological changes and thermokarst appear limited in the study area, the ground thermal regime can still be affected and these can act as positive feedbacks for permafrost degradation.

3.6 Conclusion

A Landsat-derived TC trend landscape change analysis in the Ogilvie Mountains in Central Yukon has revealed that 24% of the landscape has experienced significant landscape changes. The main monotonic (i.e., gradual or progressive) significant changes include:

1. Wetting and gullying in association with smaller tributaries, beaded streams, runoff tracks and ice-wedge polygons peripheries.
2. Vegetation succession through evergreen species increase in the forest and tundra ecosystem.
3. Deposition or drying associated with river migration and valley slopes.
4. Greenness decrease in most of the landcover types. No substantial greening occurred in the study area, and about a third of the greening was associated with recovery after wildfires.

Substantial non-monotonic (i.e., cyclical or irregular) changes include:

1. Wildfires (5.4% of the study area; the TC indices trend analysis method identified fires previously not inventoried)
2. Seven thaw slumps in the southern section of the region, where ice-wedge polygons are absent.
3. Migration of braided and meandering rivers associated mainly with deposition of sediment on point bars, erosion of cut banks, and cut off of oxbow lakes along the major rivers.
4. Earlier melting of icings in the summer.
5. Wetting and gullying in the peripheral areas of some ice-wedge polygons zones, especially along small streams and runoff tracks. The polygons lacked the development of new ponds.

6. Damaging insect outbreaks in the boreal forest ecosystem (the TC indices trend analysis method identified potential damage previously not inventoried).

Our investigation highlights how the extent and magnitude of landscape changes in TTP and surrounding areas is dictated by climate, geomorphic settings, ecological succession, and glacial history of the region. Given a varied combination of ecotypes, significant spatial and temporal variations are to be expected in terms of the response of permafrost landscapes to climate and anthropogenic disturbances.

3.7 Acknowledgements

This research was supported by Natural Resources Canada as a part of the Government of Canada's initiative for monitoring and assessing regional cumulative effects, les Fonds de recherche du Québec – Nature et Technologies (FRQNT), and Natural Sciences and Engineering Research Council of Canada (NSERC) Discovery Grant. The authors also thank DigitalGlobe for providing high resolution satellite imagery and ClimateData.ca for providing the climate information used in this paper.

3.10 References

Arctic Monitoring and Assessment Programme (AMAP), 2017. Snow, Water, Ice and Permafrost in the Arctic (SWIPA). Oslo.

Braaten, J., 2021. Earth Engine RGB Timeseries application [WWW Document]. URL https://jstnbraaten.users.earthengine.app/view/landsat-timeseries-explorer#run=false;lon=-122.91966;lat=44.24135;from=06-10;to=09-20;index=NBR;rgb=SWIR1%2FNIR%2FGREEN;chipwidth=2;

Brooker, A., Fraser, R.H., Olthof, I., Kokelj, S. v, Lacelle, D., 2014. Mapping the activity and evolution of retrogressive thaw slumps by tasselled cap trend analysis of a landsat satellite image stack. Permafrost and Periglacial Processes 25, 243–256. https://doi.org/10.1002/ppp.1819

Buchwal, A., Sullivan, P.F., Macias-Fauria, M., Post, E., Myers-Smith, I.H., Stroeve, J.C., Blok, D., Tape, K.D., Forbes, B.C., Ropars, P., Lévesque, E., Elberling, B., Angers-Blondin, S., Boyle, J.S., Boudreau, S., Boulanger-Lapointe, N., Gamm, C., Hallinger, M., Rachlewicz, G., Young, A., Zetterberg, P., Welker, J.M., 2020. Divergence of Arctic shrub growth associated with sea ice decline. Proc Natl Acad Sci U S A 117, 33334–33344. https://doi.org/10.1073/PNAS.2013311117/SUPPL_FILE/PNAS.2013311117.SD01.PDF

Calmels, F., Roy, L.P., Grandmont, K., Pugh, R., 2018. Summary of climate-and geohazard-related vulnerabilities for the Dempster Highway corridor.

Carroll, M., Wooten, M., DiMiceli, C., Sohlberg, R., Kelly, M., 2016. Quantifying Surface Water Dynamics at 30 Meter Spatial Resolution in the North American High Northern Latitudes 1991–2011. Remote Sensing 2016, Vol. 8, Page 622 8, 622. https://doi.org/10.3390/RS8080622

Ceriani, L. and Verme, P. 2012. The origins of the Gini index: extracts from Variabilità e Mutabilità (1912) by Corrado Gini. The Journal of Economic Inequality, 10, 421–443.

Chipman, M.L., Hudspith, V., Higuera, P.E., Duffy, P.A., Kelly, R., Oswald, W.W., Hu, F.S., 2015. Spatiotemporal patterns of tundra fires: Late-Quaternary charcoal records from Alaska. Biogeosciences 12, 4017–4027. https://doi.org/10.5194/BG-12-4017-2015

Cipar, J., Cooley, T., Lockwood, R., Grigsby, P., 2004. Distinquishing between coniferous and deciduous forests using hyperspectral imagery, in: International Geoscience and Remote Sensing Symposium (IGARSS). pp. 2348–2351. https://doi.org/10.1109/igarss.2004.1369758

Council of Canadian Academies, 2014. Aboriginal Food Security in Northern Canada: An Assessment of the State of Knowledge.

Crist, E.P., Cicone, R.C., 1984. A Physically-Based Transformation of Thematic Mapper Data-The TM Tasseled Cap, IEEE Transactions On Geoscience And Remote Sensing.

Cwynar, L.C., Spear, R.W., 1995. Paleovegetation and Paleoclimatic Changes in the Yukon at 6 ka BP. Géographie physique et Quaternaire 49, 29–35. https://doi.org/10.7202/033027ar

Douglas, M.M., Li, G.K., Fischer, W.W., Rowland, J.C., Kemeny, P.C., West, A.J., Schwenk, J., Piliouras, A.P., Chadwick, A.J., Lamb, M.P., 2022. Organic carbon burial by river meandering partially offsets bank erosion carbon fluxes in a discontinuous permafrost floodplain. Earth Surface Dynamics 10, 421–435. https://doi.org/10.5194/ESURF-10-421-2022

Druckenmiller, M.L., Thoman, R.L., and Moon, T.A. (Eds). 2022. Arctic Report Card 2022. https://doi.org/10.25923/yjx6-r184.

Duk-Rodkin, A., 1996. Surficial geology, Dawson, Yukon Territory, 1:250,000.

Dyke, A.S., 2005. Late quaternary vegetation history of northern North America based on pollen, macrofossil and faunal remains. Geographie Physique et Quaternaire 59, 211–262.

Edwards, M., Grosse, G., Jones, B.M., McDowell, P., 2016. The evolution of a thermokarst-lake landscape: Late Quaternary permafrost degradation and stabilization in interior Alaska. Sedimentary Geology 340, 3–14. https://doi.org/10.1016/j.sedgeo.2016.01.018

Farquharson, L.M., Romanovsky, V.E., Cable, W.L., Walker, D.A., Kokelj, S. v, Nicolsky, D., 2019. Climate Change Drives Widespread and Rapid Thermokarst Development in Very Cold Permafrost in the Canadian High Arctic. Geophysical Research Letters 46, 6681–6689. https://doi.org/10.1029/2019GL082187

Forest Management Branch, 2022. 2021 Yukon Forest Health Report, Whitehorse, Yukon.

Frappier, R., Lacelle, D., 2021. Distribution, morphometry, and ice content of ice-wedge polygons in Tombstone Territorial Park, central Yukon, Canada. Permafrost and Periglacial Processes 32, 587–600. https://doi.org/10.1002/ppp.2123

Fraser, R., Kokelj, S., Lantz, T., McFarlane-Winchester, M., Olthof, I., Lacelle, D., 2018. Climate Sensitivity of High Arctic Permafrost Terrain Demonstrated by Widespread Ice-Wedge Thermokarst on Banks Island. Remote Sensing 10, 954. https://doi.org/10.3390/rs10060954

Fraser, R., Olthof, I., Carrière, M., Deschamps, A., Pouliot, D., 2012. A method for trend-based change analysis in Arctic tundra using the 25-year Landsat archive, in: Polar Record. pp. 83–93. https://doi.org/10.1017/S0032247411000477

Fraser, Robert H, Lantz, T.C., Olthof, I., Kokelj, S. v, Sims, R.A., 2014. Warming-Induced Shrub Expansion and Lichen Decline in the Western Canadian Arctic. Ecosystems 17, 1151–1168. https://doi.org/10.1007/s10021-014-9783-3

Fraser, R.H., Olthof, I., Carrì, M., Deschamps, A., Pouliot, D., 2011. Detecting long-term changes to vegetation in northern Canada using the Landsat satellite image archive. Environ. Res. Lett 6, 45502–45511. https://doi.org/10.1088/1748-9326/6/4/045502

Fraser, Robert H., Olthof, I., Kokelj, S. v., Lantz, T.C., Lacelle, D., Brooker, A., Wolfe, S., Schwarz, S., 2014. Detecting landscape changes in high latitude environments using landsat trend analysis: 1. visualization. Remote Sensing 6, 11533–11557. https://doi.org/10.3390/rs61111533

Frost, G. v., Christopherson, T., Jorgenson, M.T., Liljedahl, A.K., Macander, M.J., Walker, D.A., Wells, A.F., 2018. Regional patterns and asynchronous onset of ice-wedge degradation since the mid-20th century in Arctic Alaska. Remote Sensing 10. https://doi.org/10.3390/RS10081312

Grinter, M., Lacelle, D., Baranova, N., Murseli, S., Clark, I.D., 2019. Late Pleistocene and Holocene ice-wedge activity on the Blackstone Plateau, central Yukon, Canada. Quaternary Research (United States) 91, 179–193. https://doi.org/10.1017/qua.2018.65

Hansen, M.J., Franklin, S.E., Woudsma, C., Peterson, M., 2001. Forest structure classification in the North Columbia mountains using the Landsat TM Tasseled Cap wetness component. Canadian Journal of Remote Sensing 27, 20–32. https://doi.org/10.1080/07038992.2001.10854916

Harp, D.R., Zlotnik, V., Abolt, C.J., Busey, B., Avendaño, S.T., Newman, B.D., Atchley, A.L., Jafarov, E., Wilson, C.J., Bennett, K.E., 2021. New insights into the drainage of inundated ice-wedge polygons using fundamental hydrologic principles. The Cryosphere 15, 4005–4029. https://doi.org/10.5194/tc-15-4005-2021

Hjort, J., Karjalainen, O., Aalto, J., Westermann, S., Romanovsky, V.E., Nelson, F.E., Etzelmüller, B., Luoto, M., 2018. Degrading permafrost puts Arctic infrastructure at risk by mid-century. Nature Communications. https://doi.org/10.1038/s41467-018-07557-4

Hjort, J., Streletskiy, D., Doré, G., Wu, Q., Bjella, K., Luoto, M., 2022. Impacts of permafrost degradation on infrastructure. Nature Reviews Earth and Environment. https://doi.org/10.1038/s43017-021-00247-8Hollingsworth, T.N.; Johnstone, J.F.; Bernhardt, E.L.; Chapin, F.S., III. 2013. Fire severity filters regeneration traits to shape community assembly in Alaska's boreal forest. PLoS One, 8, e56033.

Hovelsrud, G.K., Poppel, B., van Oort, B., Reist, J.D., 2011. Arctic Societies, Cultures, and Peoples in a Changing Cryosphere. AMBIO 40, 100–110. https://doi.org/10.1007/s13280-011-0219-4

Hu, F.S., Higuera, P.E., Walsh, J.E., Chapman, W.L., Duffy, P.A., Brubaker, L.B., Chipman, M.L., 2010. Tundra burning in Alaska: Linkages to climatic change and sea ice retreat. Journal of Geophysical Research: Biogeosciences 115, 4002. https://doi.org/10.1029/2009JG001270

Huang, C., Wylie, B., Yang, L., Homer, C., Zylstra, G., 2002. Derivation of a tasselled cap transformation based on Landsat 7 at-satellite reflectance. International Journal of Remote Sensing 23, 1741–1748. https://doi.org/10.1080/01431160110106113

Jia, G.J., Epstein, H.E., Walker, D.A., 2002. Spatial characteristics of AVHRR-NDVI along latitudinal transects in northern Alaska. Journal of Vegetation Science 13, 315–326. https://doi.org/10.1111/j.1654-1103.2002.tb02056.x

Jones, B.M., Grosse, G., Arp, C.D., Jones, M.C., Anthony, K.M.W., Romanovsky, V.E., Jones, C.:, 2011. Modern thermokarst lake dynamics in the continuous permafrost zone, northern Seward Peninsula, Alaska. Alaska, J. Geophys. Res 116, 0–03. https://doi.org/10.1029/2011JG001666

Jones, B.M., Grosse, G., Arp, C.D., Miller, E., Liu, L., Hayes, D.J., Larsen, C.F., 2015. Recent Arctic tundra fire initiates widespread thermokarst development. Scientific Reports 5. https://doi.org/10.1038/srep15865

Jones, B.M., Tape, K.D., Clark, J.A., Bondurant, A.C., Jones, M.K.W., Gaglioti, B. v, Elder, C.D., Witharana, C., Miller, C.E., Jones, C.:, Tape, B.M.;, Clark, K.D.;, Bondurant, J.A.;, Jones, W., Gaglioti, M.K.;, Elder, B.V.;, Witharana, C.D.;, Miller, C.;, 2021. Multi-Dimensional Remote Sensing Analysis Documents Beaver-Induced Permafrost Degradation, Seward Peninsula, Alaska. Remote Sensing 2021, Vol. 13, Page 4863 13, 4863. https://doi.org/10.3390/RS13234863

Jorgenson, M., Harden, J., Kanevskiy, M., O'Donnell, J., Wickland, K., Ewing, S., Manies, K., Zhuang, Q., Shur, Y., Striegl, R., Koch, J., 2013. Reorganization of vegetation, hydrology and soil carbon after permafrost degradation across heterogeneous boreal landscapes. Environmental Research Letters 8, 13. https://doi.org/10.1088/1748-9326/8/3/035017

Jorgenson, M.T., Kanevskiy, M., Roland, C., Hill, K., Schirokauer, D., Stehn, S., Schroeder, B., Shur, Y., 2022. Repeated Permafrost Formation and Degradation in Boreal Peatland Ecosystems in Relation to Climate Extremes, Fire, Ecological Shifts, and a Geomorphic Legacy. https://doi.org/10.3390/atmos13081170

Jorgenson, M T, Kanevskiy, M., Shur, Y., Moskalenko, N., Brown, D.R.N., Wickland, K., Striegl, R., Koch, J., 2015. Role of ground ice dynamics and ecological feedbacks in recent ice wedge degradation and stabilization. Journal of Geophysical Research F: Earth Surface. https://doi.org/10.1002/2015JF003602

Jorgenson, M. T., Kanevskiy, M., Shur, Y., Moskalenko, N., Brown, D.R.N., Wickland, K., Striegl, R., Koch, J., 2015. Role of ground ice dynamics and ecological feedbacks in recent ice wedge degradation and stabilization. Journal of Geophysical Research F: Earth Surface 120, 2280–2297. https://doi.org/10.1002/2015JF003602

Jorgenson, M.T., Racine, C.H., Walters, J.C., Osterkamp, T.E., 2001. Permafrost degradation and ecological changes associated with a warming climate in central Alaska.

Jorgenson, M.T., Romanovsky, V., Harden, J., Shur, Y., O'Donnell, J., Schuur, E. a G., Kanevskiy, M., Marchenko, S., 2010. Resilience and vulnerability of permafrost to climate change. Canadian Journal of Forest Research 40, 1219–1236. https://doi.org/10.1139/X

Ju, J., Masek, J.G., 2018. ABoVE: NDVI Trends across Alaska and Canada from Landsat, 1984-2012, https://doi.org/10.3334/ORNLDAAC/1576 [WWW Document]. ORNL DAAC, Oak Ridge, Tennessee, USA. https://doi.org/10.3334/ORNLDAAC/1576

Juszak, I., Erb, A.M., Maximov, T.C., Schaepman-Strub, G., 2014. Arctic shrub effects on NDVI, summer albedo and soil shading. Remote Sensing of Environment 153, 79–89. https://doi.org/10.1016/j.rse.2014.07.021

Kauth, R.J., Thomas, G.S., 1976. Purdue e-Pubs The Tasselled Cap-A Graphic Description of the Spectral-Temporal Development of Agricultural Crops as Seen by LANDSAT.

Kennedy, R.E., Yang, Z., Gorelick, N., Braaten, J., Cavalcante, L., Cohen, W.B., Healey, S., 2018. Implementation of the LandTrendr Algorithm on Google Earth Engine. Remote Sensing 2018, Vol. 10, Page 691 10, 691. https://doi.org/10.3390/RS10050691

Campbell, T., Lantz, T.C., Fraser, R.H., Hogan, D., 2021. High Arctic Vegetation Change Mediated by Hydrological Conditions. Ecosystems 24, 106–121. https://doi.org/10.1007/s10021-020-00506-7Kasischke, E.S.; French, N.H.F.; Bourgeau-Chavez, L.L.; Michalek, J.L. 2000. Using satellite data to monitor fire-related processes in boreal forests. In Fire, Climate Change, and Carbon Cycling in the Boreal Forest; Kasischke, E.S., Stocks, B.J., Eds.; Ecological Studies; Springer: New York, NY, USA; pp. 406–422.

Kokelj, S., Tunnicliffe, J., Lacelle, D., Lantz, T.C., Fraser, R.H., 2015. Retrogressive thaw slumps: From slope process to the landscape sensitivity of northwestern Canada. 68e Conférence Canadienne de Géotechnique et 7e Conférence Canadienne sur le Pergélisol, 20 au 23 septembre 2015, Québec, Québec.

Kokelj, S. v, Lantz, T.C., Tunnicliffe, J., Segal, R., Lacelle, D., 2017. Climate-driven thaw of permafrost preserved glacial landscapes, northwestern Canada. Geology 45, 371–374. https://doi.org/10.1130/G38626.1

Krautblatter, M., Leith, K., 2015. Glacier- and permafrost-related slope instabilities. The High-Mountain Cryosphere: Environmental Changes and Human Risks 147–165. https://doi.org/10.1017/CBO9781107588653.009

Labrecque, S., Lacelle, D., Duguay, C.R., Lauriol, B., 2009. Contemporary (1951 - 2001) Evolution of Lakes in the Old Crow Basin, Northern Yukon, Canada: Remote Sensing, Numerical Modeling, and Stable Isotope Analysis. Hawkings Source: Arctic 62, 225–238.

Lacelle, D., Bjornson, J., Lauriol, B., 2010. Climatic and geomorphic factors affecting contemporary (1950-2004) activity of retrogressive thaw slumps on the Aklavik plateau, Richardson mountains, NWT, Canada. Permafrost and Periglacial Processes 21, 1–15. https://doi.org/10.1002/ppp.666

Lacelle, D., Brooker, A., Fraser, R.H., Kokelj, S. v., 2015. Distribution and growth of thaw slumps in the Richardson Mountains-Peel Plateau region, northwestern Canada. Geomorphology 235, 40–51. https://doi.org/10.1016/j.geomorph.2015.01.024

Lacelle, D., Lauriol, B., Clark, I.D., Cardyn, R., Zdanowicz, C., 2007. Nature and origin of a Pleistocene-age massive ground-ice body exposed in the Chapman Lake moraine complex, central Yukon Territory, Canada. Quaternary Research 68, 249–260. https://doi.org/10.1016/j.yqres.2007.05.002

Lacelle, D., St-Jean, M., Lauriol, B., Clark, I.D., Lewkowicz, A., Froese, D.G., Kuehn, S.C., Zazula, G., 2009. Burial and preservation of a 30,000 year old perennial snowbank in Red Creek valley, Ogilvie Mountains, central Yukon, Canada. Quaternary Science Reviews 28, 3401–3413. https://doi.org/10.1016/j.quascirev.2009.09.013

Lantz, T.C., Kokelj, S. v, Gergel, S.E., Henry, G., 2009. Relative impacts of disturbance and temperature: Persistent changes in microenvironment and vegetation in retrogressive thaw slumps. Global Change Biology 15, 1664–1675. https://doi.org/10.1111/j.1365-2486.2009.01917.x

Lantz, T.C., Turner, K.W., 2015. Changes in lake area in response to thermokarst processes and climate in Old Crow Flats, Yukon. Journal of Geophysical Research: Biogeosciences 120, 513–524. https://doi.org/10.1002/2014JG002744

Lara, M.J., Nitze, I., Grosse, G., Martin, P., Mcguire, A.D., 2018. Reduced arctic tundra productivity linked with landform and climate change interactions. Scientific Reports 8, 2345–2350. https://doi.org/10.1038/s41598-018-20692-8

Latifovic, R., Pouliot, D., Olthof, I., 2017. Circa 2010 Land Cover of Canada: Local Optimization Methodology and Product Development. Remote Sensing 9, 1098. https://doi.org/10.3390/rs9111098

Lauriol, B., Lacelle, D., Labrecque, S., Duguay, C.R., Telka, A., 2009. Holocene evolution of lakes in the Bluefish Basin, Northern Yukon, Canada. Arctic 62, 212–224.

LaZerte S, Albers S (2018). weathercan: Download and format weather data from Environment and Climate Change Canada. The Journal of Open Source Software, 3(22), 571. <https://joss.theoj.org/papers/10.21105/joss.00571>.

Lewkowicz, A.G., Way, R.G., 2019. Extremes of summer climate trigger thousands of thermokarst landslides in a High Arctic environment. Nature Communications 2019 10:1 10, 1–11. https://doi.org/10.1038/s41467-019-09314-7

Liljedahl, A.K., Boike, J., Daanen, R.P., Fedorov, A.N., Frost, G. v, Grosse, G., Hinzman, L.D., Iijma, Y., Jorgenson, J.C., Matveyeva, N., Necsoiu, M., Raynolds, M.K., Romanovsky, V.E., Schulla, J., Tape, K.D., Walker, D.A., Wilson, C.J., Yabuki, H., Zona, D., 2016. Pan-Arctic ice-wedge degradation in warming permafrost and its influence on tundra hydrology. Nature Geoscience 9, 312–318. https://doi.org/10.1038/ngeo2674

McClelland, J.W., Déry, S.J., Peterson, B.J., Holmes, R.M., Wood, E.F., 2006. A pan-arctic evaluation of changes in river discharge during the latter half of the 20th century. Geophysical Research Letters 33, 2–5. https://doi.org/10.1029/2006GL025753

Mckenney, D.W., Hutchinson, M.F., Papadopol, P., Lawrence, K., Pedlar, J., Campbell, K., Milewska, E., Hopkinson, R.F., Price, D., Owen, T., 2011. Customized spatial Climate models for North ameriCa. Bulleting of American Meteorological Society 92, 1611–1622. https://doi.org/10.1175/Bams-d-10-3132.1

Myers-Smith, I.H., Harden, J.W., Wilmking, M., Fuller, C.C., McGuire, A.D., Chapin, F.S., 2008. Wetland succession in a permafrost collapse: Interactions between fire and thermokarst. Biogeosciences 5, 1273–1286. https://doi.org/10.5194/BG-5-1273-2008

National Research Council, 2014. Opportunities to Use Remote Sensing in Understanding Permafrost and Related Ecological Characteristics: Report of a Workshop, Opportunities to Use Remote Sensing in Understanding Permafrost and Related Ecological Characteristics. National Academies Press. https://doi.org/10.17226/18711

Necsoiu, M., Dinwiddie, C.L., Walter, G.R., Larsen, A., Stothoff, S.A., 2013. Multi-temporal image analysis of historical aerial photographs and recent satellite imagery reveals evolution of water body surface area and polygonal terrain morphology in Kobuk Valley National Park, Alaska. Environmental Research Letters 8. https://doi.org/10.1088/1748-9326/8/2/025007

Nitze, I., 2022. Google Earthengine HotSpot Regions of Permafrost Change Production and Visualization [WWW Document]. URL https://ingmarnitze.users.earthengine.app/view/hotspottcvisapp#lon=0;lat=50;zoom=5;

Nitze, I., Grosse, G., 2016. Detection of landscape dynamics in the Arctic Lena Delta with temporally dense Landsat time-series stacks. Remote Sensing of Environment 181, 27–41. https://doi.org/10.1016/J.RSE.2016.03.038

Nitze, I., Grosse, G., Jones, B.M., Arp, C.D., Ulrich, M., Fedorov, A., Veremeeva, A., 2017. Landsat-based trend analysis of lake dynamics across Northern Permafrost Regions. Remote Sensing 9. https://doi.org/10.3390/rs9070640

Nitze, I., Grosse, G., Jones, B.M., Romanovsky, V.E., Boike, J., 2018. Remote sensing quantifies widespread abundance of permafrost region disturbances across the Arctic and Subarctic. Nature Communications 2018 9:1 9, 1–11. https://doi.org/10.1038/s41467-018-07663-3

NWT Centre for Geomatics, 2021. Image Service: Landsat Long-Term Change Detection [WWW Document]. URL https://www.image.geomatics.gov.nt.ca/arcgis/rest/services/Mosaics/LongTermChangeDetection_TasseledCapResult/ImageServer

O'Donnell, J.A., Harden, J.W., Mcguire, A.D., Kanevskiy, M.Z., Jorgenson, M.T., Xu, X., 2011. The effect of fire and permafrost interactions on soil carbon accumulation in an upland black spruce ecosystem of interior Alaska: implications for post-thaw carbon loss. Global Change Biology 17, 1461–1474. https://doi.org/10.1111/J.1365-2486.2010.02358.X

Olthof, I., Fraser, R.H., 2014. Detecting landscape changes in high latitude environments using landsat trend analysis: 2. classification. Remote Sensing 6, 11558–11578. https://doi.org/10.3390/rs61111558

Olthof, I., Pouliot, D., Latifovic, R., Chen, W., 2008. Recent (1986–2006) Vegetation-Specific NDVI Trends in Northern Canada from Satellite Data, ARCTIC.

Osterkamp, T.E., Jorgenson, M.T., Schuur, E.A.G., Shur, Y.L., Kanevskiy, M.Z., Vogel, J.G., Tumskoy, V.E., 2009. Physical and ecological changes associated with warming permafrost and thermokarst in Interior Alaska. Permafrost and Periglacial Processes 20, 235–256. https://doi.org/10.1002/ppp.656

Pironkova, Z., Whaley, R., Lan, K., 2018. Time series analysis of Landsat NDVI composites with Google Earth Engine and R: User guide, Science and Research.

Raynolds, M.K., Walker, D.A., 2016. Increased wetness confounds Landsat-derivedNDVI trends in the central Alaska North Sloperegion, 1985–2011. https://doi.org/10.1088/1748-9326/11/8/085004

Raynolds, M.K., Walker, D.A., Ambrosius, K.J., Brown, J., Everett, K.R., Kanevskiy, M., Kofinas, G.P., Romanovsky, V.E., Shur, Y., Webber, P.J., 2014. Cumulative geoecological effects of 62 years of infrastructure and climate change in ice-rich permafrost landscapes, Prudhoe Bay Oilfield, Alaska. Global Change Biology 20, 1211–1224. https://doi.org/10.1111/gcb.12500

Ritchie, J.C., 1984. Past and present vegetation of the far northwest of Canada. Past and present vegetation of the far northwest of Canada. https://doi.org/10.2307/2260178

Roberts, D.A., Ustin, S.L., Ogunjemiyo, S., Greenberg, J., Dobrowski, S.Z., Chen, J., Hinckley, T.M., 2004. Spectral and Structural Measures of Northwest Forest Vegetation at Leaf to Landscape 7, 545–562. https://doi.org/10.1007/sl0021-004-0144-5

Rocha, A. v., Loranty, M.M., Higuera, P.E., MacK, M.C., Hu, F.S., Jones, B.M., Breen, A.L., Rastetter, E.B., Goetz, S.J., Shaver, G.R., 2012. The footprint of Alaskan tundra fires during the past half-century: implications for surface properties and radiative forcing. Environmental Research Letters 7, 044039. https://doi.org/10.1088/1748-9326/7/4/044039

Romanovsky, V.E., et al., 2017. Changing permafrost and its impacts, in: Snow, Water, Ice and Permafrost in the Arctic (SWIPA). Arctic Monitoring and Assessment Programme (AMAP), pp. 65–102.

Roy, D.P., Kovalskyy, V., Zhang, H.K., Vermote, E.F., Yan, L., Kumar, S.S., Egorov, A., 2016. Characterization of Landsat-7 to Landsat-8 reflective wavelength and normalized difference vegetation index continuity. Remote Sensing of Environment 185, 57–70. https://doi.org/10.1016/j.rse.2015.12.024

Segal, R.A., Lantz, T.C., Kokelj, S. v, 2016. Acceleration of thaw slump activity in glaciated landscapes of the Western Canadian Arctic. Environmental Research Letters 11, 34025. https://doi.org/10.1088/1748-9326/11/3/034025

Senf, C., Pflugmacher, D., Wulder, M.A., Hostert, P., 2015. Characterizing spectral-temporal patterns of defoliator and bark beetle disturbances using Landsat time series. Remote Sensing of Environment 170, 166–177. https://doi.org/10.1016/j.rse.2015.09.019

Short, N., Brisco, B., Couture, N., Pollard, W., Murnaghan, K., Budkewitsch, P., 2011. A comparison of TerraSAR-X, RADARSAT-2 and ALOS-PALSAR interferometry for monitoring permafrost environments, case study from Herschel Island, Canada. Remote Sensing of Environment 115, 3491–3506. https://doi.org/10.1016/J.RSE.2011.08.012

Steedman, A.E., Lantz, T.C., Kokelj, S. v., 2017. Spatio-Temporal Variation in High-Centre Polygons and Ice-Wedge Melt Ponds, Tuktoyaktuk Coastlands, Northwest Territories. Permafrost and Periglacial Processes 28, 66–78. https://doi.org/10.1002/PPP.1880

St-Jean, M., Lauriol, B., Clark, I.D., Lacelle, D., Zdanowicz, C., 2011. Investigation of ice-wedge infilling processes using stable oxygen and hydrogen isotopes, crystallography and occluded gases (O2, N2, Ar). Permafrost and Periglacial Processes 22, 49–64. https://doi.org/10.1002/ppp.680

Stow, D.A., Hope, A., McGuire, D., Verbyla, D., Gamon, J., Huemmrich, F., Houston, S., Racine, C., Sturm, M., Tape, K., Hinzman, L., Yoshikawa, K., Tweedie, C., Noyle, B., Silapaswan, C., Douglas, D., Griffith, B., Jia, G., Epstein, H., Walker, D., Daeschner, S., Petersen, A., Zhou, L., Myneni, R., 2004. Remote sensing of vegetation and land-cover change in Arctic Tundra Ecosystems. Remote Sensing of Environment 89, 281–308. https://doi.org/10.1016/j.rse.2003.10.018

Talucci, A.C., Loranty, M.M., Alexander, H.D., 2022. Siberian taiga and tundra fire regimes from 2001–2020. Environmental Research Letters 17, 025001. https://doi.org/10.1088/1748-9326/AC3F07

Toohey, R.C., Herman-Mercer, N.M., Schuster, P.F., Mutter, E.A., Koch, J.C., 2016. Multidecadal increases in the Yukon River Basin of chemical fluxes as indicators of changing flowpaths, groundwater, and permafrost. Geophysical Research Letters 43, 12,120-12,130. https://doi.org/10.1002/2016GL070817

U.S. Geological Survey, 2020. Landsat 4-7 Collection 1 (C1) Surface Reflectance (LEDAPS) Product Guide.

U.S. Geological Survey, 2016. Landsat 7 (L7) Enhanced Thematic Mapper Plus (Etm+) Level 1 (L1) Data Format Control Book (DFCB).

van der Sluijs, J., Kokelj, S., Fraser, R., Tunnicliffe, J., Lacelle, D., 2018. Permafrost Terrain Dynamics and Infrastructure Impacts Revealed by UAV Photogrammetry and Thermal Imaging. Remote Sensing 10, 1734. https://doi.org/10.3390/rs10111734

Vowles, T., Björk, R.G., 2019. Implications of evergreen shrub expansion in the Arctic. Journal of Ecology 107, 650–655. https://doi.org/10.1111/1365-2745.13081

Vuorinen, K.E.M., Oksanen, L., Oksanen, T., Pyykönen, A., Olofsson, J., Virtanen, R., 2017. Open tundra persist, but arctic features decline—Vegetation changes in the warming Fennoscandian tundra. Global Change Biology 23, 3794–3807. https://doi.org/10.1111/GCB.13710

Walvoord, M.A., Striegl, R.G., 2007. Increased groundwater to stream discharge from permafrost thawing in the Yukon River basin: Potential impacts on lateral export of carbon and nitrogen. Geophysical Research Letters 34, 12402. https://doi.org/10.1029/2007GL030216

Ward Jones, M.K., Pollard, W.H., Jones, B.M., 2019. Rapid initialization of retrogressive thaw slumps in the Canadian high Arctic and their response to climate and terrain factors. Environmental Research Letters 14. https://doi.org/10.1088/1748-9326/ab12fd

Weijers, S., Pape, R., Löffler, J., Myers-Smith, I.H., 2018. Contrasting shrub species respond to early summer temperatures leading to correspondence of shrub growth patterns. Environmental Research Letters 13, 034005. https://doi.org/10.1088/1748-9326/AAA5B8

Wesche, S.D., Chan, H.M., 2010. Adapting to the Impacts of Climate Change on Food Security among Inuit in the Western Canadian Arctic. Ecohealth 7, 361–373. https://doi.org/10.1007/s10393-010-0344-8

White, D.M., Craig Gerlach, S., Loring, P., Tidwell, A.C., Chambers, M.C., 2007. Food and water security in a changing arctic climate. https://doi.org/10.1088/1748-9326/2/4/045018

Wilson, S.D., Nilsson, C., 2009. Arctic alpine vegetation change over 20 years. Global Change Biology 15, 1676–1684. https://doi.org/10.1111/J.1365-2486.2009.01896.X

Yukon Parks, 2009. Tombstone Territorial Park Management Plan. Government of Yukon, 108 p.

CHAPTER 4: A PROCESS-BASED MODEL OF ACTIVE LAYER THICKNESS AND PERMAFROST CONDITIONS IN TOMBSTONE TERRITORIAL PARK (CENTRAL YUKON).

Abstract

Air temperatures have increased at an accelerated rate in northern regions, and permafrost is expected to experience change to its thermal regime, which could result in degradation. The relationships between permafrost and local geo-ecological factors leads to a complex representation of permafrost distribution involving climate-ecosystem interactions which need to be taken into account to obtain a full picture of the thermal dynamics of permafrost. In this study, permafrost distribution and thermal conditions in the Ogilvie Mountains, Central Yukon, were modeled for past, current and future conditions under different climate scenarios using the Northern Ecosystem Soil Temperature (NEST) model, a process-based models that integrates the effects of climate, vegetation, ground features and hydrological dynamics. Results indicate that permafrost has persisted through the 20th century and beginning of the 21st century and is currently present throughout the study area. Modeled mean permafrost depth (113.8 ± 49.6 m), mean ALT (2.45 ± 7 m), mean surface temperature (−1 ± 1.2°C), mean near-surface temperature (−1.6 ± 1.2°C) and mean deep temperature (−2.4 ± 1.3°C) are in the range of other local and regional measurements. Predicted ALTs and permafrost depth show areas of permafrost loss by 2100 under both RCP4.5 and RCP8.5 (22%-29% of study area). Permafrost in the study area most likely went from being climate-driven in the Pleistocene to ecosystem-driven in the mid-Holocene, and it might become ecosystem-protected in the 21st century. Permafrost degradation in the study area could greatly impact slope stability and conditions of aquatic systems, and shrubification could contribute to increased degradation.

4.1.Introduction

Air temperatures have increased at an accelerated rate in northern regions, and permafrost is expected to experience change to its thermal regime, which could result in degradation (Arctic Monitoring and Assessment Programme (AMAP), 2017; Jorgenson et al., 2010). Permafrost occurrence and persistence is dictated by a number of complex interactions between climate, topography, the physical properties of the ground, soil moisture, drainage, snow cover, waterbodies, fire, and vegetation, which can lead to positive and negative feedbacks to permafrost existence and sensitivity to climatic conditions (Shur and Jorgenson, 2007; Jorgenson et al., 2010). The relationships between permafrost and the local geo-ecological factors leads to a complex representation of permafrost distribution involving climate-ecosystem interactions which need to be taken into account to accurately define permafrost distribution, sensitivity, stability and ability to recover after disturbances (Shur and Jorgenson, 2007). While mapping and modeling permafrost based on geomorphological, topographic and climatic variables is useful in determining the large-scale distribution of permafrost (e.g. Brown et al., 1997; Bonnaventure et al., 2012; Heginbottom et al., 1995; O'Neill et al., 2019), addressing the variety of geo-ecological factors determining permafrost distribution and sensitivity is crucial to obtain a full picture of the thermal dynamics of permafrost environments (Zhang et al., 2003).

The Tombstone Territorial Park, located in the Ogilvie Mountains, Central Yukon, is a permafrost niche because of its higher elevations and colder air temperatures. Despite the many geomorphic features indicative of the presence of icy permafrost, a recent study has found little evidence of recent (1986-2021) substantial changes to permafrost-related features in the area (Frappier et al., in press). Given the local variabilities associated with ground ice contents, elevations and vegetation cover, small-scale investigation is necessary to establish the state of permafrost and sensitivity of the study area to climate and surface disturbances. The increased availability of high- to mid-resolution products allow for such investigations to be taken at the regional scale. In this study, permafrost distribution and thermal conditions in the Ogilvie Mountains were modeled for past, current and future conditions under different climate scenarios using the Northern Ecosystem Soil Temperature (NEST) model, a process-based models that integrates the effects of climate, vegetation, ground features and hydrological dynamics (Zhang et al., 2003). This model has been validated against energy fluxes, snow depths, soil temperatures, thaw depths, and permafrost and thermal conditions distribution across Canada (Zhang et al., 2012). It has been used to simulate the distribution and sensitivity of permafrost across a variety of landscapes. For instance, it has been applied to assess the effects of climate change since the end of the Little Ice Age in Canada (Zhang, Chen and Riseborough, 2006), to model and map permafrost in the Hudson Bay Lowlands in northern Ontario (Ou et al., 2016; Zhang et al., 2012), to characterise isolated patches of permafrost on the coast of Labrador (Way, Lewkowicz and Zhang, 2018), and it has also been integrated with a biogeochemical model to upscale methane fluxes from plant communities to ecosystem scale in permafrost peatlands in the Lena River Delta in Russia (Zhang et al., 2012). For the first time, the model was used to characterise permafrost in a mountainous region. The goals of this paper are to 1) provide detailed maps of permafrost distribution and thermal conditions in the TTP and surrounding areas of the Ogilvie Mountains, 2) evaluate their change under different climate scenarios, and 3) test the application of the NEST model in a mountainous region.

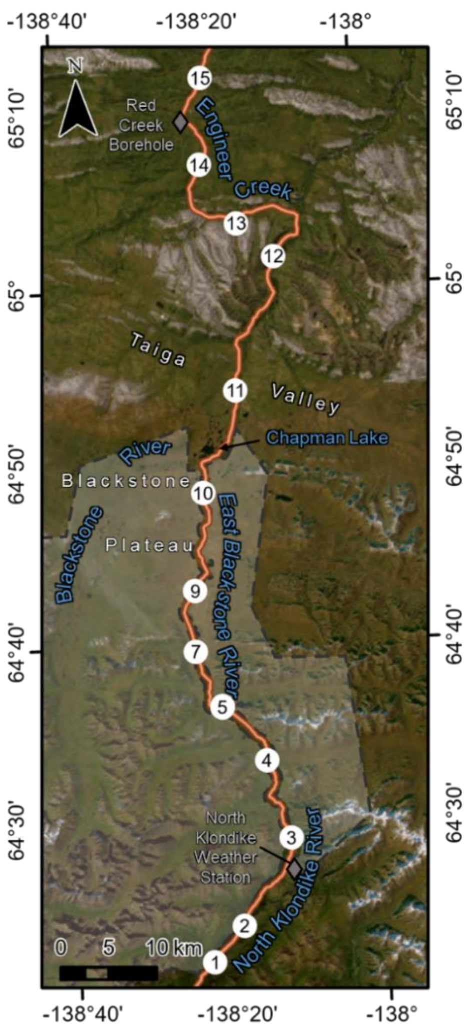

Figure 4.1 Study area location map with distribution of field observation sites (white circles) in and near Tombstone Territorial Park, Central Yukon (shaded grey area). Dempster Highway is shown in red.

4.2. Study Area

The study area encompasses the Tombstone Territorial Park (TTP) in the North Ogilvie Mountains in Central Yukon, and extends >40 km to the North along the Dempster Highway into Engineer Creek valley (**Fig. 4.1**). Elevations range between 668 and 2344 m a.s.l. (**Fig. 4.2**). Four main river valleys run through the region: the North Klondike River flowing southward in the southern part of the study area; the Blackstone and East Blackstone Rivers flowing northward and merging at the northern boundary of TTP, near Chapman Lake; and Engineer Creek flowing northward in the northern part of the study area. Most of the region has been ice-free since the late Pleistocene (McConnell Glaciation, MIS2), and some of the areas north of the region have remained unglaciated since at least the mid-Pleistocene (Reid Glaciation, MIS4/6). Surficial deposits are dominated by Holocene colluvium (ca. 67%), with scattered Late Pleistocene morainal deposits (ca. 18%) and Holocene alluvial plains deposits (ca. 10%) (Thomas and Rampton, 1982). The highest elevations are barren lands (ca. 25% of total study area), and the lowest elevations are covered by boreal forest (ca. 8%). Shrubland tundra (ca. 19%) is found in the transition between the forest and grassland tundra (ca. 40%), which is widespread in the northern part of the study area (Latifovic et al., 2017).

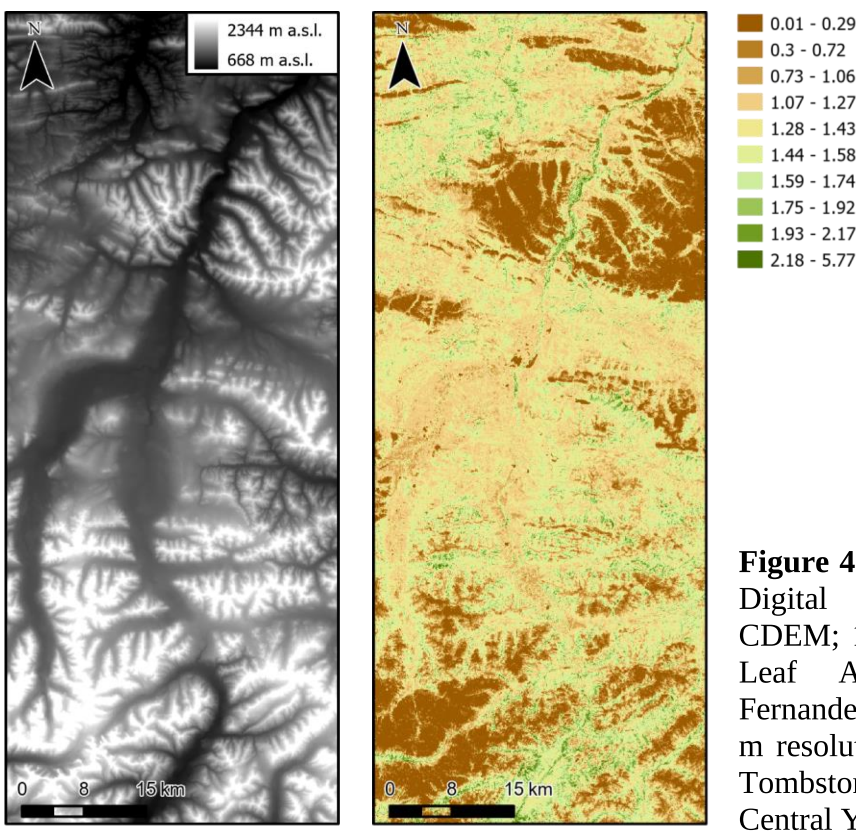

Figure 4.2 Elevation (Canada Digital Elevation Model; CDEM; 15 m resolution) and Leaf Area Index (LAI; Fernandes and Sun, 2021; 30 m resolution) in and near the Tombstone Territorial Park, Central Yukon.

According to the Köppen-Geiger Climate Classification, the higher elevations of the Ogilvie Mountains correspond to the tundra polar climate, while the lower elevations correspond to the subarctic climate (Beck et al., 2018). Gridded historical climate data reports a mean annual air temperature (MAAT) of −7.9°C for the 1950-2013 period (mean January temperature: −26.9°C; mean July temperature: 11.5°C), and a mean thawing index of 1086.6°C-days (Mckenney et al., 2011). In winter, the mountainous topography often traps Arctic air masses that create cold spells with air temperatures below −40°C (Hu and Pollard, 1997). A meteorological station located within the study area (North Klondike River, 64.45°N, 138.22°W, 972 m a.s.l.) reports an average of 472 mm of total precipitations with c. 48% falling as snow for the 1967-2006 period.

The presence of buried glacial ice indicate that permafrost has persisted, at least locally, since the late Pleistocene (Lacelle et al., 2009, 2007). Permafrost-related features such as ice-wedge (IW) polygons, icings, and pingos are present within the Blackstone and East Blackstone river valleys, and rock glaciers are widespread in the southern and eastern part of the study area (Frappier and Lacelle, 2021; Frappier et al., in press). Existing permafrost distribution models indicate permafrost to be continuous in the higher elevations, with extensive discontinuous to sporadic permafrost present in valley bottoms and plateaus (Obu et al., 2019; Bonnaventure et al., 2012). A shallow borehole located within the study area ca. 10 km from the northern boundary (Red Creek borehole) reported average ground temperatures of ca. −2.5°C in 2007, which, assuming a typical geothermal gradient of 1°C per 30-60 m, indicates a permafrost thickness ranging between 75 to 150 m (Lacelle et al., 2009). In Dawson City, ca. 58 km south-west of our study area, permafrost thicknesses up to 60 m have been reported (Smith et al., 2004).

4.3. Methods

4.3.1. The model

The Northern Ecosystem Soil Temperature (NEST) model (Zhang et al., 2003) builds on field observations, remote sensing and process-based modelling approaches and integrates the effects of: 1) climate (daily minimum and maximum air temperature, precipitation, fraction of snowfall, solar radiation, vapor pressure, wind speed, and downward longwave radiation); 2) topography (slope, aspect and solar radiation viewshed angles); 3) vegetation (type and height of landcover, leaf area index in peak growing season, albedo, and effects of wildfires, if applicable); 4) ground features (organic matter fraction and degree of decomposition, mineral soil texture, fraction of stones and excess ice); and 5) hydrological dynamics (water input and output, water table depth, surface and ground lateral inflow and outflow, snow compaction, metamorphism and redistribution). The modeled ground profile is divided in 62 layers of thicknesses increasing from 0.1 m near the surface to 4.8 m at the base of the profile, which has a total depth of 120 m. Ground temperature dynamics are then simulated by solving the one-dimensional heat conduction equation, where the upper boundary condition is determined based on energy balance, and the lower boundary condition is defined based on geothermal heat flux. Detailed description and validation of the model are presented in Zhang et al. (2003), and improvements to the model are described in Zhang et al. (2012, 2015 and 2018) and Zhang (2013).

The NEST model was first calibrated using measured ground temperatures taken at 15 monitoring sites in the study area (**Table 4.1**) between August 2021 and July 2022. Ground temperature data was retrieved using iButtons loggers (accuracy ±1°C) recording every 255 minutes (average of six measurements per day). Shallow (15 cm of depth) and deep (35-70 cm of depth) ground temperature were measured. The deepest loggers were inserted at the depth of thaw in mid- to late-summer at 9 out of the 15 sites (Way and Lewkowicz, 2018; Way et al., 2018). Model outputs were validated against thaw layer depth measurements taken in August 2021 at 11 of the 15 sites (exceeded probing depth or was too rocky at four other sites), and from other research (Grinter et al., 2019; Calmels et al., 2018; Lacelle et al., 2009). Then, the NEST model was used to calculate ground temperatures, freezing depth, active layer thickness and permafrost conditions under two Representative Concentration Pathways; RCP4.5 and RCP8.5. RCP4.5 is an intermediate scenario in which total radiative forcing is stabilizing shortly after 2100, and it corresponds to many non-climate policy scenarios, as well as some climate policy scenarios. RCP8.5 is a high emission scenario in which a rise in total radiative forcing is predicted by 2100, and it corresponds to very high range non-climate policy scenarios (van Vuuren et al., 2011). Comparing these two climate RCPs allows for assessment of the effects of both intermediate climate changes and higher-range climate changes on permafrost in the study area.

Table 4.1 Monitoring sites information and description

ID	Lat	Long	Elevation (m a.s.l.)	Slope (°)	Aspect (°)	OLT[1] (cm)	TLT[2] (cm)	Shallow temp. logger depth (cm)	Deep temp. logger depth (cm)	Landcover type	Surficial deposit
1	64.37	-138.38	864.2	3.4	326.8	28	>100	15	-	Boreal forest	Alluvium
2	64.40	-138.31	907.7	6.7	158.1	15	>100	15	-	Boreal forest	Alluvium
3	64.48	-138.20	1002.4	0.9	346.6	12	60	15	60	Boreal forest	Alluvium
4	64.56	-138.25	1260.2	1.5	233.7	3	56	15	-	Shrubland tundra	Glaciofluvial
5	64.61	-138.34	1186.2	2.9	341.7	0	-	15	-	Grassland tundra	Glaciofluvial
6	64.61	-138.34	1186.2	2.9	341.7	15	47	15	47	Grassland tundra	Glaciofluvial
7	64.66	-138.39	1138.7	0.2	290.8	27	36	15	36	Ice-wedge polygon (dry rim)	Glaciofluvial
8	64.66	-138.39	1138.7	0.2	290.8	37	54	15	54	Ice-wedge polygon (low wet center)	Glaciofluvial
9	64.72	-138.39	1112.9	0.3	110.9	8	35	15	35	Ice-wedge polygon (high center)	Alluvium
10	64.81	-138.36	1034.4	5.0	72.9	10	41	15	41	Ice-wedge polygon (high center)	Moraine
11	64.90	-138.28	955.3	1.3	71.8	13	44	15	44	Grassland tundra	Glaciofluvial
12	65.03	-138.18	910.2	15.0	110.6	15	>100	15	50	Boreal forest	Alluvium
13	65.06	-138.26	1077.8	4.6	268.0	20	70	15	70	Grassland tundra	Alluvium
14	65.12	-138.34	843.4	1.2	110.7	40	40	15	40	Grassland tundra	Alluvium
15	65.20	-138.33	729.9	0.7	75.0	50	50	15	50	Shrubland tundra	Alluvium

[1] Organic layer thickness, based on measurements taken in July 2021 [2] Thaw layer thickness, based on probing measurements taken in July 2021

4.3.2. Model parametrization

The model was parametrize using field, remote sensing and regional climate data. Properties of the soil, including soil texture, organic matter content and degree of decomposition, excess ice content and stone content (>2mm), vegetation composition and height, and snow depth were determined in the field at the 15 monitoring sites. Detailed monitoring sites information and description are shown in **Table 4.1**.

Remote sensing data include: a) elevation (Canadian Digital Elevation Model; resolution: 16 m) to determine slope, aspect and solar radiation viewshed; b) maximum leaf area index (LAI) during the 2020 growing season (June to August) at 30 m resolution (Fernandes and Sun, 2021); c) landcover which was determined based on the 30 m resolution Land Cover of North America (Latifovic et al., 2017), and; d) MODIS-derived albedo during peak phenology season in the summer of 2016 (July 7th and 15th 2016) (Solvik et al., 2019).

A regional climate dataset spanning from 1901 to 2100 (**Fig. 4.3**) was derived using a continuous daily gridded meteorological dataset (Met1km) which was developed specifically for modeling and mapping permafrost at high spatial resolutions in Canada and whose accuracy is similar or better compared to other gridded meteorological datasets (Zhang et al., 2020). The

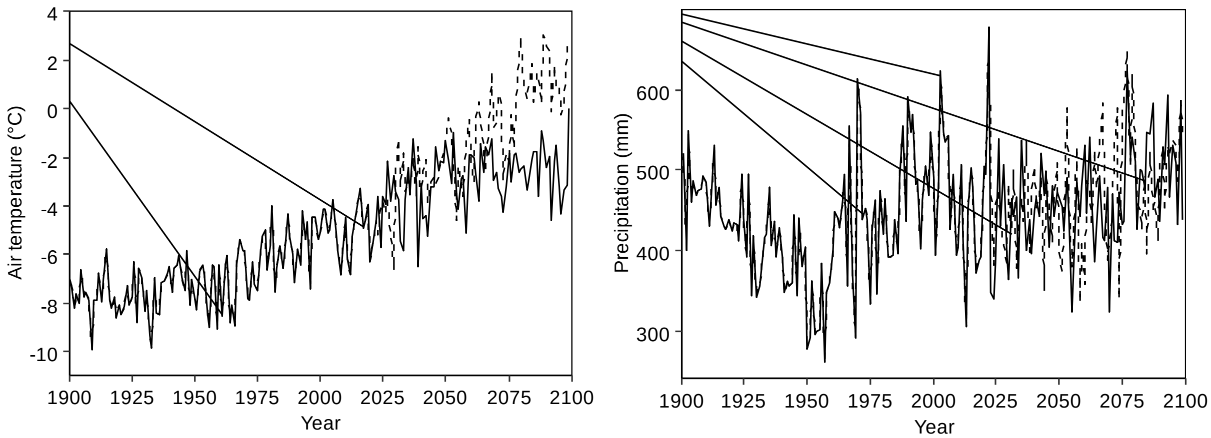

Figure 4.3 Mean annual air temperatures and mean annual precipitation for the study area from 1901 to 2100. Future predictions generated for both RCP4.5 (solid line) and RCP 8.5 (dashed line).

dataset was calibrated using three weather stations; one in the study area with less data available (North Klondike River station, 64.45°N, 138.22°W, 972 m a.s.l.), and two south of the study area with more data available (Dawson A and Dawson City stations, 64.04°N, 139.13°W, 370 m a.s.l.) (Environment and Climate Change Canada, 2022) by determining transformation coefficients. When no widespread measurements of ground temperatures and soil conditions exist to initialize the model, typical climate conditions from the beginning of the climate datasets are used for initialization (Zhang et al., 2012). All climate data beginning in 1900 was therefore used to run the model iteratively until ground thermal conditions reached stability.

The climate dataset estimates an increase of 2.9°C in MAAT from the 1900s (1901-1910; $\bar{x} = -7.9$°C) to the 2010s (2011-2020; $\bar{x} = -4.9$°C), and increases of 2.3°C from the 2010s to the 2090s (2091-2100) under RCP4.5 ($\bar{x} = -2.7$°C), and 6.3°C under RCP8.5 ($\bar{x} = 1.4$°C) (**Fig. 4.3**). Mean annual precipitations were estimated to decrease by 50.5 mm from the 1900s (1901-1910; $\bar{x} = 481.8$ mm) to the 2010s (2011-2020; $\bar{x} = 431.3$ mm), and mean annual precipitations increases of 71.3 mm are predicted from the 2010s to the 2090s (2091-2100) under RCP4.5 ($\bar{x} = 502.57$), and 89.9 mm under RCP8.5 ($\bar{x} = 521.2$ mm) (**Fig. 4.3).**

4.3.3. Modeling active layer and permafrost thermal regime

Model calibration using the 15 field sites showed that the most influential parameters for ground thermal regime were the snow-drifting factor, top soil organic layer thickness, and organic matter content in top layers. Previous studies have also shown that the most important factors determining the spatial distribution of active layer thickness are landcover type and organic layer thickness because of their direct impacts on ground thermal conditions (Zhang et al., 2012; Ou et al., 2016). In contrast, small variations in parameters such as aspect, slope and albedo do not significantly affect the output from the NEST model (Zhang et al., 2012). To illustrate this, landcover types classes were created at a 30 m resolution by combining landcover and surficial deposits (**Fig. 4.4**) (Latifovic et al. 2017; Thomas and Rampton, 1982), and integrating LAI values (Fernandes and Sun, 2021) which were divided into 10 discrete classes ranging from 0.2 to 4 (**Fig. 4.2**). An additional class was created to illustrate the presence of IW polygons in the study area (Frappier and Lacelle, 2021). This resulted in 453 unique landcover type classes. The effects of elevation and topography are strongly represented by the LAI values and vegetation cover as can be seen in the elevation ranges and mean of each landcover and LAI class (**Fig. 4.5**). The calibration exercise also showed that slope, aspect and viewshed had little to no impact on modeled ground temperatures. Therefore, topography was not integrated in the model for simplicity.

Snow-drifting factor, organic layer thickness, mineral soil texture and thickness of soil were derived for each landcover type class based on field observations and ancillary data including surficial deposits and geology (Thomas and Rampton, 1982; GSG, 2018; Duk-Rodkin, 1996). The model was run for each landcover type class and the results were applied to all 30 m x 30 m pixels covering the study area corresponding to each landcover type class (Zhang et al., 2012). 10-year mean depth to permafrost base, active layer thickness (ALT), surface ground temperatures (5 cm depth; MAST), near-surface ground temperatures (15 cm depth; MANST) and deep ground temperatures (2 m depth; MADT) were computed for two decades (2011-2020 and 2091-2100) and mapped to assess their distribution and change under climate scenarios. These depths were chosen for ground temperature analysis because they are simple and commonly used to assess permafrost thawing (Jorgenson et al., 2010). Future predictions (2091-2100) were analyzed for both RCP4.5 and RCP8.5. While permafrost is defined as ground that remains at or below 0°C for at least two consecutive years (van Everdingen, 2005), for this study, permafrost was considered non-existent in any area where an annual frozen layer was absent for 6 or more years within the decade (Ou et al., 2012). The distribution of the 2011-2020 means and the change between 2011-2020 and 2091-2100 were compared with surficial geology, vegetation cover, landcover types and LAI distributions. The relative frequency distribution were normalized to the relative frequency distribution of these different landscape factors to determine which ones are determinant of ALTs and permafrost distribution and change.

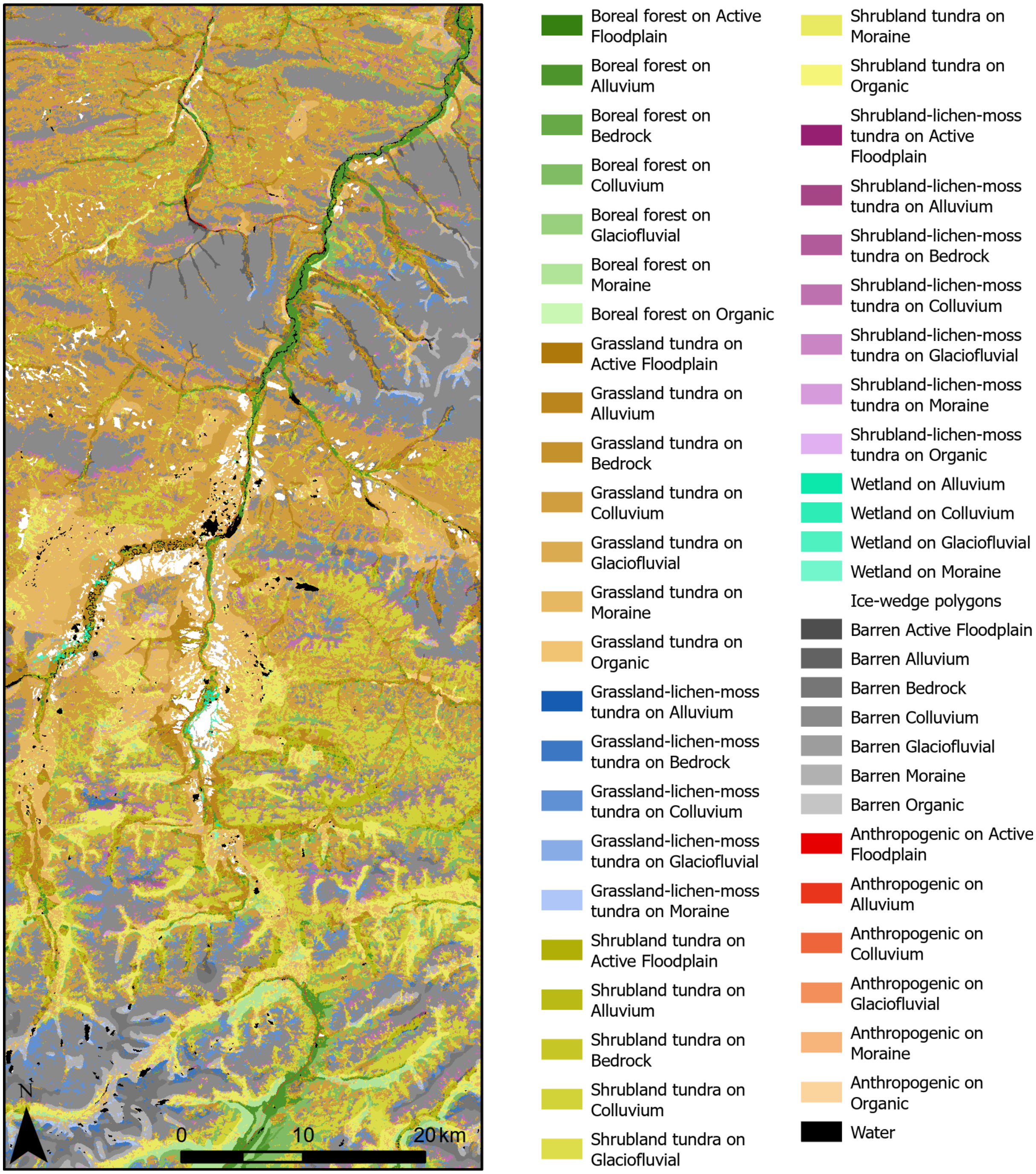

Figure 4.4 Landcover types incorporating vegetation cover, surficial deposits and the presence of ice-wedge polygons in and near the Tombstone Territorial Park, Central Yukon.

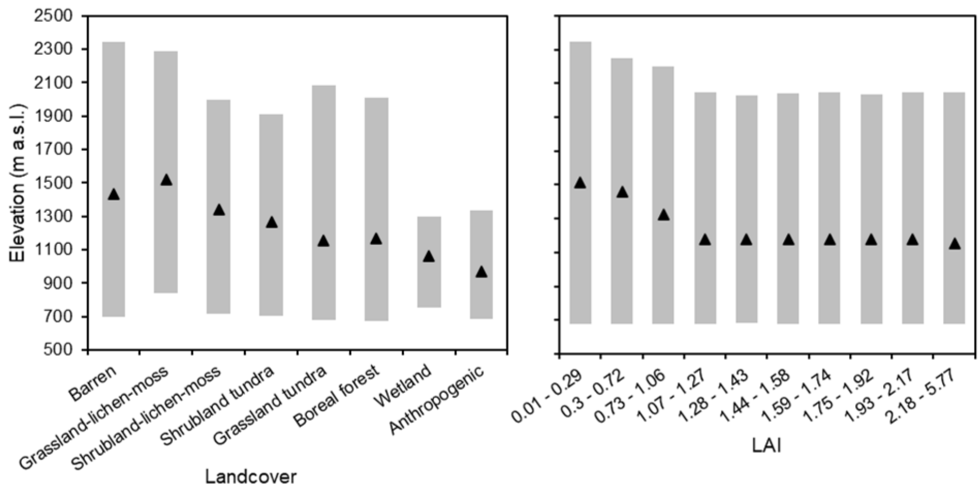

Figure 4.5 Elevation ranges (bar) and mean (triangle) of landcover and leaf-area-index (LAI) classes

1.1. Results

1.1.1. Model calibration and validation

Mean annual absolute difference between modeled and measured temperatures at 15 cm below the surface was ±1.2°C, with a root-mean-square error (RMSE) of 1.6°C (**Fig. 4.6a**). These modeled temperatures are slightly overestimated for measured temperatures above 0°C and below −6°C, and slightly underestimated between 0 and −6°C. Examination of individual sites reveals how the underestimation is associated with winter freeze onset which is often earlier in modeled data compared to the measurements (**Fig. 4.7**). This seems to be typical of IW polygons (sites 7, 8, 9 and 10), although other sites also show a similar delay. It could be related to high moisture contents which result in heat energy being spent freezing water rather than cooling the ground. Deep temperature for the 9 sites where thermistors were installed at the base of the mid- to late-summer thaw layer report an annual mean absolute difference (MD) of 0.8°C and a RMSE of 1.2°C (**Fig. 4.6b**). Modeled deep temperatures are slightly underestimated between -1 and -7°C. Looking at individual sites, all six grassland tundra and IW polygons sites are in very good agreement, especially for winter temperatures (**Fig. 4.7**). The other three sites are located in the boreal forest and the model did not perform as well in modeling those deeper temperatures.

Model outputs were validated against thaw layer depths measurements taken in August 2021 at 11 of the 15 monitored sites (exceeded probing depth of 1 m at sites 1, 2 and 12, and too rocky at site 5), and from other research (Grinter et al., 2021; Calmels et al., 2018; Lacelle et al.,

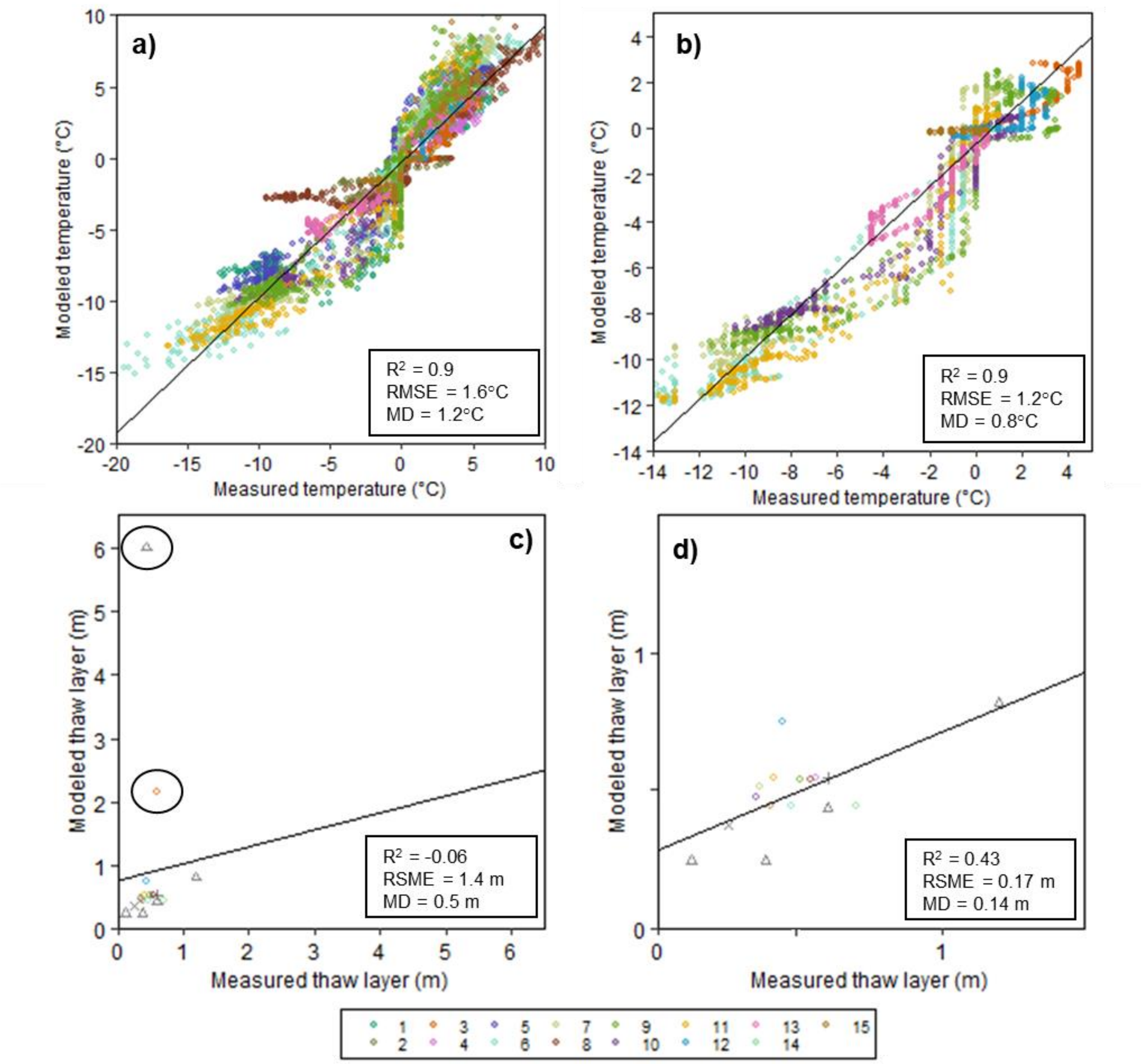

Figure 4.6 Scatterplot showing comparison of the modeled and measured a) shallow (15 cm below surface) ground temperatures for the 15 calibration sites, b) deep (35-60 cm below surface) ground temperatures for 9 calibration site, c) thaw layer depth at 11 calibration sites where measurement was possible, and from other research (Grinter et al., (2021) ("x"), Calmels et al., 2018 (triangle); and Lacelle et al., 2009 (crosshairs)), and d) c) thaw layer depths shown in c) without the circled outliers. Coefficient of determination (R^2), root-mean-square error (RMSE) and mean absolute difference (MD) are shown.

2009) (**Fig. 4.6c**). At these sites, MD between modeled and measured thaw layer depths is 0.5 m, with a RMSE of 1.4 m. The error is driven up by our monitoring site 3 and Calmels et al. (2018) site DH103, where the thaw layer depths were greatly overestimated. When these sites are excluded, the MD and RMSE are reduced to 0.14 m and 0.17 m, respectively. Site 3 is located in the boreal forest, and all other thaw layer measurements taken in the boreal forest exceed 1 m

(**Table 4.1**), which indicates this measurement could be an error. This is also supported by the elevated ground temperatures measured at the site (**Fig. 4.7**). Site DH103 has a thick organic layer, is located in ice-wedge polygons and has a high excess ice content ($\bar{x}$=42%) (Calmels et al., 2018), details that were not represented in the model for the landcover type class under which this site falls (Shrubland tundra on bedrock), which could explain the large difference between measured and modeled thaw layer depths.

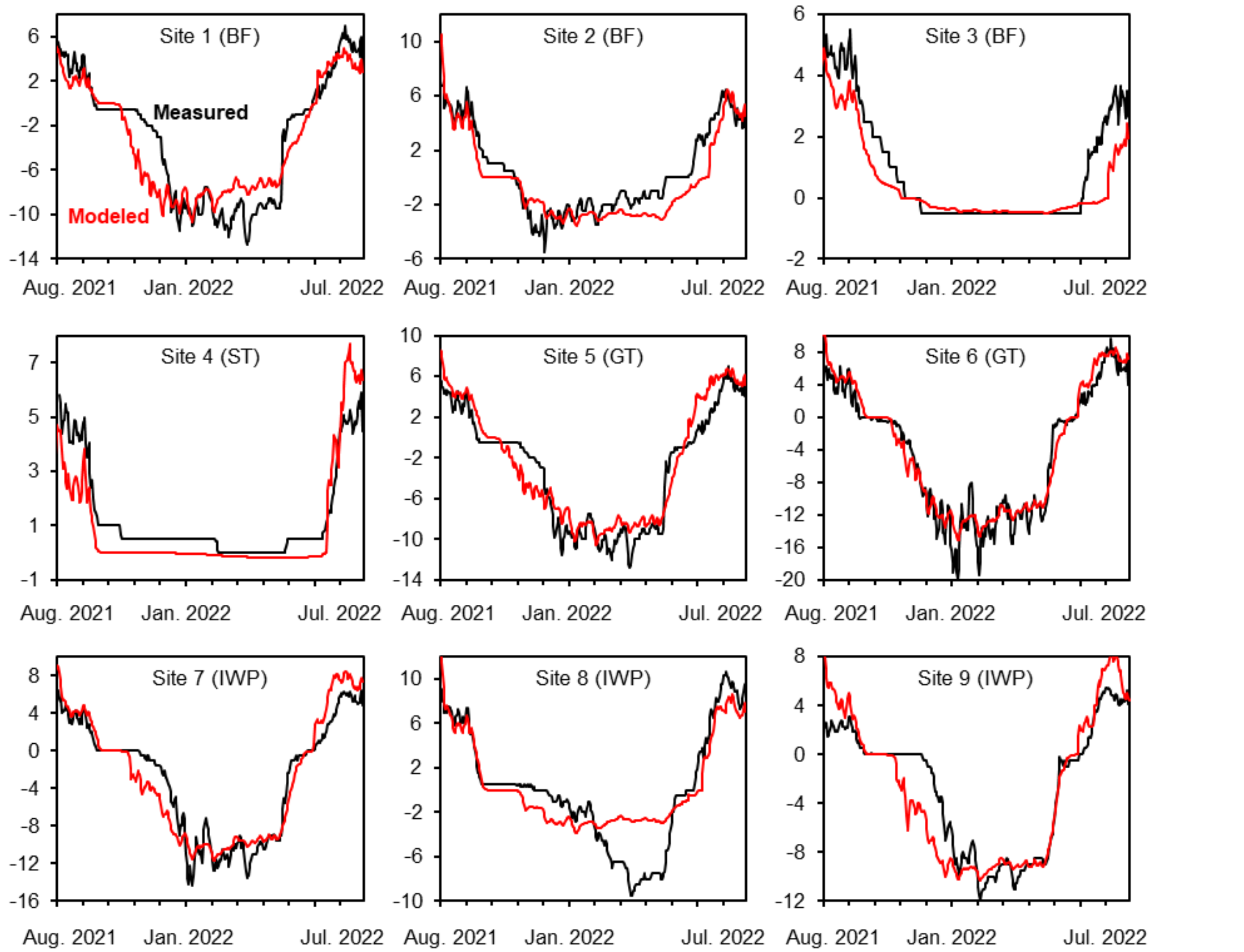

Figure 4.7 Comparison of modeled (red) and measured (black) ground temperatures at 15 cm below the surface for the 15 calibration sites. BF; Boreal Forest, ST; Shrubland tundra, GT: Grassland tundra, IWP; Ice-wedge polygons. A detailed description of each site is shown in Table 4.1.

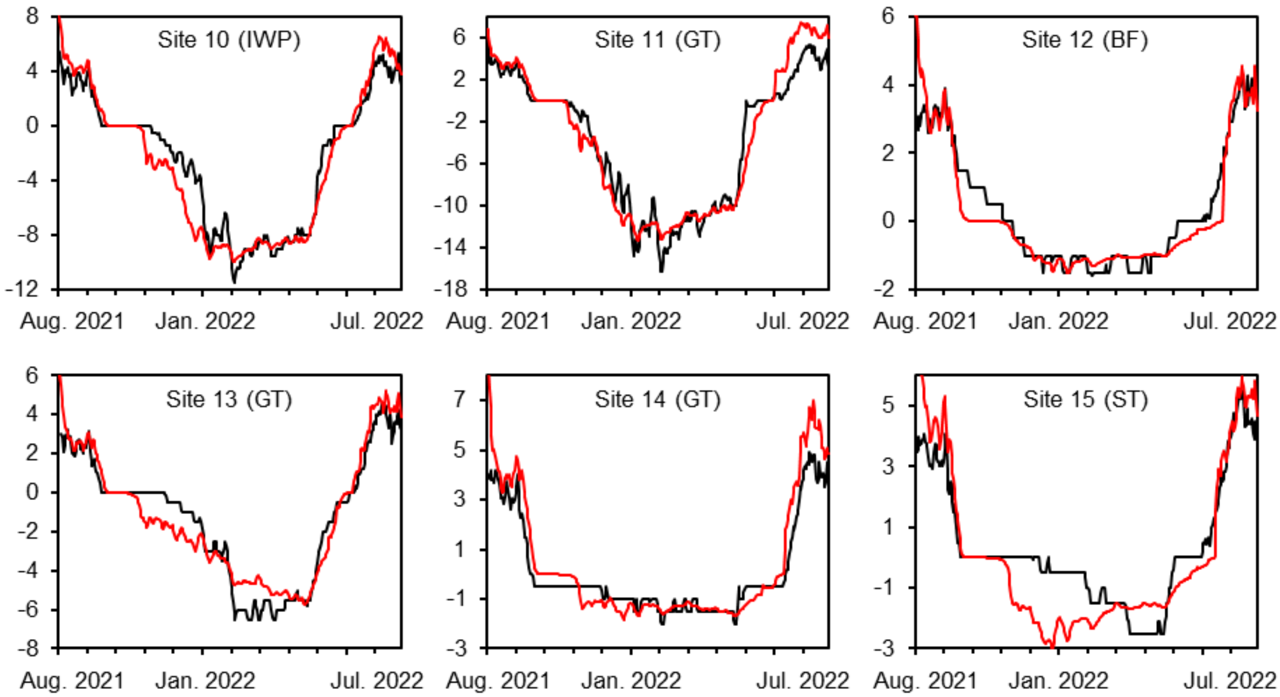

Figure 4.7 Continued

4.4.2. Modeled 2011-2020 permafrost conditions and thermal regime

The NEST model predicts that permafrost underlies the entire study area for the 2010 decade (2011-2020), with the exclusion of large waterbodies. The depth to the base of permafrost is predicted to range between 0.2 and 188.8 m, averaging 113.8 ± 49.6 m for the 2011-2020 decade (**Fig. 4.8a**). Depths to permafrost base range between 120 and 170 m in the majority of the study area (53.2%), and between 0.2 and 40 m in 18.8% of the region. No measurements exist on the thickness of permafrost within the study area. The NEST modeled average depth to permafrost base for the 2011-2020 decade is in agreement with estimations from Dawson City (Smith et al., 2004) and Red Creek borehole (Lacelle et al., 2009). Additionally, modeled permafrost distribution is validated based on the presence of permafrost-related features. The normalized frequency distribution shows that the most widespread depth to permafrost base (120-170 m) is preferentially found within barren areas, grassland tundra, anthropogenic areas, and grassland-lichen-moss tundra, and bedrock and colluvium. The second most widespread permafrost depth (0.2-40 m) is preferentially associated with shrubland tundra, and morainal and

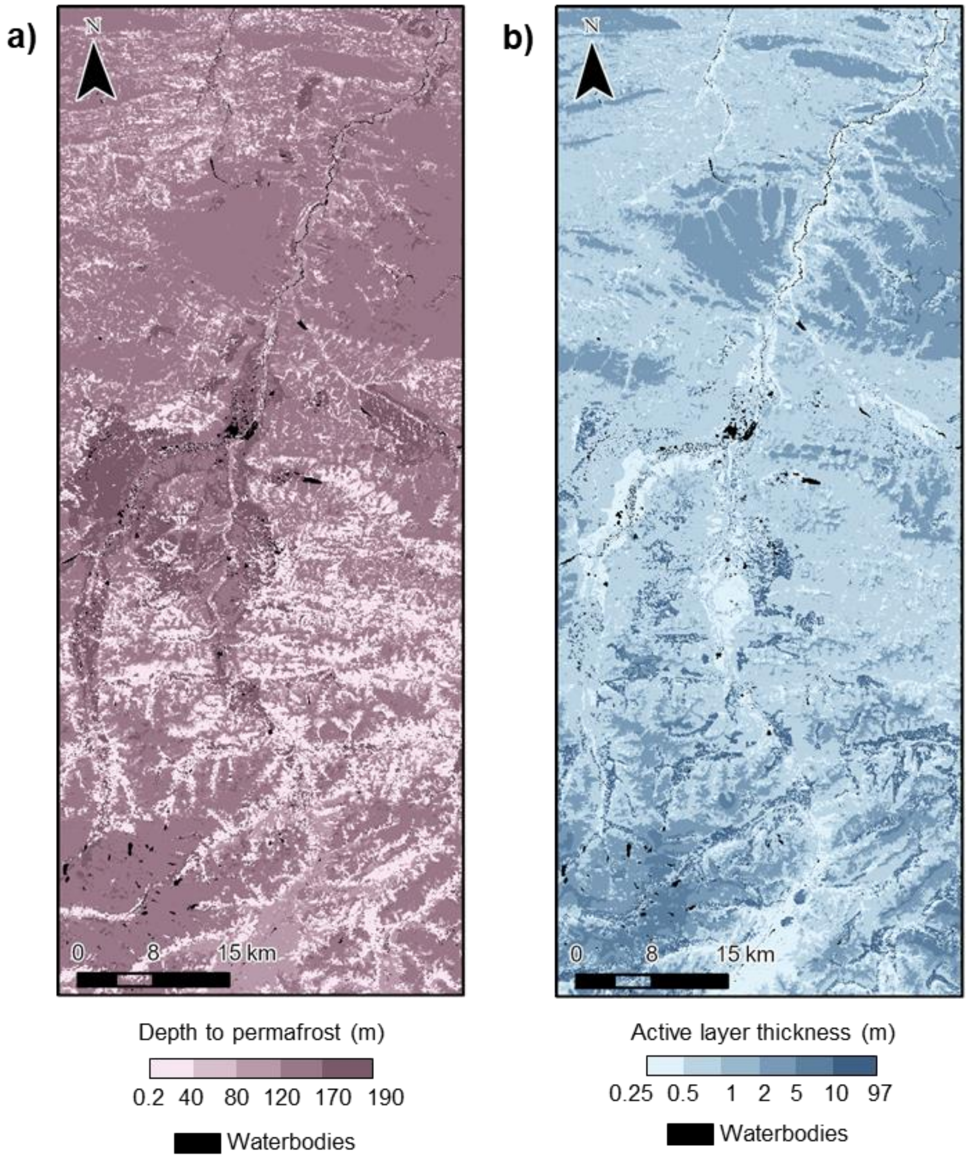

Figure 4.8 NEST-modeled a) average depth to permafrost base and b) average active layer thickness in the 2010s (2011-2020)

alluvial deposits. Shallower permafrost depths are associated with medium-to-large LAI values (1.28-5.77), and deeper permafrost (120 to 188.9 m) with small-to-medium LAI values (0.01-1.43). No permafrost thickness measurements exist in our study area, but a study in southern Yukon revealed that bedrock summits is >50 m thick (Lewkowicz et al., 2012).

For the 2011-2020 decade, modeled MAST range between −3.8 and 2°C ($\bar{x} = -1 \pm 1.2$°C), MANST range between −4.4 and 1.3°C ($\bar{x} = -1.6 \pm 1.2$°C), and MADT range between −5.5 and 0.6°C ($\bar{x} = -2.4 \pm 1.3$°C) for the entire study area. Surface and near-surface temperatures are warmest in shrubland and shrubland-lichen-moss tundra, with the majority being >0°C. Coldest surface temperatures are found in barren areas, grassland tundra, wetlands, and grassland-lichen-moss tundra. Sites located along the Dempster Highway where signs of permafrost degradation had been observed were monitored in 2016-2017, and results showed ground temperatures ranging between −3 and 0°C, with a mean of −1.8°C at depths between 2 and 3 m (Calmels et al., 2018). Our results are within a similar range, although they indicate slightly colder permafrost at depth, which is most likely related to the fact that the types of landcovers covered by our results are more varied.

4.4.3. Modeled 2011-2020 active layer thickness

The NEST modeled active layer thickness (ALT) for the 2010s range between 0.25 and 97 m, with an average of 2.45 ± 7 m (**Fig. 4.8b**). About 54% of the study area has an ALT between 0.5 and 1 m, ca. 20% is between 2 and 5 m, and ca. 12% is between 0.25 and 0.5 m. The normalized relative frequency distribution of ALTs for the 2010s reveals that thick ALTs (2-5 m) develop preferentially within barren and anthropogenic areas over colluvium. Intermediate ALTs (0.5-1 m) preferentially develop within grassland, grassland-lichen-moss and shrubland tundra, and within alluvium and colluvium. The shallowest ALTs (0.25-0.5 m) are found across the study area and they develop preferentially in organic, glaciofluvial and alluvial deposits, and within wetlands, boreal forests, and IW polygons zones. Furthermore, a relationship exists between LAI and all ALTs whereby the shallowest ALTs are associated with medium-to-large LAI values (1.44-5.77), the slightly thicker ALTs are associated with medium LAIs (1.07-1.74), and thicker ALTs are associated with small LAI values (0.01-1.06), except when we reach the thickest ALTs (>10 m) which are associated with medium LAIs (1.25-1.58). Very little data on ALT exists in the study area, except for those used to validate the model (Grinter et al., 2019; Calmels et al., 2018; Lacelle et al., 2009), which are all located along the Dempster Highway. Permafrost in mountain areas varies spatially because of the variety of landcover and materials in which they occur and their effects on the ground thermal regime (Gruber and Haeberli, 2008). A study of mountain permafrost in southern Yukon reported ALTs >5 m on bedrock summits (Lewkowicz et al., 2012).

4.4.4. Predicted changes in permafrost distribution and conditions

While modeled ALTs and permafrost depth show that permafrost persisted in the entire study area until the 2010s, predicted ALTs and permafrost depth show permafrost loss under both tested climate scenarios.

The NEST model predicts that 22% of the study area will have lost permafrost by the 2090s under RCP4.5 (**Fig. 4.9a**), and 29% under RCP8.5. Under RCP4.5, depths to permafrost base are predicted to decrease on average by 11.4 ± 5% between the 2010s and the 2090s. About 45% of the study area is predicted to experience a permafrost base depth decrease of 3-12%, and 25% a decrease of 12-25% (**Fig. 4.9a**). ALTs are predicted to experience a 40-70% increase in 22% of the study area, and a 150-300% increase in 17% of the study area (**Fig. 4.9b**). These numbers are in the range of those reported following disturbances such as wildfires; A forest-tundra fire near Inuvik (Northwest Territories, Canada) caused for ALT increase up to 300% (Mackay, 1995). ALT increases reaching 200% have also been measured in the European Alps between 2000 and 2019 and have been related to local thermal conditions such as advective heat transport and radiation balance (Etzelmüller et al., 2020). Under RCP 8.5, depths to permafrost base are predicted to decrease on average by 12.3 ± 6%, with about 36% of the study area predicted to experience a permafrost base depth decrease of 3.4-10%, and 28% a decrease of 10-20%. The most widespread ALT increases are larger than predicted under RCP4.5; 35% of the study area is predicted to experience an ALT increase between 1700 and 17528%, and 23% between 600 and 1700%.

Based on the normalized frequency distribution, permafrost losses occurred preferentially within morainal and alluvial deposits and in shrubland and shrubland-lichen-moss tundra under both RCP4.5 and RCP8.5, with the addition of boreal forest under RCP8.5. The most widespread permafrost depth decreases predicted under both climate scenarios (3-12%) are preferentially associated with organic, glaciofluvial and morainal deposits, and a variety of vegetation cover types (i.e., wetlands, grassland tundra, grassland-lichen-moss tundra, anthropogenic and barren areas) that exclude taller vegetations (i.e., boreal forest and shrubland). Under RCP4.5, the slightly larger decrease in depth to permafrost base (12-25%) are associated with grassland tundra and boreal forest, and bedrock, active floodplain, colluvium, alluvium. Under RCP8.5, these larger increases (10-20%) are associated with grassland tundra within bedrock, alluvium and colluvium.

Under RCP4.5, the most widespread ALT increases (40-70%) are preferentially associated with barren and boreal forest areas within organic, alluvial, and glaciofluvial deposits while the larger widespread ALT increases (150-300%) are preferentially associated with grassland tundra and barren areas within colluvial and morainal deposits. The larger ALT increases predicted under RCP8.5 (600-17528%) are preferentially associated with barren lands, anthropogenic areas, and grassland tundra within bedrock, colluvium, and active floodplains.

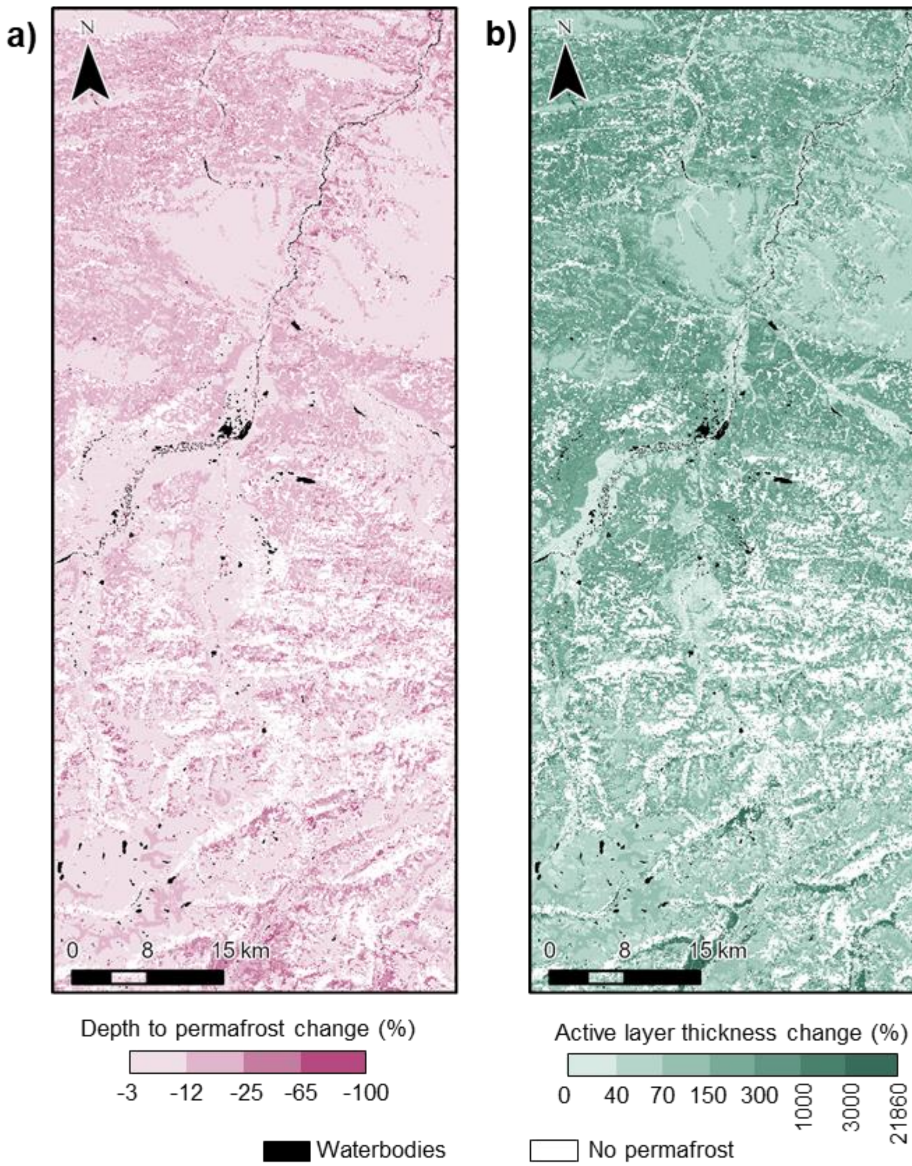

Figure 4.9 NEST-modeled average a) active layer thickness change and b) depth to permafrost base changes between the 2010s (2011-2020) and 2090s (2091-2100) under RCP4.5.

Under both RCP4.5 and RCP8.5, the smaller permafrost base depth decreases and ALT increases are associated with smaller LAI values, while larger permafrost depth decrease, larger ALT increases and permafrost loss are associated with larger LAI values.

Overall, modeled average ALT and depth to permafrost base for the entire study area show a gradually decreasing permafrost depth starting at the end of the 1990s, and a more pronounced decrease starting around 2025 and accompanied by an ALT increase (**Fig. 4.10**). While permafrost depth decrease is more gradual, ALT increase is less stable and shows some years of permafrost aggradation. Under RCP4.5, ALT stabilizes around 2095, while permafrost depth continue to rise. Under RCP8.5, ALT increases more dramatically and permafrost base depth decreases a little more than that of RCP4.5 until 2100. The overall trend reveals that permafrost degradation comes from both warming from below and active layer thickness increase.

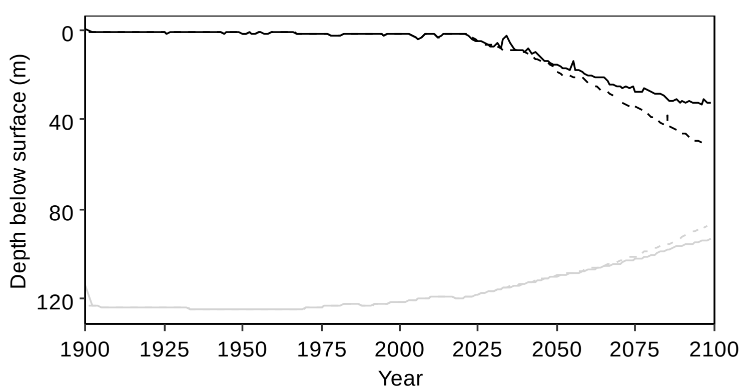

Figure 4.10 NEST-modeled average active layer thickness (black) and depth to permafrost base (gray) for RCP4.5 (solid) and RCP8.5 (dashed) from 1901 to 2100 for the entire study area.

4.5. Discussion

4.5.1. Permafrost distribution, conditions and change, and determinant landscape factors

The NEST model indicates that permafrost has persisted through the 20th century and beginning of the 21st century and is currently present throughout the study area. Modeled mean permafrost depth (113.8 ± 49.6 m), mean ALT (2.45 ± 7 m), mean surface temperature (−1 ± 1.2°C), mean near-surface (−1.6 ± 1.2°C) and deep (−2.4 ± 1.3°C) temperature are in accordance with other local and regional measurements.

The normalized frequency distributions of ALT, permafrost depth and their changes between the 2010s and 2090s compared to surficial deposits, vegetation cover and LAI values reveals the importance of these factors in determining permafrost distribution, conditions and their sensitivity to climate changes. Particularly, permafrost losses are associated with morainal and alluvial deposits, especially when associated with shrubland tundra and larger LAI values. Both of these deposits also have shallow depth to permafrost base. While morainal deposits are very shallow (100 m) and have thinner organic layers (5-15 cm), making them more directly related to the thermal conditions of both the underlying bedrock and the surface, alluvium is deep (500 m) with a thick top organic layer (20-30 cm), which contributes to this type of deposit being less affected by heat penetration during summer. However, shrubland tundra is related to snowdrift trapping, which insulates the ground from cold winter air temperatures, hindering heat loss, and can contribute to permafrost degradation. Areas of shrubland tundra in the study area are also associated with the warmest modeled permafrost temperatures. These combined factors make shrubland tundra in alluvial and morainal deposits especially sensitive to climate changes.

Grassland tundra and barren lands underlain by colluvium and bedrock are associated with thicker ALTs, deep and cold permafrost, and small decreases in depth to permafrost base until 2100 (10-25%). However, they are associated with large ALTs increases (150-17528%), most likely because they do not contribute to blocking incoming solar radiation.

Small-to-medium LAI wetland, grassland tundra, grassland-lichen-moss tundra, anthropogenic and barren lands within organic deposits are associated with small ALT increases and small permafrost base depth decrease. This illustrates how organic-rich surface layers, which tend to be poorly drained and therefore have higher thermal conductivities in winter when frozen then during summer when unfrozen (Burn and Smith, 1988; Romanovsky and Osterkamp, 1995), hinders heat penetration during summer and favors heat loss during winter (Jorgenson et al., 2010). This effect is enhanced by the low vegetation which contributes to more rapid heat loss by allowing snow to drift away. Active floodplains are also associated with small ALT increases and small permafrost base depth decrease. However, the NEST model is one-dimensional, so lateral heat fluxes from adjacent streams and rivers, which would most likely change the active floodplains thermal regime, are not represented.

Overall, the modeling exercise and results show the importance of a) vegetation height and LAI which determine the degree of exposure of the ground to solar radiation and the amount of heat loss during winter through snow drifting or trapping, b) surface organic layer which controls heat energy exchanges between the air, the surface and deeper ground, and c) the thickness of surficial deposits which influences the thickness of permafrost.

4.5.2. Landcover types and feedbacks

Modeled future changes show largest ALT increases and depth to permafrost base decreases associated with different landcover types, indicating that whether permafrost loss will occur and how the thermal regime will be affected is dependent on the type of landcover. This illustrates the importance of the surface and thermal offsets and how they relate to the geo-ecological characteristics of each landcover types (Jorgenson et al., 2010). For the most common landcover types in the study area, modeled surface offset (MAST − MAAT) range from 2°C in grassland tundra to 5.9°C in shrubland tundra, both in morainal deposits (**Fig. 4.11**). For grassland tundra, the surface offset is larger in colluvium and alluvium, and for shrubland tundra the surface offset is smaller in colluvium. Barren colluvium has the second-smallest surface offset of 3°C. The large surface offsets associated with shrubland tundra illustrate once again how this type of landcover contributes to warming the ground, especially as an effect of snow trapping, whereas in barren lands, grassland tundra and the boreal forest, snow is either drifted away or intercepted by

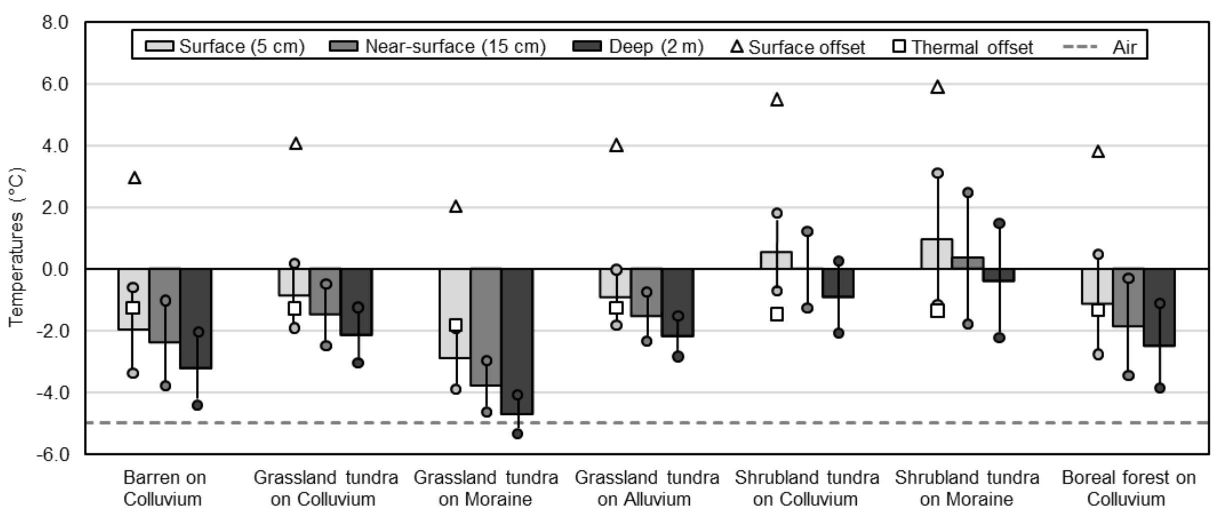

Figure 4.11 NEST-modeled surface ground temperature (MAST), near-surface ground temperature (MANST), and deep ground temperature (MADT) for seven common landcover types in and near the Tombstone Territorial Park for the 2011-2020 decade. Modeled surface offset (MAST − MAAT) and thermal offset (MADT – MAST) are shown for each landcover type. Mean annual air temperature is also shown for the 2011-2020 decade.

vegetation, which allows for increased heat loss during winter. Modeled thermal offset (MADT – MAST) ranged from −1.2°C in barren colluvium to −1.8°C in grassland tundra on morainal deposits. Again, organic surface layers tend to be poorly drained and therefore have higher thermal conductivities in winter when frozen then during summer when unfrozen, which leads to larger thermal offset (Burn and Smith, 1988; Romanovsky and Osterkamp, 1995). On the opposite, barren colluvium is generally well drained and therefore experiences less changes in thermal conductivities between summer and winter, which result in smaller thermal offsets (Jorgenson et al., 2010).

Permafrost in the study area most likely went from being climate-driven in the Pleistocene (i.e., permafrost formation is due to cold climate conditions), to ecosystem-driven in the mid-Holocene (i.e., permafrost exists because of the combination of climate and ecological conditions), and it might become ecosystem-protected in the 21st century (i.e., permafrost persists in certain local ecological conditions, but cannot redevelop after degradation) (French et al., 2017). The vast majority of the study has remained unglaciated since at least the mid-Pleistocene, and while the early Holocene warm interval most likely melted large amounts of near-surface ground ice (Grinter et al., 2019), the cooler climate and possible moisture increase that followed in the mid-Holocene, caused for the open forest of white spruce to be replaced by black spruce forest and green alder (Cwynar and Spear, 1995; Dyke, 2005) and for permafrost to aggrade (Ritchie, 1984). As the cooling trend continued, the forest cover reached its current position in the southern part of area and gave way to tundra in the central and northern parts (Cwynar and Spear, 1995). More recently, the widespread presence of grassland tundra and associated thick surface organic layer protects permafrost from heat penetration in summer and allows for heat loss in winter. While barren lands have been associated with important permafrost degradation because of their lack of protective vegetation and organic layer (Fraser et al., 2018; Ward Jones et al., 2019), here we find that the fact that barren lands are mostly associated with colluvium, and are therefore well drained, and have deep permafrost, contributes to their relatively smaller thermal offsets, despite having thick ALTs. Modeling of future changes indicates large ALT increases in these areas, which could mean that these areas will no longer be able to recover under warmer conditions after degradation, making them ecosystem-protected permafrost.

There are a few notable implications of the modeled permafrost conditions and changes within the study area. Barren colluvium are associated with mountain ridges and slopes. Their vulnerability to active layer degradation therefore poses a risk of potential slope instability (Gruber and Haeberli, 2007; Harris et al., 2008), which could mean the increase of magnitude and density of mass movement such as slope failures and rock avalanches (e.g., Geertsema et al., 2006; Dramis et al., 1995; Gruber et al., 2004). Moreover, the NEST model is one-dimensional and does not account for lateral heat fluxes, which greatly impacts ground thermal conditions in mountainous topography (Noetzli et al., 2007). The degree of fracturing in bedrock also plays an important role whereby water percolating in fractures increases energy transfers, resulting in thicker ALTs and a potential for more important degradation upon warming (Gruber and Haeberli, 2007). These two parameters were not taken into account in the modelling and mapping, meaning that degradation could be underestimated in mountains exposing bedrock or overlain by thin colluvium.

Additionally, shrubland tundra and larger-LAI values areas are mostly associated with river valleys, meaning that their sensitivity to permafrost degradation could have important impacts on the aquatic ecosystem. Permafrost thaw remobilizes soil organic matter and minerals which can then enter lakes, streams and rivers, greatly impacting their physical and optical properties (Vonk et al., 2015). Finally, in this study, changes in landcover types were not considered. But the vulnerability of shrubland tundra to permafrost degradation indicates that an increase in shrub cover could lead to important permafrost thaw because of their effect on atmosphere-surface heat energy exchanges (Zhang et al., 2012). Landcover changes associated with coniferous shrubs expansion has been detected in the study area for the 1986-2021 period (Frappier et al., in press), meaning that an increase in the extent of permafrost degradation associated with shrubland tundra could be observed.

4.5.3. Application of the NEST model in a mountainous region with polygonal terrain

Contrary to that of the European Alps, the relationship between permafrost distribution and elevation in the Yukon is non-linear and permafrost is found both above and below the treeline (Bonnaventure et al., 2012), meaning that permafrost distribution cannot efficiently be represented solely by elevation and solar radiation parameters (e.g., Gruber and Hoelzle, 2001). The incorporation of vegetation in modelling permafrost distribution in the Yukon has been proven useful, especially when combined with elevation data (Kremer et al., 2011). In our study area specifically, there is a strong relationship between elevation, landcover types and LAI (**Fig. 4.2 and 4.4**). Our modeled ALTs and permafrost depths compared well with other local and regional observations, indicating that modeling and mapping permafrost in a mountains setting with the NEST model, using high spatial resolution landcover and LAI data, is practical.

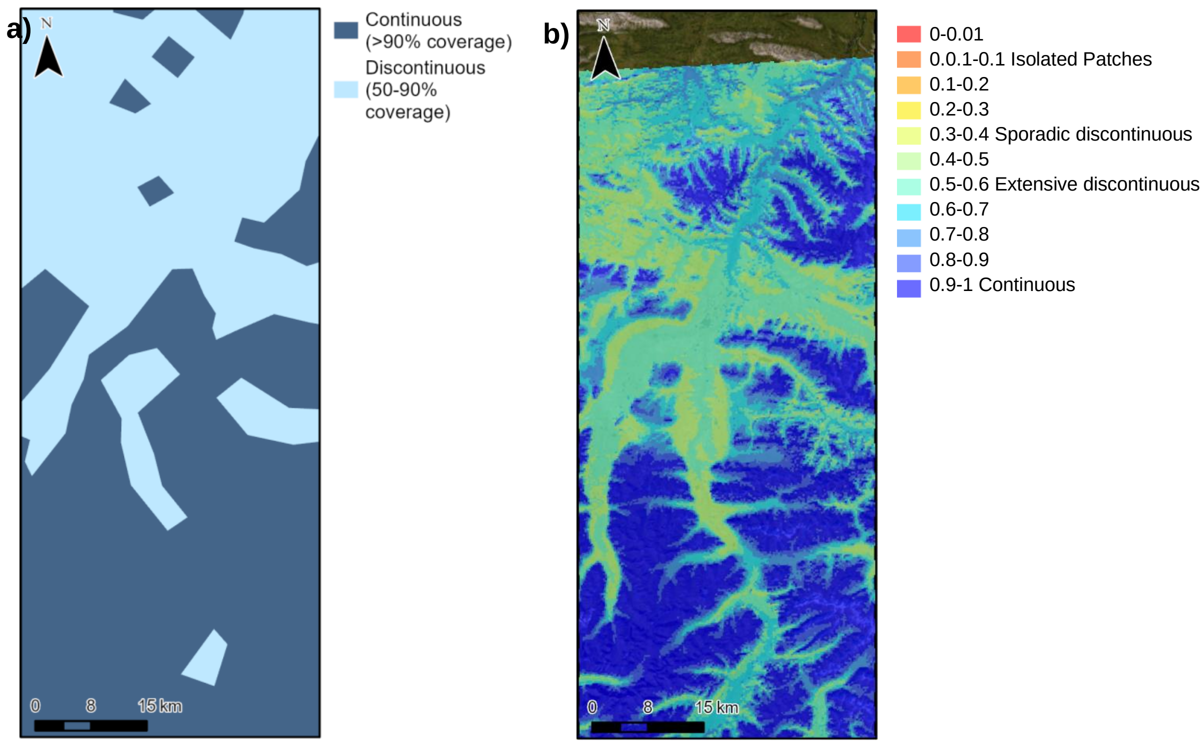

Figure 4.12 a) Permafrost distribution map based on TTOP modelling for 2000-2016 (Obu et al., 2019), and b) permafrost probability map based on elevation, potential incoming solar radiation and surface lapse rates (Bonnaventure et al., 2012).

Existing permafrost distribution models covering our study area show continuous permafrost in the higher elevations and extensive discontinuous to sporadic permafrost in valley bottoms and plateaus, with a higher probability of permafrost in the valleys to the north and south of the study area, and a lower probability of permafrost in the Blackstone and East Blackstone river and Taiga valleys (**Fig. 4.12**) (Obu et al., 2019; Bonnaventure et al., 2012). The Obu et al. (2019) permafrost distribution map (**Fig. 4.12a**) assumes that permafrost is in equilibrium with the 2000-2016 TTOP measurements and does not take into account the history of ground thermal conditions and changes of ground temperature under a warming climate. This can reduce the model accuracy under transient conditions, especially where permafrost is rapidly warming or cooling, where ground temperatures is close to 0°C, where the soil moisture content is high, and under thick relict permafrost. The Bonnaventure et al. (2012) permafrost probability model (**Fig. 12b**) is a combination of seven local empirical-statistical models, and it integrates elevation, potential incoming solar radiation and surface lapse rates to depict the relationship between permafrost distribution and elevation. While the results of our study show thick permafrost in high elevations, thick permafrost is also found within the Blackstone Plateau, the Blackstone and East Blackstone river valleys, the Taiga Valley and throughout most of the northern area of the study area, and thinner permafrost is found in the valleys, especially within the southern half of the study area. The abundance of periglacial landforms, including IW polygons, in the Blackstone and East Blackstone river valleys and in the Taiga Valley, and the presence of boreal forest within the southern valleys corroborate these results. Our study therefore reveals how the NEST model can efficiently represent the effects of vegetation, surficial geology, ground conditions and topography, without specifically integrating elevation in the model.

4.6. Conclusion

In this study, the NEST model was used to model and map permafrost distribution and thermal conditions in the Ogilvie Mountains for past, current and future conditions under two climate scenarios. Results show the importance of vegetation height and LAI, surface organic layer thickness and conditions, and surficial deposits thickness, because of their impact on energy exchanges between the atmosphere, the surface and deeper ground. Our study indicates that the stability of slopes, the conditions of aquatic systems and the effects of shrubification should be monitored in the study area as they may be greatly impacted by permafrost changes.

4.7. Acknowledgments

This work was supported by Natural Resources Canada as a part of the Government of Canada's initiative for monitoring and assessing regional cumulative effects, les Fonds de recherche du Québec – Nature et Technologies (FRQNT), and Natural Sciences and Engineering Research Council of Canada (NSERC) Discovery Grants with logistical support provided by NSERC Northern Supplement, and the Northern Scientific Training Program. We thank M. Landry and N. Comerford for valuable field assistance. Fieldwork was performed under the Yukon

Scientists and Explorers Act Licence 21-43S&E and 22-67S&E, Yukon Park Permit No. 20-RE-TP-03 and 22-RE-TP-08 and with approval from the Tr'ondek Hwech'in government.

4.8. Supporting information

Data is available in supplementary material, included in appendices.

Table S4.1 NEST model input parameters for each unique landcover type class (combining landcover, surficial deposits and leaf area index) in and near the Tombstone Territorial Park, Central Yukon

4.9. References

Arctic Monitoring and Assessment Programme (AMAP). (2017). *Snow, Water, Ice and Permafrost in the Arctic (SWIPA).* www.amap.no

Beck, H. E., Zimmermann, N. E., McVicar, T. R., Vergopolan, N., Berg, A., & Wood, E. F. (2018). Present and future Köppen-Geiger climate classification maps at 1-km resolution. *Scientific Data*, *5*(1), 180214. https://doi.org/10.1038/sdata.2018.214

Bonnaventure, P. P., Lewkowicz, A. G., Kremer, M., & Sawada, M. C. (2012). A Permafrost Probability Model for the Southern Yukon and Northern British Columbia, Canada. *Permafrost and Periglacial Processes*, *23*(1), 52–68. https://doi.org/10.1002/ppp.1733

Brown, J., Ferrians, O. J., Heginbottom, J. A., and Melnikov, E. S. (1997). *Circum-Arctic map of permafrost and ground-ice conditions*, Circum-Pacific Map Series CP-45, Scale 1 V 10;000; 000, U.S. Geological Survey, Reston, VA.

Burn, C. R., & S Smith, C. A. (1988). Observations of the "Thermal Offset" in Near-Surface Mean Annual Ground Temperatures at Several Sites near Mayo, Yukon Territory, Canada. *Arctic*, *41*(2), 99–104.

Calmels, F., Roy, L. P., Grandmont, K., & Pugh, R. (2018). Summary of climate-and geohazard-related vulnerabilities for the Dempster Highway corridor.

Cwynar, L. C., & Spear, R. W. (1995). Paleovegetation and Paleoclimatic Changes in the Yukon at 6 ka BP. *Géographie Physique et Quaternaire*, *49*(1), 29–35. https://doi.org/10.7202/033027ar

Duk-Rodkin, A., 1996. Surficial geology, Dawson, Yukon Territory, 1:250,000.

Dramis, F., Govi, M., Guglielmin, M., & Mortara, G. (1995). Mountain permafrost and slope instability in the Italian Alps: The Val Pola Landslide. *Permafrost and Periglacial Processes*, *6*(1), 73–81. https://doi.org/10.1002/PPP.3430060108

Dyke, A. S. (2005). Late quaternary vegetation history of northern North America based on pollen, macrofossil and faunal remains. *Geographie Physique et Quaternaire*, *59*(2–3), 211–262.

Ensom, T., Makarieva, O., Morse, P., Kane, D., Alekseev, V., & Marsh, P. (2020). The distribution and dynamics of aufeis in permafrost regions. *Permafrost and Periglacial Processes, 31*(3), 383–395. https://doi.org/10.1002/ppp.2051

Environment and Climate Change Canada (2022). *Canadian Climate Station Data*. http://climate.weather.gc.ca.

Etzelmüller, B., Guglielmin, M., Hauck, C., Hilbich, C., Hoelzle, M., Isaksen, K., Noetzli, J., Oliva, M., & Ramos, M. (2020). Twenty years of European mountain permafrost dynamics-the PACE legacy. Environmental Research Letters, 15(10), 104070–. https://doi.org/10.1088/1748-9326/abae9d

Fernandes, R. A., & Sun, L. (2021). *LEAF-Toolbox-Canada Repository*. Government of Canada. https://github.com/rfernand387/LEAF-Toolbox-Canada

Frappier, R., & Lacelle, D. (2021). Distribution, morphometry, and ice content of ice-wedge polygons in Tombstone Territorial Park, central Yukon, Canada. *Permafrost and Periglacial Processes*, *32*(4), 587–600. https://doi.org/10.1002/ppp.2123

Frappier, R., Lacelle, D. and Fraser, R.H. (in press). Landscape Changes in the Tombstone Territorial Park region (central Yukon, Canada) from Multi-Level Remote Sensing Analysis [Manuscript accepted for publication].

Fraser, R., Kokelj, S., Lantz, T., McFarlane-Winchester, M., Olthof, I., & Lacelle, D. (2018). Climate Sensitivity of High Arctic Permafrost Terrain Demonstrated by Widespread Ice-Wedge Thermokarst on Banks Island. *Remote Sensing, 10*(6), 954. https://doi.org/10.3390/rs10060954

French HM. (2017). *The Periglacial Environment: Fourth Edition*.; Hoboken, NJ: John Wiley and Sons.

Geertsema, M., Clague, J. J., Schwab, J. W., & Evans, S. G. (2005). *An overview of recent large catastrophic landslides in northern British Columbia, Canada.* https://doi.org/10.1016/j.enggeo.2005.06.028

Grinter, M., Lacelle, D., Baranova, N., Murseli, S., Clark, I.D., 2019. Late Pleistocene and Holocene ice-wedge activity on the Blackstone Plateau, central Yukon, Canada. Quaternary Research (United States) 91, 179–193. https://doi.org/10.1017/qua.2018.65

Gruber, S., & Haeberli, W. (2007). Permafrost in steep bedrock slopes and its temperature-related destabilization following climate change. *Journal of Geophysical Research, 112*(F2), F02S18. https://doi.org/10.1029/2006JF000547

Gruber, S., & Haeberli, W. (2008). Mountain Permafrost. In Permafrost Soils (pp. 33–44). Springer Berlin Heidelberg. https://doi.org/10.1007/978-3-540-69371-0_3

Gruber, S., & Hoelzle, M. (2001). Statistical Modelling of Mountain Permafrost Distribution: Local Calibration and Incorporation of Remotely Sensed Data. *Permafrost and Periglacial Processes, 12*, 69–77. https://doi.org/10.1002/ppp

Gruber, S., Hoelzle, M., & Haeberli, W. (2004). Permafrost thaw and destabilization of Alpine rock walls in the hot summer of 2003. *Geophysical Research Letters, 31*(13). https://doi.org/10.1029/2004GL020051

Harris, C., Smith, J. S., Davies, M. C. R., & Rea, B. (2008). An investigation of periglacial slope stability in relation to soil properties based on physical modelling in the geotechnical centrifuge. *Geomorphology, 93*(3–4), 437–459. https://doi.org/10.1016/j.geomorph.2007.03.009

Heginbottom, J. A., Dubreuil, M. A., & Haker, P. T. (1995*). Canada permafrost*, 1:7 500 000 scale. The National Atlas of Canada, 5th Edition. Sheet MCR 4177, National Resources Canada: Ottawa.

Hu, X., & Pollard, W. H. (1997). The hydrologic analysis and modelling of river icing growth, North Fork Pass, Yukon Territory, Canada. *Permafrost and Periglacial Processes, 8*(3), 279–294. https://doi.org/10.1002/(sici)1099-1530(199709)8:3<279::aid-ppp260>3.0.co;2-7

Jorgenson, M. T., Romanovsky, V., Harden, J., Shur, Y., O'Donnell, J., Schuur, E. a G., Kanevskiy, M., & Marchenko, S. (2010). Resilience and vulnerability of permafrost to climate change. *Canadian Journal of Forest Research, 40*, 1219–1236. https://doi.org/10.1139/X

Lacelle, D., Lauriol, B., Clark, I. D., Cardyn, R., & Zdanowicz, C. (2007). Nature and origin of a Pleistocene-age massive ground-ice body exposed in the Chapman Lake moraine complex, central Yukon Territory, Canada. *Quaternary Research, 68*(2), 249–260. https://doi.org/10.1016/j.yqres.2007.05.002

Lacelle, D., St-Jean, M., Lauriol, B., Clark, I. D., Lewkowicz, A., Froese, D. G., Kuehn, S. C., & Zazula, G. (2009). Burial and preservation of a 30,000 year old perennial snowbank in Red Creek valley, Ogilvie Mountains, central Yukon, Canada. *Quaternary Science Reviews, 28*(27–28), 3401–3413. https://doi.org/10.1016/j.quascirev.2009.09.013

Latifovic, R., Pouliot, D., & Olthof, I. (2017). Circa 2010 Land Cover of Canada: Local Optimization Methodology and Product Development. *Remote Sensing, 9*(11), 1098. https://doi.org/10.3390/rs9111098

Lewkowicz, A.G., Bonnaventure, P.P., Smith, S.L. and Kuntz, Z., (2012). Spatial and thermal characteristics of mountain permafrost, northwest Canada. Geografiska Annaler: Series A, Physical Geography, 94(2),195-213. doi:10.1111/j.1468-0459.2012.00462.x

Mackay, J. R. (1995). Active layer changes (1968 to 1993) following the forest-tundra fire near Inuvik, N.W.T., Canada. Arctic and Alpine Research, 27(4), 323–336. https://doi.org/10.2307/1552025

Mckenney, D. W., Hutchinson, M. F., Papadopol, P., Lawrence, K., Pedlar, J., Campbell, K., Milewska, E., Hopkinson, R. F., Price, D., & Owen, T. (2011). Customized spatial Climate models for North ameriCa. *Bulleting of American Meteorological Society, 92*(12), 1611–1622. https://doi.org/10.1175/Bams-d-10-3132.1

Noetzli, J., Gruber, S., Kohl, T., Salzmann, N., & Haeberli, W. (2007). Three-dimensional distribution and evolution of permafrost temperatures in idealized high-mountain topography. *Journal of Geophysical Research, 112*(F2), F02S13. https://doi.org/10.1029/2006JF000545

O'Neill, H.B., Wolfe, S.A., and Duchesne, C. (2019). New ground ice maps for Canada using a paleogeographic modelling approach. *The Cryosphere, 13*(3), 753–773. https://doi.org/10.5194/tc-13-753-2019

Ou, C., LaRocque, A., Leblon, B., Zhang, Y., Webster, K., & McLaughlin, J. (2016). Modelling and mapping permafrost at high spatial resolution using Landsat and Radarsat-2 images in Northern Ontario, Canada: Part 2 – regional mapping. *International Journal of Remote Sensing, 37*(12), 2751–2779. https://doi.org/10.1080/01431161.2016.1151574

Page, A. (2009). *A topographic and photogrammetric study of rock glaciers in the southern Yukon Territory*. University of Ottawa.

Ritchie, J. C. (1984). Past and present vegetation of the far northwest of Canada. *Journal of Ecology, 73*(3), 1074-1075. https://doi.org/10.2307/2260178

Romanovsky, V. E., & Osterkamp, T. E. (1995). Interannual variations of the thermal regime of the active layer and near-surface permafrost in northern Alaska. *Permafrost and Periglacial Processes, 6*(4), 313–335. https://doi.org/10.1002/PPP.3430060404

Shur, Y. L., & Jorgenson, M. T. (2007). Patterns of permafrost formation and degradation in relation to climate and ecosystems. *Permafrost and Periglacial Processes, 18*(1), 7–19. https://doi.org/10.1002/ppp.582

Smith, C. A. S., Meikle, J. C., & Roots, C. F. (2004). *Ecoregions of the Yukon Territory : biophysical properties of Yukon landscapes*. Agriculture and Agri-Food Canada.

Solvik, K. K., Potter, S., Erb, A. M., Roman, M., Schaaf, C., Sun, Q., Wang, Z., & Rogers, B. M. (2019). *ABoVE: MODIS-Derived Daily Mean Blue Sky Albedo for Northern North America, 2000-2017*. In ORNL DAAC.

Thomas, R.D. and Rampton, V.N. (1982). *Surficial Geology and Geomorphology, Upper Blackstone River, Yukon Territory*. Geological Survey of Canada, Preliminary Map 7-1982, scale 1:100,000.

van Everdingen, R. (2005). Multi-language glossary of permafrost and related ground-ice terms. In *National Snow and Ice Data Center/World Data Center for Glaciology*, Boulder (Vol. 1998, Issue ed 1998 revised). https://doi.org/10.2307/1551636

van Vuuren, D. P., Edmonds, J., Kainuma, M., Riahi, K., Thomson, A., Hibbard, K., Hurtt, G. C., Kram, T., Krey, V., Lamarque, J. F., Masui, T., Meinshausen, M., Nakicenovic, N., Smith, S. J., & Rose, S. K. (2011). The representative concentration pathways: An overview. *Climatic Change*, *109*(1), 5–31. https://doi.org/10.1007/S10584-011-0148-Z/TABLES/4

Vonk, J. E., Tank, S. E., Mann, P. J., Spencer, R. G. M., Treat, C. C., Striegl, R. G., Abbott, B. W., & Wickland, K. P. (2015). Biodegradability of dissolved organic carbon in permafrost soils and aquatic systems: A meta-analysis. *Biogeosciences, 12*(23), 6915–6930. https://doi.org/10.5194/BG-12-6915-2015

Ward Jones, M. K., Pollard, W. H., & Jones, B. M. (2019). Rapid initialization of retrogressive thaw slumps in the Canadian high Arctic and their response to climate and terrain factors. *Environmental Research Letters, 14*(5). https://doi.org/10.1088/1748-9326/ab12fd

Way, R. G., Lewkowicz, A. G., & Zhang, Y. (2018). Characteristics and fate of isolated permafrost patches in coastal Labrador, Canada. *The Cryosphere, 12*, 2667–2688. https://doi.org/10.5194/tc-12-2667-2018

Zhang, W., Witharana, C., Liljedahl, A. K., & Kanevskiy, M. (2018). Deep convolutional neural networks for automated characterization of arctic ice-wedge polygons in very high spatial resolution aerial imagery. *Remote Sensing, 10*(9). https://doi.org/10.3390/rs10091487

Zhang, Y., Chen, W., & Cihlar, J. (2003). A process-based model for quantifying the impact of climate change on permafrost thermal regimes. *Journal of Geophysical Research Atmospheres*, *108*(22). https://doi.org/10.1029/2002jd003354

Zhang, Y., Chen, W., & Riseborough, D. W. (2006). Temporal and spatial changes of permafrost in Canada since the end of the Little Ice Age. *Journal of Geophysical Research Atmospheres*, 111(22). https://doi.org/10.1029/2006JD007284

Zhang Y, Qian B, Hong G. (2020). A Long-Term, 1-km Resolution Daily Meteorological Dataset for Modeling and Mapping Permafrost in Canada. Atmosphere, 11(12):1363. https://doi.org/10.3390/atmos11121363

Zhang, Y., Sachs, T., Li, C., & Boike, J. (2012). Upscaling methane fluxes from closed chambers to eddy covariance based on a permafrost biogeochemistry integrated model. *Global Change Biology, 18*(4), 1428–1440. https://doi.org/10.1111/J.1365-2486.2011.02587.X

Zhang, Y. (2013). Spatio-temporal features of permafrost thaw projected from long-term high resolution modeling for a region in the Hudson Bay Lowlands in Canada. *Journal of Geophysical Research.-Earth Surface*, 118, 1-11. doi: 10.1002/jgrf.20045

Zhang, Y., S. A. Wolfe, P. D. Morse, I. Olthof, and R. H. Fraser (2015). Spatiotemporal impacts of wildfire and climate warming on permafrost across a subarctic region, Canada. *Journal of Geophysical Research, Earth Surface*, 120(11), 2338-2356. doi: 10.1002/2015JF003679

Zhang, Y., Qian, B., Hong, G. (2020). A long-term, 1-km resolution daily meteorological dataset for modeling and mapping permafrost in Canada, *Atmosphere, 11*(12), 1363.

CHAPTER 5: CONCLUSIONS

5.1. Summary and conclusions

Despite access along the road and signs of permafrost degradation, there have been a limited number of studies addressing permafrost and ground ice conditions in Tombstone Territorial Park and its surroundings (Ogilvie Mountains, central Yukon) (Lacelle et al., 2007, 2009; Grinter et al., 2019; Calmels et al., 2018). This PhD thesis aimed to fill this gap by 1) characterizing the distribution, morphometry, state and ice content of IW polygons in the study area, 2) defining the type and magnitude of landscape changes in the study area, and 3) modelling permafrost distribution, thermal conditions and sensitivity to climate changes in the study area. These three objectives were fulfilled through each contribution.

Firstly, characterization of IW polygons in TTP revealed that their development is constrained by hillslope processes and the hydrological network and is restricted to low-gradient slopes with mid-Holocene deposits the accumulated in the fluvial plains of the lower reaches of the Blackstone and East Blackstone rivers (Chapter 2), confirming our initial hypothesis. This contrasts with non-mountainous regions where IW polygons are more broadly distributed in low-lying areas, flat terrain or rolling hills (Kanevskiy et al., 2017; Bernard-Grand'Maison and Pollard, 2018; Steedman et al., 2017; Morse and Burn, 2013; Fraser et al., 2018).

Our initial hypothesis was that IW polygons sites with differing surficial characteristics would have different morphometric parameters and soil properties and would be associated with different development stages. However, further investigation of individual polygonal sites showed that only the vegetation type, surface wetness, and polygon network spatial pattern (random, intermediate, regular) are influenced by the development stage of IW polygons (developing, degrading, stabilized), while the size and angles of polygons seem independent of the development stage (Chapter 2). Additionally, we found that the spatial pattern of polygons network in TTP seems to be more closely influenced by the nature of the substrate than by its age, while the size of the polygons is more closely influenced by the age of the substrate, providing insight on the application of morphometric and soil parameters for the study of IW polygons. Also, because of the evidence of permafrost thaw-induced ponding and gullying observed along the Dempster Highway and in previous local studies (Lacelle et al., 2007; Grinter et al., 2019), we had originally hypothesized that IW polygons would mostly be in the degradation development stage. However, we found evidence of a range of development stages (developing, degrading, stabilized) based on polygons micro-topography and surface wetness, indicating that the degradation of IW might be constrained to locations close to the road.

Characterization of IW polygons also allowed for an estimation of wedge-ice content inferred from delineation of the centerlines of polygons troughs (Chapter 2), confirming our hypothesis. The occurrences of massive ice bodies appear to have limited distribution in TTP, and therefore IW likely represent the main type of massive ice, most of which are located in tundra valley bottoms.

Secondly, the Landsat-derived landscape change analysis of the TTP and surrounding region covering the 1986-2021 period and multi-level image interpretation (Chapter 3) showed that 24% of the study area experienced statistically significant spectral changes, with the most widespread changes being associated with vegetation (succession) and hydrological processes (erosion and deposition); a small proportion of waterbodies experienced changes in extent and only seven slumps were identified. Wildfires, which occupy 5.4% of the study area, were the most substantial sudden landscape change identified. These results refute our initial hypothesis that permafrost degradation would be observed through increased distribution of large thaw lakes and/or drained thaw lake basins, evidence of large thaw slumping, extensive vegetation greening and ponding associated with IW degradation. Instead, we find that the study area appears to have been experiencing a relative stability with regards to permafrost-related features. While other regions in the western Arctic that remained unglaciated have experienced substantial contemporary permafrost-related landscape changes, namely lake drainage and formation of thaw ponds (e.g., Jones et al., 2011; Labrecque et al., 2009; Lantz and Turner, 2015; Lauriol et al., 2009), other regions have also remained rather stable since at least the early Holocene (e.g., Edwards et al., 2016), or have experienced very heterogenous and asynchronous changes (e.g., Edwards et al., 2016; Frost et al., 2018; Jorgenson et al., 2022). We suggest a similar response of permafrost landforms where interactions between the geomorphic setting, ecological succession and glacial history of the region have led to the recent stability of the landscape with regards to landscape-scale perturbations that can be identified using the Landsat archive.

Lastly, modeling current and future permafrost conditions in the study area using the Northern Ecosystem Soil Temperature (NEST) model showed that permafrost has persisted through the 20th century and beginning of the 21st century and is currently present throughout the area (Chapter 4), confirming our original hypothesis. The model also predicts permafrost loss by 2100, which is in aligned with our hypothesis that permafrost is warming. The most determinant factors for permafrost distribution, conditions and sensitivity in the study area are a) vegetation height and LAI which determine the degree of exposure of the ground to solar radiation and the amount of heat loss during winter through snow drifting or trapping, b) surface organic layer which controls heat energy exchanges between the air, the surface and deeper ground, and c) the thickness of surficial deposits which influences the thickness of permafrost. Permafrost in the study area most likely went from being climate-driven in the Pleistocene to ecosystem-driven in the mid-Holocene, and it might become ecosystem-protected in the 21st century (French et al., 2017). Permafrost degradation in the study area could greatly impact slope stability and conditions of aquatic systems, and shrubification could contribute to increased degradation. Finally, our results allowed us to confirm the application of the NEST model in a mountainous region.

The findings from each contribution leads to a better understanding of TTP and its surroundings as a permafrost environment. It highlights how the region is a unique permafrost niche, not only because of its higher elevations and colder air temperatures, but also because of its glacial history and geomorphic setting. Going back to the Pleistocene up until the Last Glacial Maximum (ca. 24-21k BP), climate in central Yukon was much colder (4-5°C colder) and drier than today, leading to the great majority of the region in and near TTP to remain unglaciated, at least since the mid-Pleistocene (Lacelle et al., 2009; Viau et al., 2008). The region was then covered in tundra, permafrost was existent and IW polygons formed, until the early Holocene warm interval, when permafrost degraded, and tundra vegetation was replaced by open forests dominated by white spruce (Grinter et al., 2019; Cwynar and Spear, 1995). In the mid-Holocene, the climate cooled again which caused for the open forest of white spruce to be replaced by black spruce forest and green alder, and for permafrost to aggrade and permafrost features to stabilize (Cwynar and Spear, 1995; Dyke, 2005; Ritchie, 1984). As the cooling trend continued, the forest cover reached its current position in the southern part of TTP and gave way to tundra in the central and northern parts (Cwynar and Spear, 1995). Since then, accumulation of sandy silt colluvium with mostly pore ice to low excess ice in valleys has led to the area being relatively ice-poor, with the presence of near-surface excess ice being constrained to the low-gradient lower reaches of the Blackstone and East Blackstone river valleys as IW that began to develop 6500 cal yr BP (Frappier and Lacelle, 2021; Grinter et al., 2019). Some buried remnants of glacial ice also exist, but these have a very sporadic distribution (Lacelle et al., 2007). More recently, the widespread presence of grassland tundra and associated thick surface organic layer protects permafrost from heat penetration in summer and allows for heat loss in winter, contributing to the stability of permafrost under the recent warming conditions. Some IW polygons are in the development stage or stabilization stage, indicating that permafrost is indeed currently ecosystem-driven. Additionally, the fact that barren lands in the area are mostly associated with colluvium, and are therefore well drained, and have deep and cold permafrost, contributes to their relatively smaller thermal offsets and stability. Modeling of future changes does indicate permafrost loss by 2100, which could indicate that permafrost currently is or will become ecosystem-protected, and will no longer be able to recover under warmer conditions after degradation.

5.2. Key contributions

The main research goals of this PhD research project (outlined in section 4.1) were reached. The findings presented in this thesis are novel scientific contributions to the study of permafrost and ground ice conditions in and near the TTP. Key contributions include:

1. Novel detailed description of IW polygons, their distribution, morphometry and wedge-ice content in a sub-arctic mountainous area.
2. Insight on the application of morphometric and soil parameters, including IW polygons network pattern, for the assessment of IW polygons distribution, development stages and wedge-ice content.
3. Application of a Landsat-derived pixel-based Tasseled Cap indices trend analysis to a sub-arctic mountainous region.
4. Characterization of both monotonic (i.e., gradual or progressive) and non-monotonic (i.e., cyclical or irregular) landscape changes in the study area.
5. High-resolution modeling of permafrost distribution, thermal regime and predicted changes in the study area.
6. Application of the Northern Ecosystem Soil Temperature model to a mountainous region.
7. Understanding of the effects of the region's glacial history and geomorphic setting on current permafrost conditions.

5.3. Limitations and future research directions

While this thesis contributes to a better understanding of permafrost conditions in a poorly-studied area of Central Yukon, some limitations remain and additional research is needed to completely understand the state and fate of permafrost in the TTP and surrounding areas. These are discussed below.

The detailed morphometry, surface, vegetation and soil conditions of IW polygons is limited to sites within the East Blackstone river valley accessible through the Dempster Highway. While characterization of the morphometry and some surface conditions of other polygonal terrain was possible within the Blackstone river valley using remote sensing, a complete description of soil and vegetation conditions was not possible.

Landsat was chosen to conduct the TC indices trend analysis to detect landscape changes because it represents the longest continuous satellite imagery record (1985-today), and because various spectral indices have been developed to capture surface changes using Landsat. However, because of the mountainous topography and high elevations of the region, cloud cover is usually high in the summer, which made identification of clear-sky imagery difficult. This resulted in a low number of yearly observations to conduct the trend analysis in some areas of the study area. We also had to extend the peak summer growing season, choosing imagery from June 10th to August 31st , in order to obtain a satisfiable number of observations for the trend analysis. While we showed that only little non-significant bias could have been introduced based on the yearly acquisition dates, this still presents some risk of noise being introduced in the change signal, especially with relations to seasonal hydrological changes. Moreover, the medium spatial resolution (30 m) of Landsat imagery did not allow for identification and characterization of smaller-scale landscape changes. Therefore, the relative landscape stability highlighted by our results is limited to landscape disturbances that can be identified using Landsat imagery. Furthermore, smaller-scale monitoring and hydrological studies would be valuable to confirm the widespread wetting/gullying signal which we associate with potential changes of IW polygons.

Modeling of permafrost distribution and thermal regime is based on our current knowledge of the landscape, accessibility to field sites, and available data. While validation sites represent different landcover types and elevations within the study area, they are distributed on a latitudinal transect following the Dempster Highway because of the accessibility the road brings, which means that not all landcover types were covered (e.g., bedrock, colluvium, barren lands), and that they are not equally distributed within the study area. A larger number of validation points (thaw layer depths) would also be valuable in improving the accuracy and confidence of the modeling results. Furthermore, direct measurements of deep permafrost (>1m deep) physical properties and thermal conditions were not made. Given the fact that only shallow borehole data exists for the study area (Calmels et al., 2018; Lacelle et al., 2009), observations of deeper permafrost would allow for validation of deep permafrost temperature modeling, as well as ground ice content, as mentioned above.

Also, despite the presence of IW polygons and the usage of IW polygons validation sites for the modeling, the small-scale changes within polygonal terrain themselves were not modeled. It would be relevant to test whether the NEST model is able to predict thermal regime associated with small-scale changes in ground ice content, lateral drainage patterns, moisture content and vegetation types within IW polygons. This would require a large deployment of thermal sensors and sampling within polygons.

Some important implications associated with shrubland tundra were highlighted, namely the fact that a possible increase in shrub cover within the tundra could be under way, and the fact that shrubland tundra permafrost is the most sensitive to climate warming. It would be worthy to conduct further vegetation studies to confirm that shrubs are indeed proliferating, a phenomena that has been observed in other regions (e.g., Vuorinen et al., 2017; Weijers et al., 2018; Wilson and Nilsson, 2009), but that was not confirmed by direct measurements in our study area. This is significant because the modeling exercise did not consider changes in landcover over time. If shrub cover is indeed increasing, more important permafrost degradation and loss could occur.

5.4. References

Bernard-Grand'Maison C, Pollard W.(2018). An estimate of ice wedge volume for a High Arctic polar desert environment, Fosheim Peninsula, Ellesmere Island. Cryosphere,12(11):3589-3604. https:// doi.org/10.5194/tc-12-3589-2018

Calmels, F., Roy, L.P., Grandmont, K., Pugh, R., 2018. Summary of climate-and geohazard-related vulnerabilities for the Dempster Highway corridor.

Cwynar, L.C., Spear, R.W., 1995. Paleovegetation and Paleoclimatic Changes in the Yukon at 6 ka BP. Géographie physique et Quaternaire 49, 29–35. https://doi.org/10.7202/033027ar

Dyke, A.S., 2005. Late quaternary vegetation history of northern North America based on pollen, macrofossil and faunal remains. Geographie Physique et Quaternaire 59, 211–262.

Edwards, M., Grosse, G., Jones, B.M., McDowell, P., 2016. The evolution of a thermokarst-lake landscape: Late Quaternary permafrost degradation and stabilization in interior Alaska. Sedimentary Geology 340, 3–14. https://doi.org/10.1016/j.sedgeo.2016.01.018

Frappier, R., Lacelle, D., 2021. Distribution, morphometry, and ice content of ice-wedge polygons in Tombstone Territorial Park, central Yukon, Canada. Permafrost and Periglacial Processes 32, 587–600. https://doi.org/10.1002/ppp.2123

Fraser, R., Kokelj, S., Lantz, T., McFarlane-Winchester, M., Olthof, I., Lacelle, D., 2018. Climate Sensitivity of High Arctic Permafrost Terrain Demonstrated by Widespread Ice-Wedge Thermokarst on Banks Island. Remote Sensing 10, 954. https://doi.org/10.3390/rs10060954

Frost, G. v., Christopherson, T., Jorgenson, M.T., Liljedahl, A.K., Macander, M.J., Walker, D.A., Wells, A.F., 2018. Regional patterns and asynchronous onset of ice-wedge degradation since the mid-20th century in Arctic Alaska. Remote Sensing 10. https://doi.org/10.3390/RS10081312

Grinter, M., Lacelle, D., Baranova, N., Murseli, S., Clark, I.D., 2019. Late Pleistocene and Holocene ice-wedge activity on the Blackstone Plateau, central Yukon, Canada. Quaternary Research (United States) 91, 179–193. https://doi.org/10.1017/qua.2018.65

James, M., Lewkowicz, A. G., Smith, S. L., & Miceli, C. M. (2013). Multi-decadal degradation and persistence of permafrost in the Alaska Highway corridor, northwest Canada. *Environmental Research Letters, 8*(4). https://doi.org/10.1088/1748-9326/8/4/045013

Jones, B.M., Grosse, G., Arp, C.D., Jones, M.C., Anthony, K.M.W., Romanovsky, V.E., Jones, C.:, 2011. Modern thermokarst lake dynamics in the continuous permafrost zone, northern Seward Peninsula, Alaska. Alaska, J. Geophys. Res 116, 0–03. https://doi.org/10.1029/2011JG001666

Jorgenson, M.T., Kanevskiy, M., Roland, C., Hill, K., Schirokauer, D., Stehn, S., Schroeder, B., Shur, Y., 2022. Repeated Permafrost Formation and Degradation in Boreal Peatland Ecosystems in Relation to Climate Extremes, Fire, Ecological Shifts, and a Geomorphic Legacy. https://doi.org/10.3390/atmos13081170

Jorgenson, M.T., Romanovsky, V., Harden, J., Shur, Y., O'Donnell, J., Schuur, E. a G., Kanevskiy, M., Marchenko, S., 2010. Resilience and vulnerability of permafrost to climate change. Canadian Journal of Forest Research 40, 1219–1236. https://doi.org/10.1139/X

Kanevskiy M, Shur Y, Jorgenson T, et al. (2017). Degradation and stabilization of ice wedges: Implications for assessing risk of thermokarst in northern Alaska. Geomorphology,297:20-42. https://doi.org/10.1016/j.geomorph.2017.09.001

Labrecque, S., Lacelle, D., Duguay, C.R., Lauriol, B., 2009. Contemporary (1951 - 2001) Evolution of Lakes in the Old Crow Basin, Northern Yukon, Canada: Remote Sensing, Numerical Modeling, and Stable Isotope Analysis. Hawkings Source: Arctic 62, 225–238

Lacelle, D., Lauriol, B., Clark, I.D., Cardyn, R., Zdanowicz, C., 2007. Nature and origin of a Pleistocene-age massive ground-ice body exposed in the Chapman Lake moraine complex, central Yukon Territory, Canada. Quaternary Research 68, 249–260. https://doi.org/10.1016/j.yqres.2007.05.002

Lacelle, D., St-Jean, M., Lauriol, B., Clark, I.D., Lewkowicz, A., Froese, D.G., Kuehn, S.C., Zazula, G., 2009. Burial and preservation of a 30,000 year old perennial snowbank in Red Creek valley, Ogilvie Mountains, central Yukon, Canada. Quaternary Science Reviews 28, 3401–3413. https://doi.org/10.1016/j.quascirev.2009.09.013

Lantz, T.C., Turner, K.W., 2015. Changes in lake area in response to thermokarst processes and climate in Old Crow Flats, Yukon. Journal of Geophysical Research: Biogeosciences 120, 513–524. https://doi.org/10.1002/2014JG002744

Lauriol, B., Lacelle, D., Labrecque, S., Duguay, C.R., Telka, A., 2009. Holocene evolution of lakes in the Bluefish Basin, Northern Yukon, Canada. Arctic 62, 212–224.

Morse PD, Burn CR.(2013). Field observations of syngenetic ice wedge polygons, outer Mackenzie Delta, western Arctic coast, Canada. Case Rep Med.,118(3):1320-1332. https://doi.org/10.1002/jgrf.20086

Ritchie, J.C., 1984. Past and present vegetation of the far northwest of Canada. Past and present vegetation of the far northwest of Canada. https://doi.org/10.2307/2260178

Steedman AE, Lantz TC, Kokelj SV. (2017). Spatio-Temporal Variation in High-Center Polygons and Ice-Wedge Melt Ponds, Tuktoyaktuk Coastlands, Northwest Territories. Permafr Periglac Process.,28 (1):66-78. https://doi.org/10.1002/ppp.1880

Viau, A.E., Gajewski, K., Sawada, M.C. and Bunbury, J. (2008). Low-and high-frequency climate variability in eastern Beringia during the past 25 000 years. *Canadian Journal of Earth Sciences*, *14*, 1435-1453.

APPENDIX A: SUPPLEMENTAL INFORMATION FOR CHAPTER 2

Figure S2.1 Photographs of permafrost cores taken from a trough at the three East Blackstone River valley sites. A) Undegraded tundra polygons with ice wedge overlain by organic matter (Patch KM93; 0-32 cm below surface), B) Degrading tundra polygons with ice wedge overlain by ice-rich medium to coarse silts (Patch KM92; 61-97 cm below surface), C) Stabilized tundra polygon with ice lenses and organic-rich deposits deep in the trough (Patch KM95; 31-80 cm below surface)

Table S2.1 Gravimetric water, organic matter and carbonates content results from permafrost cores taken in one centre and one trough at the three East Blackstone River valley sites.

		Center				Trough			
Patch	Depth below surface (cm)	GWC (%)	Organic matter (%)	Carbonates (%)	Mean grain size (μm)	GWC (%)	Organic matter (%)	Carbonates (%)	Mean grain size (μm)
KM93	5								
KM93	10					603.9	93.1	0.2	
KM93	15					818.6	98.8	0.2	
KM93	20	403.3	96.4	0.2		730.3	97.2	0.1	
KM93	25	335.0	94.5	0.3		719.1	96.7	0.2	
KM93	30	331.6	95.5	0.2		959.1	98.7	0.1	
KM93	35	334.7	94.3	0.2		1106.7	97.1	0.0	
KM93	40	297.0	92.2	0.3					
KM93	45	186.0	91.3	0.2					
KM93	50								
KM93	55	259.5	91.5	0.3					
KM93	60	343.4	88.1	2.5					
KM93	65	403.5	92.3	0.2					
KM93	70	710.3	95.8	0.1					
KM93	75	838.4	97.3	0.1					
KM93	80	783.0	95.1	0.1					
KM93	85	667.8	93.7	0.2					
KM93	90								
KM93	95								
KM93	100								
KM93	105								
KM93	110								
KM93	Mean	453.3	93.7	0.4		822.9	96.9	0.1	
KM93	Median	343.4	94.3	0.2		774.4	97.2	0.1	
KM93	SD	216.5	2.5	0.6		182.4	2.1	0.1	
KM92	5								
KM92	10	584.1	80.6	0.4		701.3	80.6	0.4	
KM92	15	380.3	87.8	0.4		576.6	86.0	0.3	
KM92	20	112.1	27.3	1.3	14.9	623.3	91.6	0.2	
KM92	25	92.5	41.7	1.1	22.6	64.2	87.9	0.3	
KM92	30	111.6	31.9	1.3	19.0	73.2			
KM92	35	143.7	45.8	1.1		43.3	71.6	0.7	
KM92	40	144.4	31.3	1.2	21.2	87.5	14.2	1.2	13.6
KM92	45	178.5	33.1	1.2		161.7	5.4	1.2	
KM92	50	235.7	33.2	1.2	32.1	101.9	6.1	1.3	13.8
KM92	55	347.1	56.8	0.9		110.4	7.7	1.3	

KM92	60	295.2	26.4	1.3		104.8	17.6	1.3	
KM92	65	366.5	30.8	1.2		173.4	9.8	1.3	
KM92	70	305.2	66.1	1.0	47.9	145.0	11.0	1.3	14.1
KM92	75	234.3	24.3	1.8		81.8	43.7	1.1	
KM92	80	276.6	49.8	1.3			15.1	1.2	
KM92	85		11.4	2.1					
KM92	90	96.1							
KM92	95	226.6	14.6	1.8	16.7				
KM92	100	315.3	62.7	0.8					
KM92	105	204.2	26.6	1.7					
KM92	110								
KM92	Mean	244.7	41.2	1.2	24.9	217.7	39.2	0.9	13.8
KM92	Median	234.3	33.1	1.2	21.2	107.6	16.4	1.2	13.8
KM92	SD	124.4	21.2	0.4	11.6	229.6	35.8	0.5	0.3
KM95	5								
KM95	10					715.8	98.1	0.8	
KM95	15	298.1	94.1	0.1		678.0	94.0	0.4	
KM95	20	226.0	58.7	0.8		443.9	93.4	0.1	
KM95	25	155.8	25.7	3.5	13.1	359.0	80.1	0.5	
KM95	30	92.5	45.1	6.3	13.7	254.6	80.5	0.4	
KM95	35	72.3	56.9	5.8		134.9	46.0	1.1	
KM95	40	115.0	63.8	0.8	36.9	111.7	31.6	1.5	15.4
KM95	45	154.2	61.8	9.0		222.4	26.8	1.3	
KM95	50	217.6	68.0	7.2	35.7	211.6	42.7	1.2	18.9
KM95	55	229.0	57.4	6.9		331.8	77.2	4.8	
KM95	60	261.2	39.8	1.2		341.6	75.3	0.6	
KM95	65	263.1	65.9	0.9		575.1	60.6	0.8	
KM95	70	518.7	45.3	1.1	24.5	636.6	89.7	0.2	
KM95	75								
KM95	80	321.4	59.6	1.0		487.4	92.5	0.1	
KM95	85	534.4	43.6	1.0		635.3	97.2	0.1	
KM95	90	410.8	60.4	0.9		731.5	96.7	0.1	
KM95	95	404.4	72.9	0.8	44.5	806.5	97.0	0.1	
KM95	100	472.2	71.9	0.8		578.2	93.3	0.0	
KM95	105	344.8	83.1	0.5					
KM95	110								
KM95	Mean	282.9	59.7	2.7	28.0	458.7	76.3	0.8	17.2
KM95	Median	262.2	60.0	1.0	30.1	465.6	85.1	0.4	17.2
KM95	SD	142.3	16.2	2.9	13.0	220.3	24.1	1.1	2.5

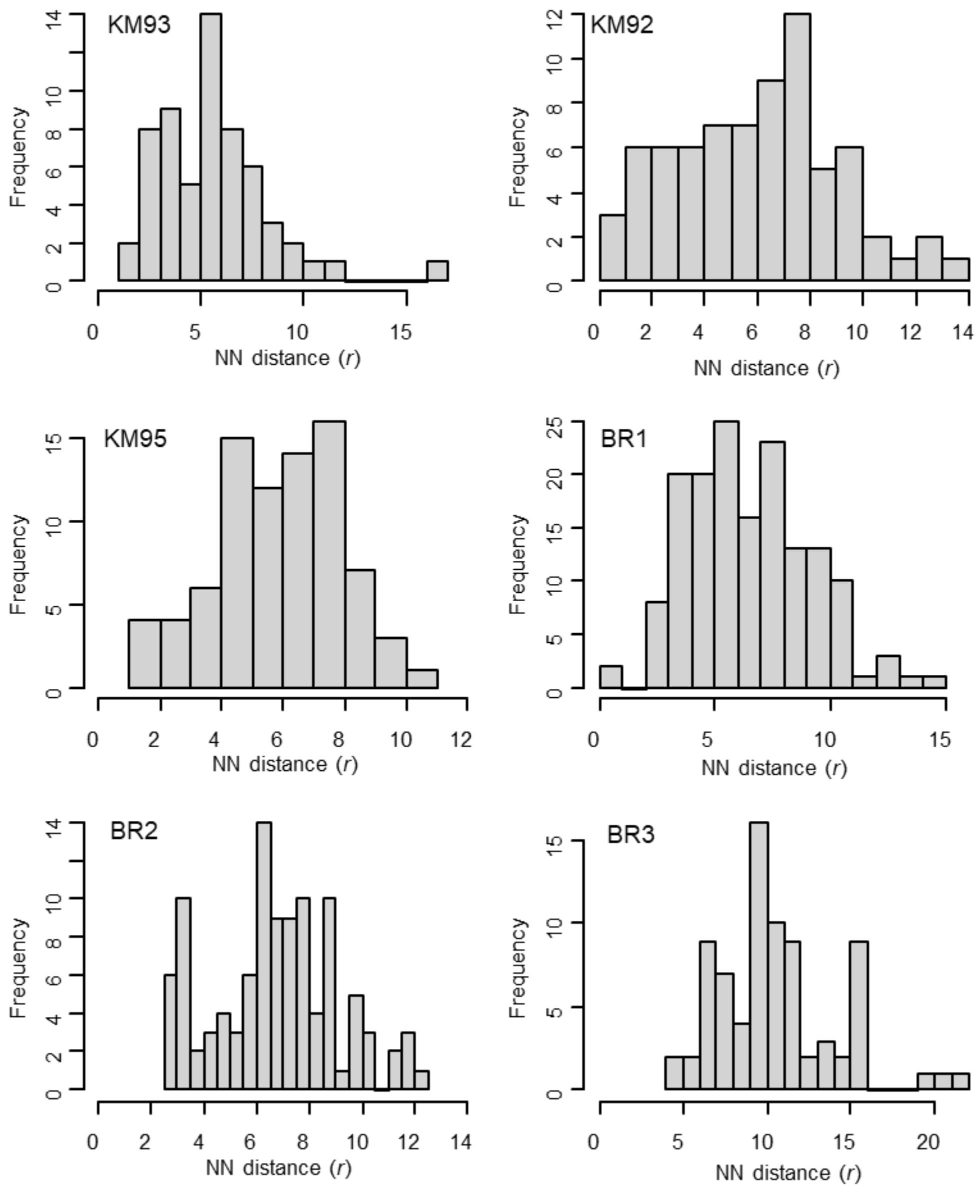

Figure S2.2 Histograms of nearest-neighbour distances of polygon intersections at six ice-wedge polygons sites in Tombstone Territorial Park, central Yukon, Canada.

Table S2.2 Maximum absolute deviation (MAD) test results between G(r) and $G_{CSR}(r)$ of six ice-wedge polygons sites in Tombstone Territorial Park, central Yukon, Canada

	KM93	KM92	KM95	BR1	BR2	BR3
MAD	0.14	0.22	0.3	0.18	0.32	0.32
p-value	0.595	0.06	0.005	0.014	0.001	0.006

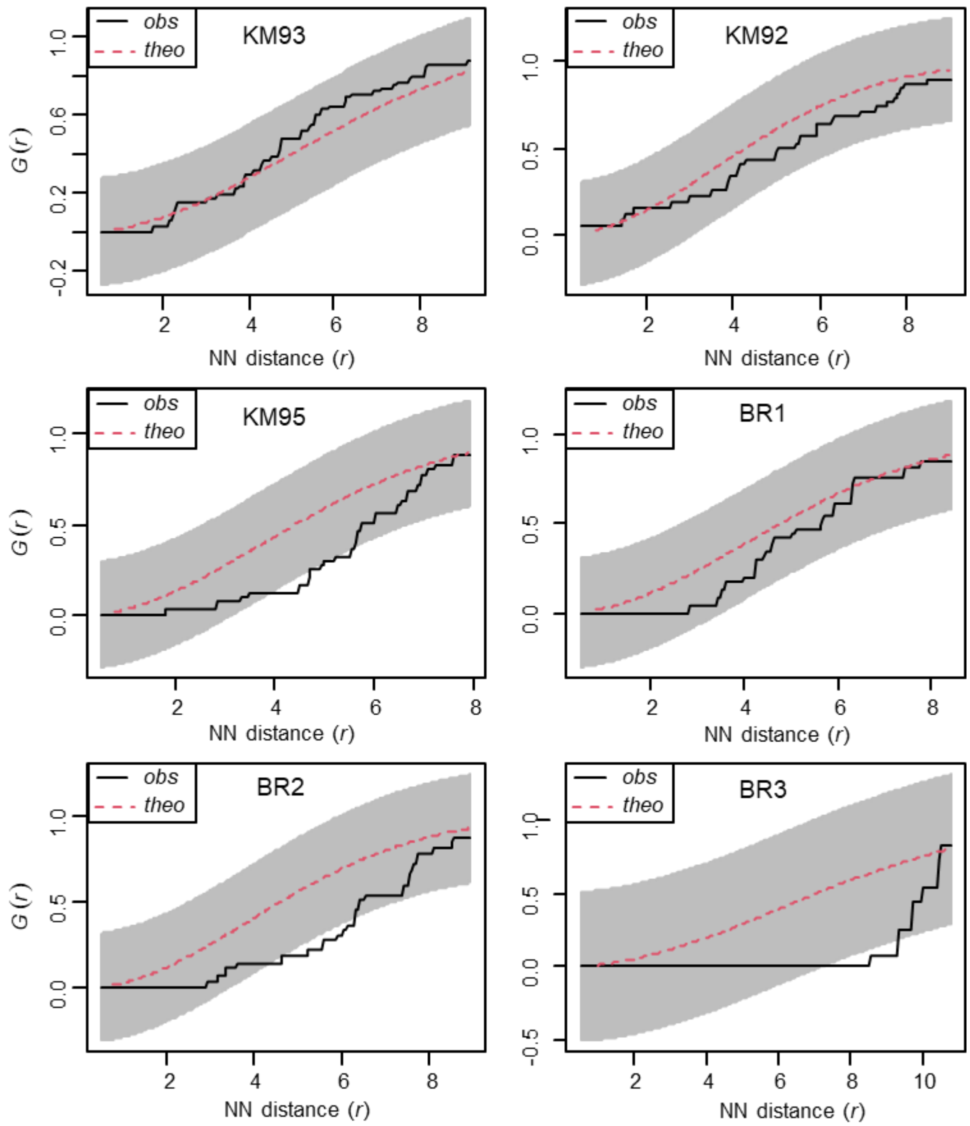

Figure S2.3 G-function with observed cumulative relative frequency distribution (G) of ice-wedge polygons intersections nearest-neighbour (NN) distances (r), theoretical values of G(r) for 999 simulations of complete spatial randomness (CSR), and 5th rank CSR envelope curves defining completely random distribution. Analysis performed with constant area of interest (5250 m^2) centered on each site.

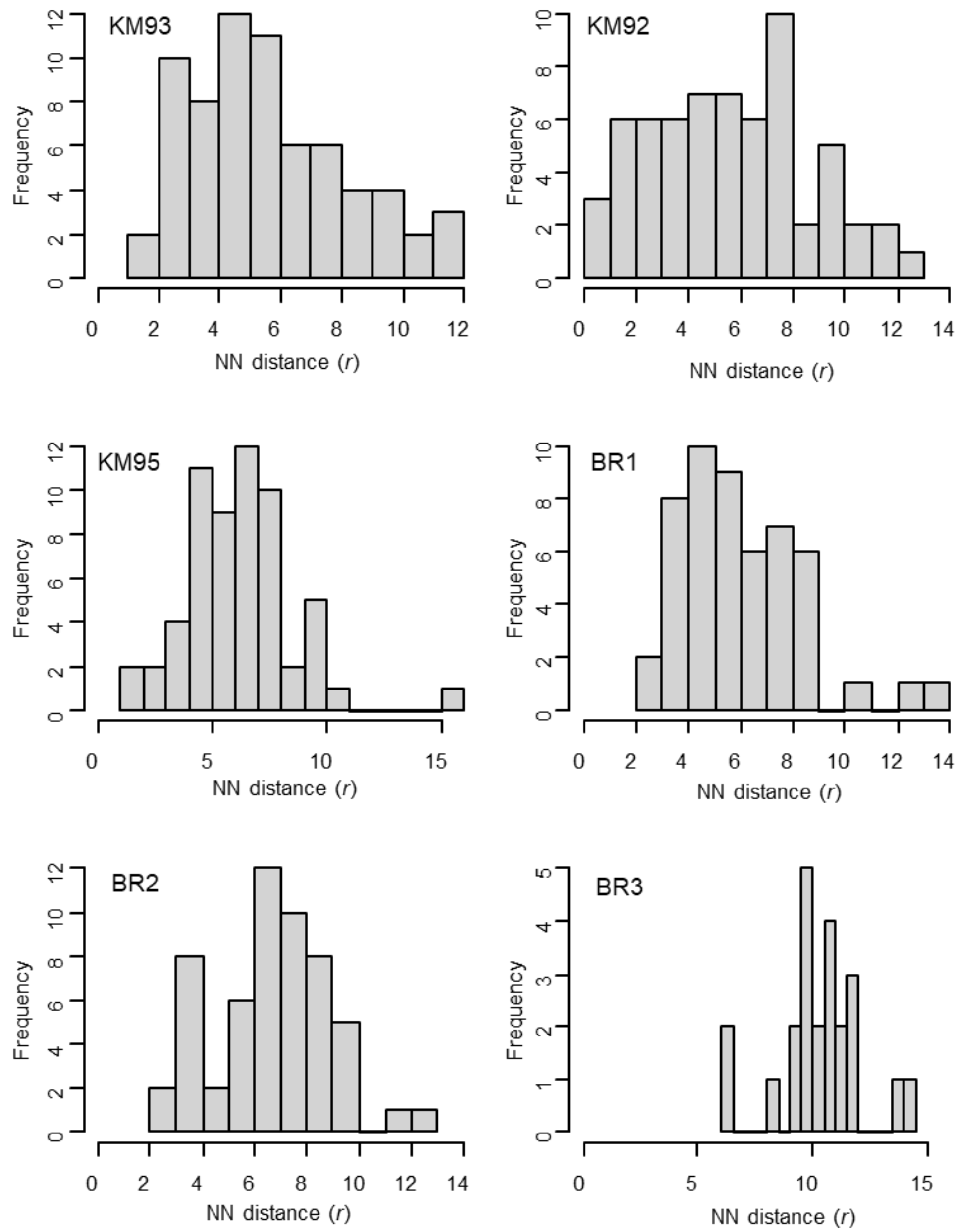

Figure S2.4 Histograms of nearest-neighbour distances of polygon intersections at six ice-wedge polygons sites in Tombstone Territorial Park, central Yukon, Canada. Analysis performed with constant area of interest (5250 m^2) centered on each site.

Table S2.3 Maximum absolute deviation (MAD) test results between G(r) and G_{CSR}(r) of six ice-wedge polygons sites in Tombstone Territorial Park, central Yukon, Canada Analysis performed with constant area of interest (5250 m^2) centered on each site.

	KM93	KM92	KM95	BR1	BR2	BR3
MAD	0.09	0.21	0.4	0.28	0.48	0.71
p-value	0.9	0.12	0.003	0.05	0.001	0.006

APPENDIX B : SUPPLEMENTAL INFORMATION FOR CHAPTER 3

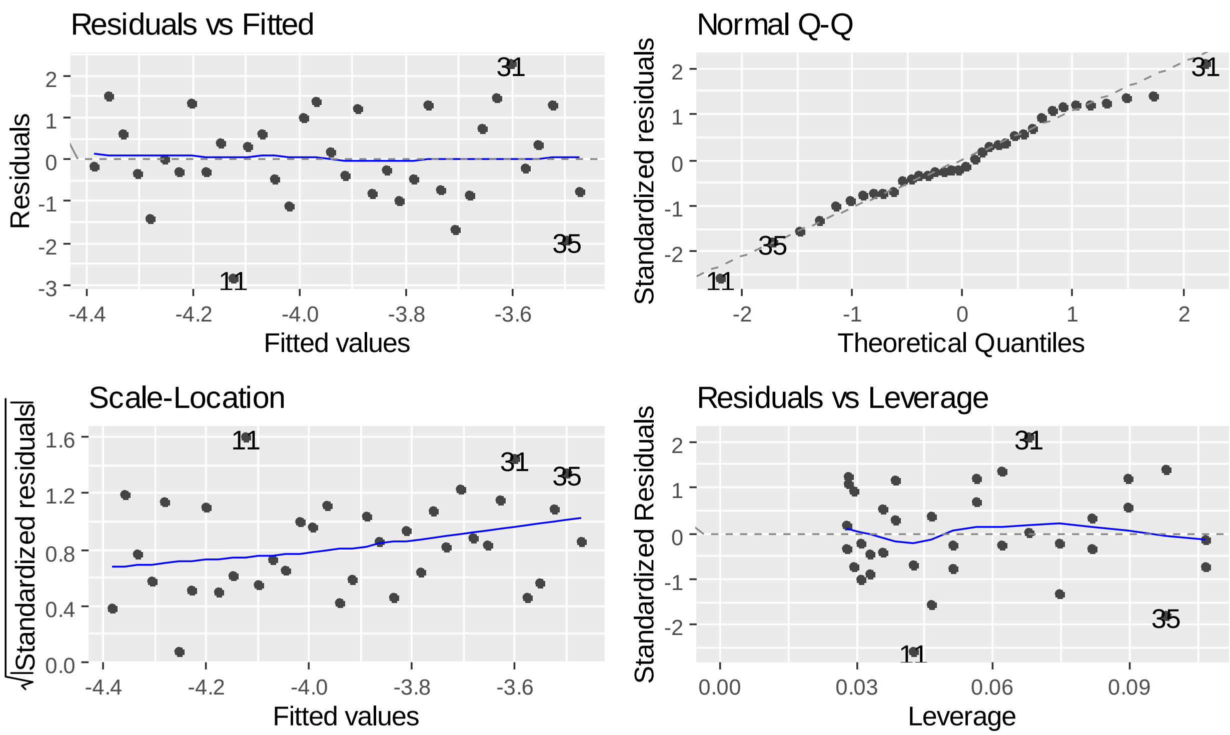

Figure S3.1 Residuals of Dawson City meteorological station mean annual temperature linear regression model

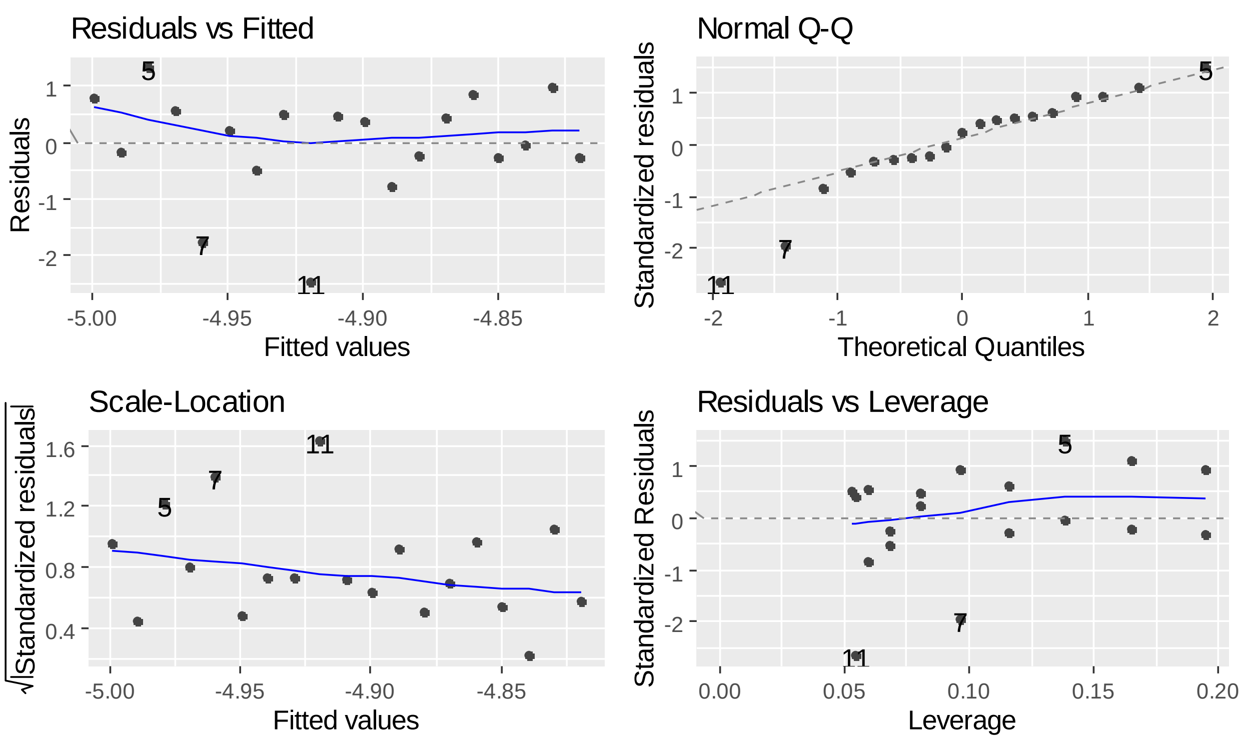

Figure S3.2 Residuals of North Klondike river station mean annual temperature linear regression model

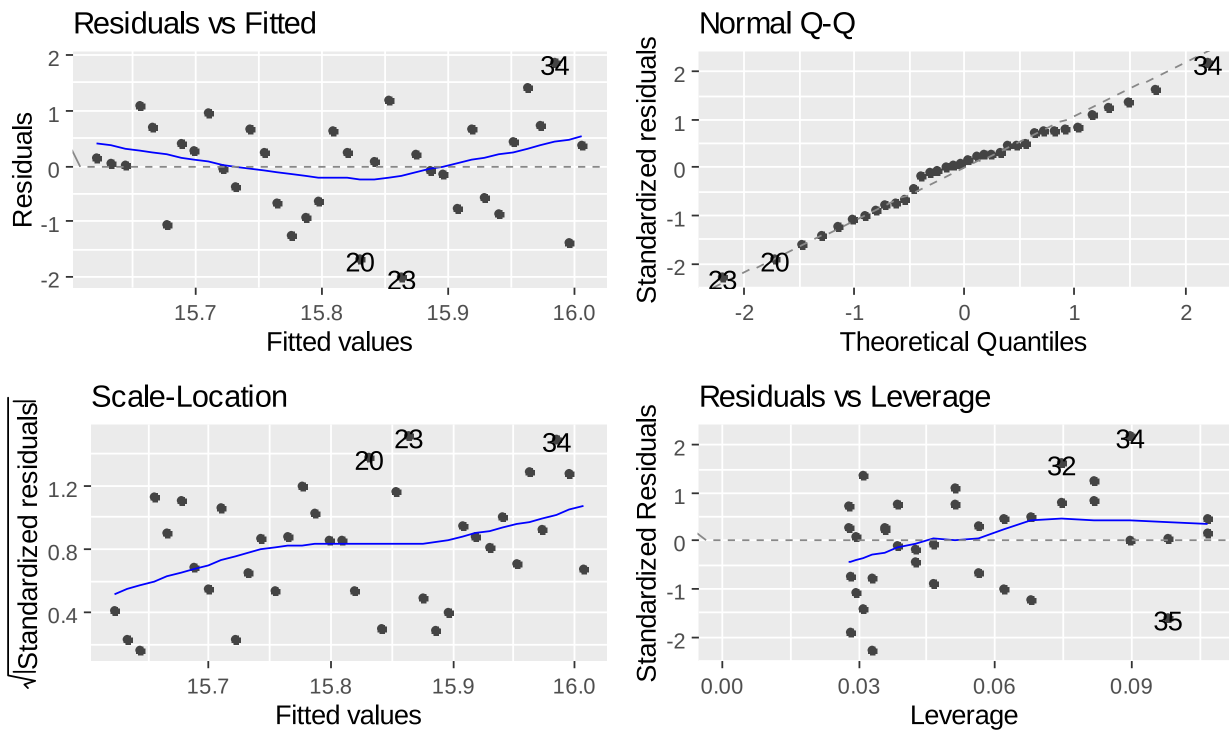

Figure S3.3 Residuals of Dawson City meteorological station mean July temperature linear regression model

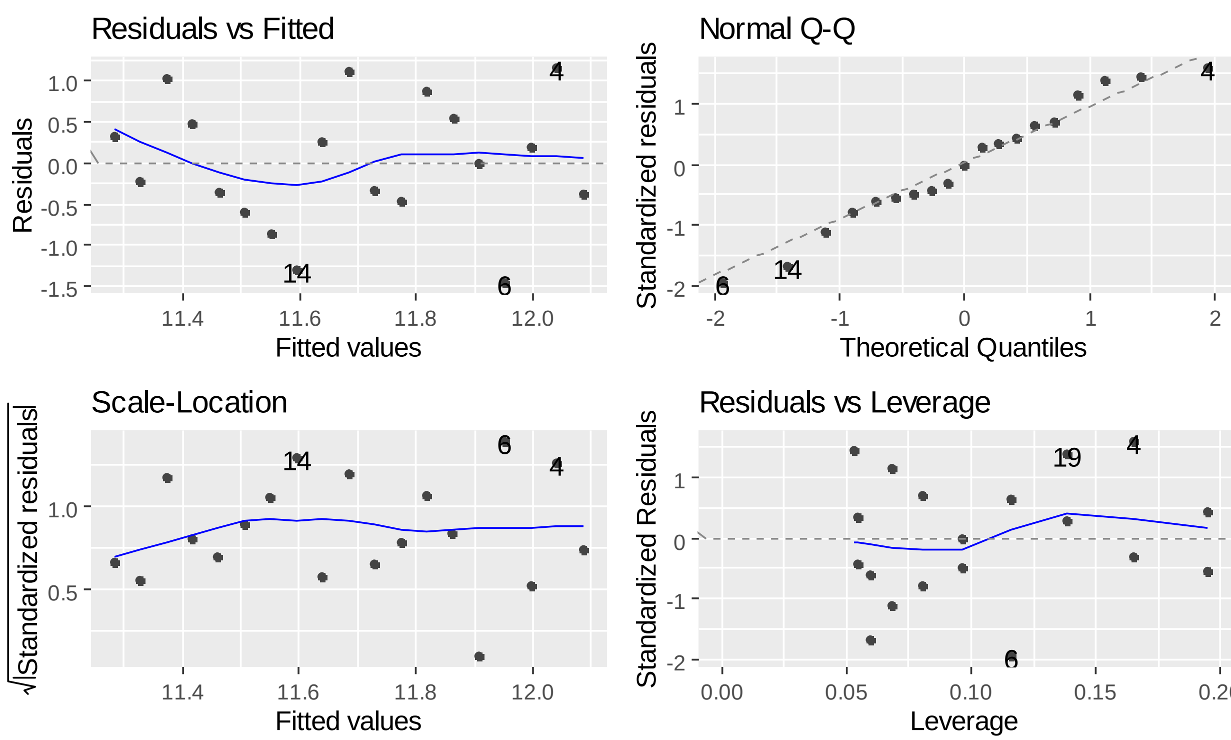

Figure S3.4 Residuals of North Klondike river meteorological station mean July temperature linear regression model

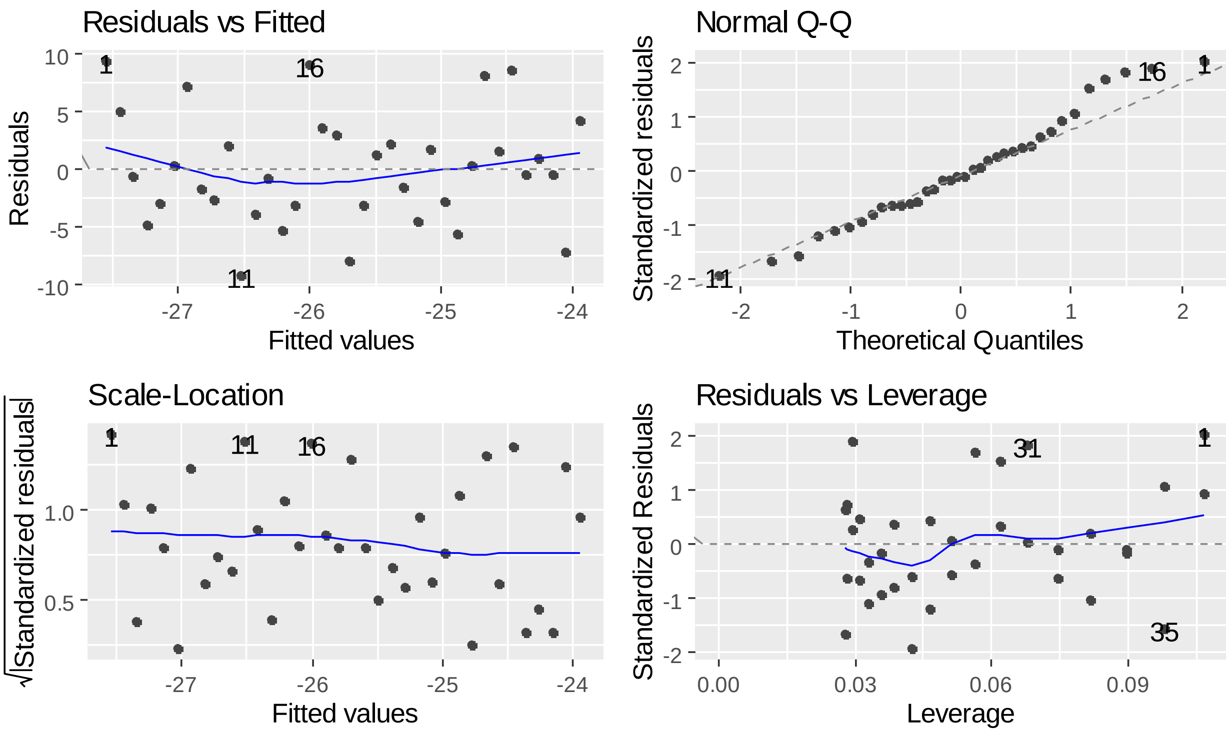

Figure S3.5 Residuals of Dawson city meteorological station mean January temperature linear regression model

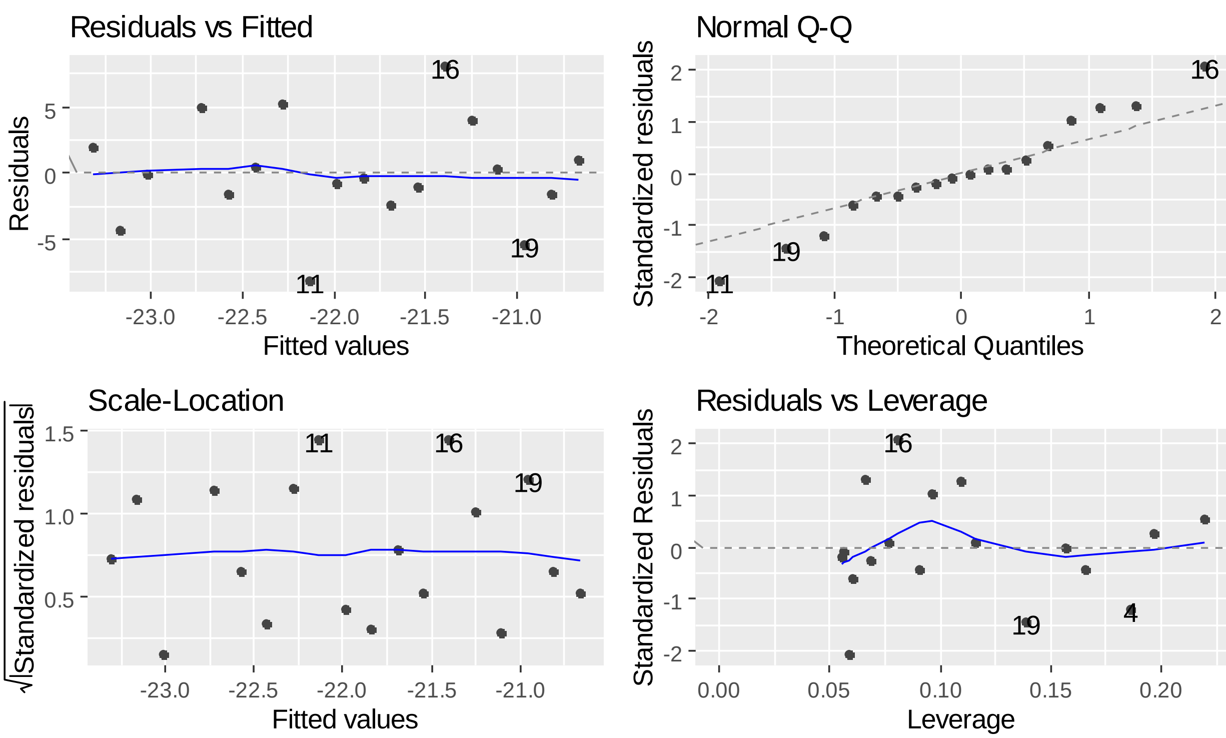

Figure S3.6 Residuals of North Klondike river meteorological station mean January temperature linear regression model

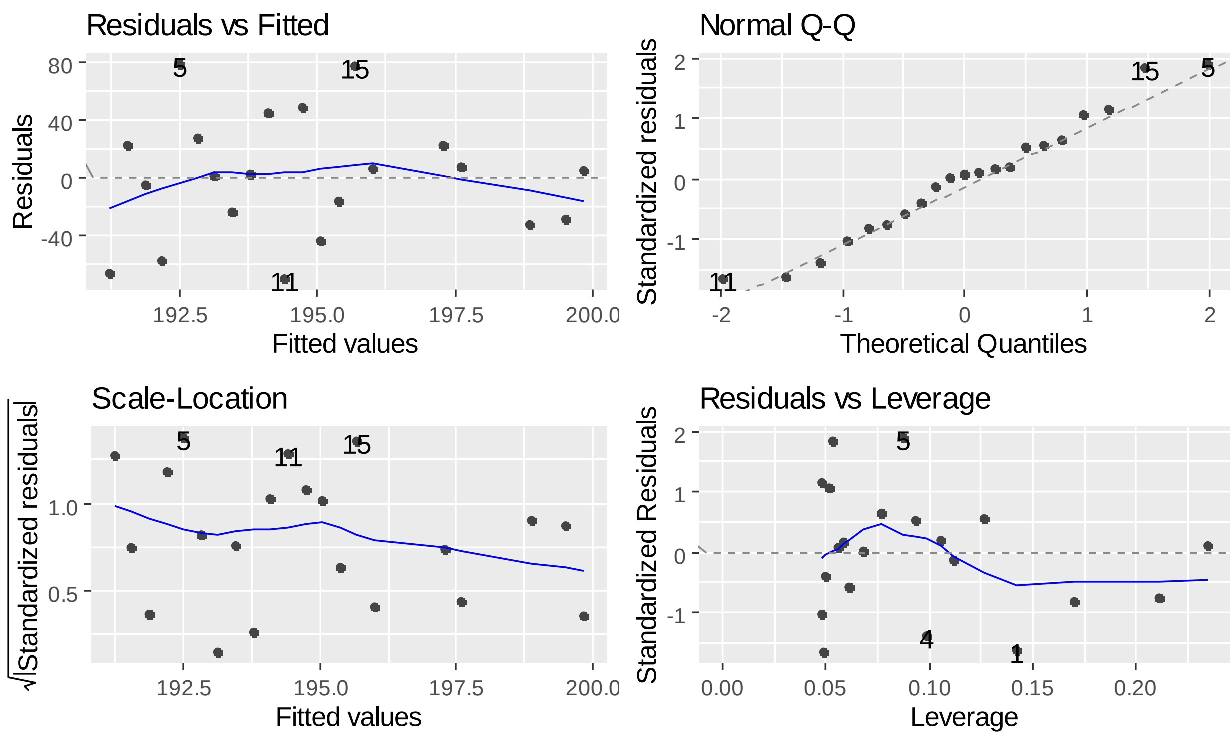

Figure S3.7 Residuals of Dawson City meteorological station total rain linear regression model

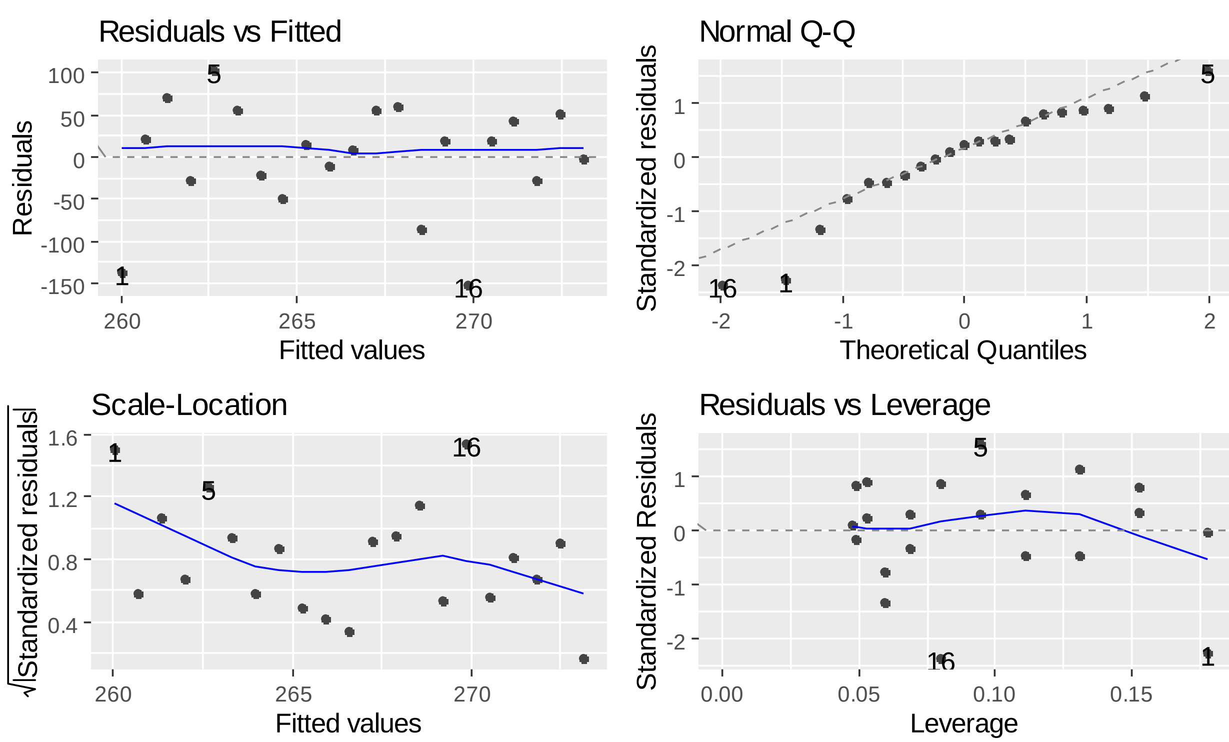

Figure S3.8 Residuals of North Klondike river meteorological station total rain linear regression model

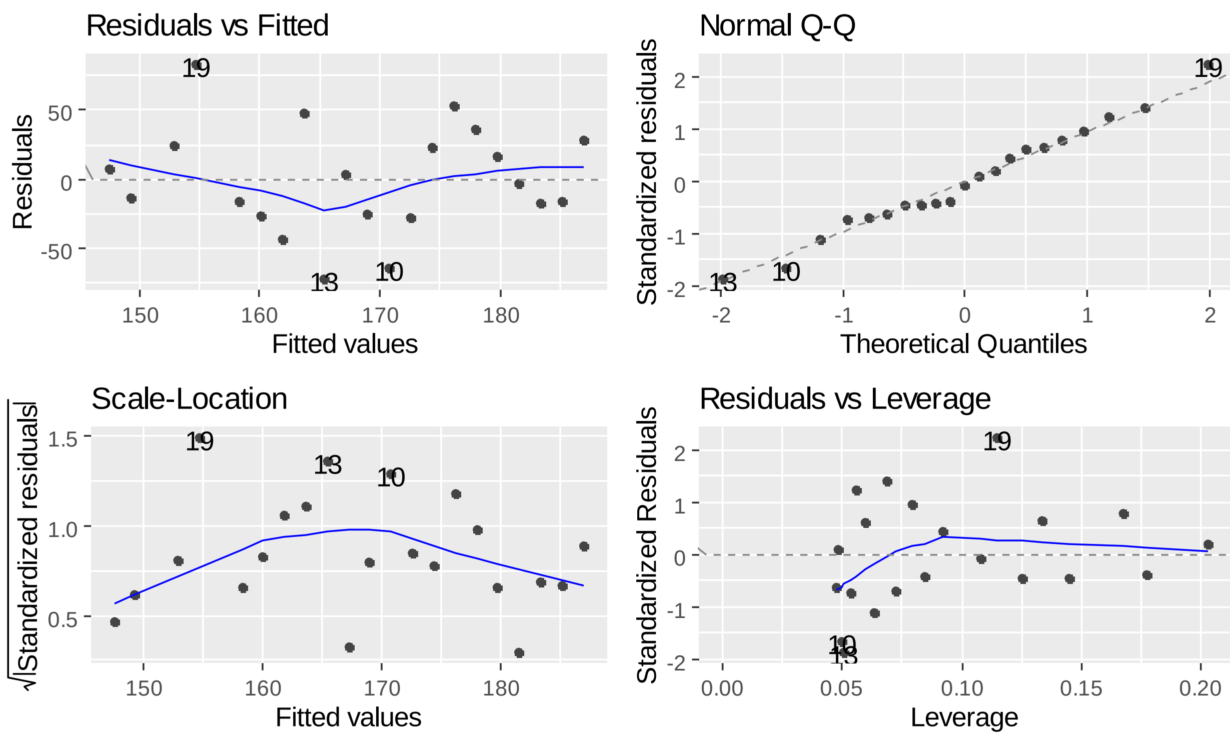

Figure S3.9 Residuals of Dawson City meteorological station total snow linear regression model

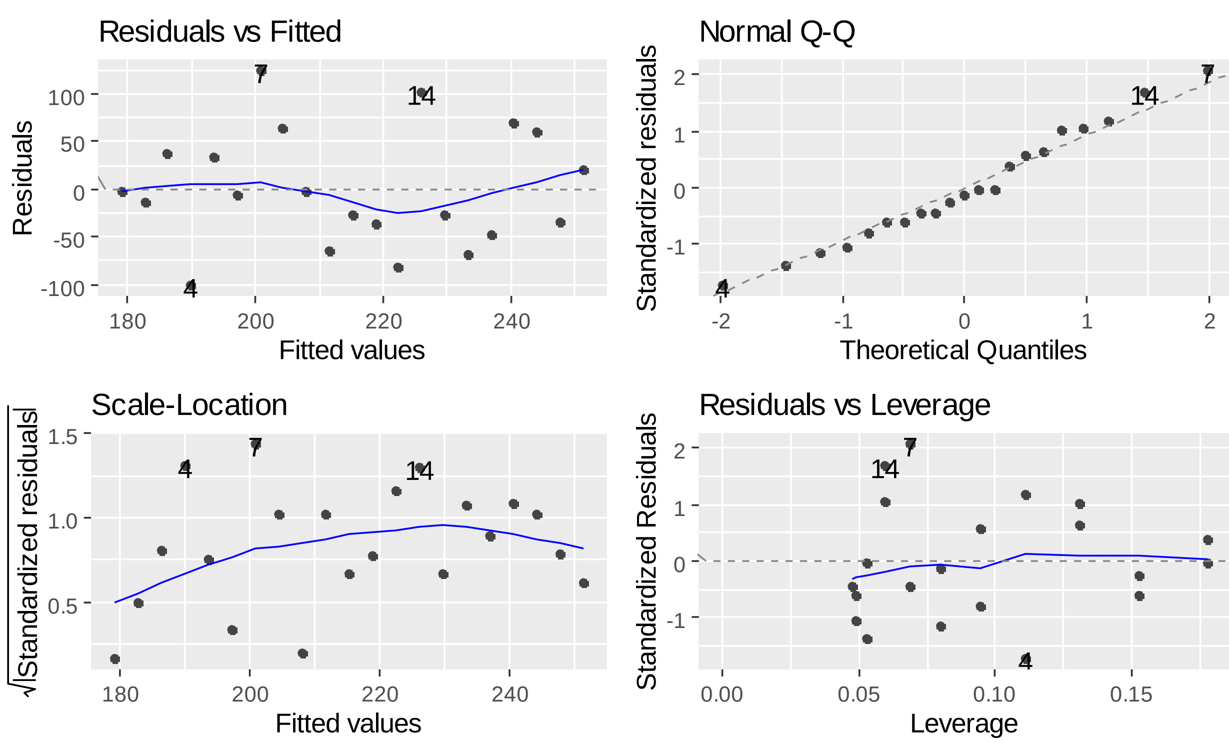

Figure S3.10 Residuals of North Klondike river meteorological station total snow linear regression model

APPENDIX C : SUPPLEMENTAL INFORMATION FOR CHAPTER 4

Table S4.1 NEST model input parameters for each unique landcover type class (combining landcover, surficial deposits and leaf area index) in and near the Tombstone Territorial Park, Central Yukon

ID	Landcover	LAI	Depth to bedrock (cm)	Mineral Soil Texture codea	Organic Layer Thickness (cm)	Organic layer organic matter content (%)	Layer 1 organic matter content (%)	Layer 2 organic matter content (%)	Degree of decomposition of organic matter	Ground ice	Rock fragments >2 mm	Vegetation type codeb	Vegetation height (m)	Snow drifting parameter (P)c
1	Barren on Colluvium	0.5	300	6	2	80	40	0	Low	Yes	Yes, up to 1 m above bedrock	5	0	0.8
2	Shrubland tundra on Colluvium	1.5	300	6	20	100	75	50	Med	Yes	Yes, up to 1 m above bedrock	4	0.2	-0.3
3	Grassland tundra on Colluvium	1.4	300	6	10	100	45	30	High	Yes	Yes, up to 1 m above bedrock	5	0.1	0.6
4	Grassland tundra on Colluvium	0.9	300	6	10	100	45	30	High	Yes	Yes, up to 1 m above bedrock	5	0.1	0.6
5	Boreal forest on Colluvium	1.5	300	6	20	90	85	70	Med	Yes	Yes, up to 1 m above bedrock	1	15	0.2
6	Grassland tundra on Colluvium	1.2	300	6	10	100	45	30	High	Yes	Yes, up to 1 m above bedrock	5	0.1	0.6
7	Shrubland-lichen-moss tundra on Colluvium	1.2	300	3	15	95	30	0	Med	Some	Yes	4	0.05	0.3
8	Boreal forest on Colluvium	1.8	300	6	20	90	85	70	Med	Yes	Yes, up to 1 m above bedrock	1	15	0.5
9	Shrubland tundra on Colluvium	4	300	6	20	100	75	50	Med	Yes	Yes, up to 1 m above bedrock	4	0.2	-0.3
10	Grassland tundra on Colluvium	1.5	300	6	10	100	45	30	High	Yes	Yes, up to 1 m above bedrock	5	0.1	0.6
11	Grassland tundra on Colluvium	1.8	300	6	10	100	45	30	High	Yes	Yes, up to 1 m above bedrock	5	0.1	0.5
12	Shrubland tundra on Colluvium	1.4	300	6	20	100	75	55	Med	Yes	Yes, up to 1 m above bedrock	4	0.2	-0.3
13	Barren on Colluvium	0.9	300	6	5	90	50	0	Low	Yes	Yes, up to 1 m above bedrock	5	0	0.8
14	Shrubland-lichen-moss tundra on Colluvium	1.4	300	3	15	95	30	0	Med	Some	Yes	4	0.05	0.3
15	Shrubland-lichen-moss tundra on Colluvium	1.5	300	3	15	95	30	0	Med	Some	Yes	4	0.05	0.3
16	Barren on Colluvium	1.2	300	6	5	90	50	0	Low	Yes	Yes, up to 1 m above bedrock	5	0	0.8
17	Shrubland-lichen-moss tundra on Colluvium	1.7	300	3	15	95	30	0	Med	Some	Yes	4	0.05	0.3
18	Barren on Colluvium	1.4	300	6	5	90	50	0	Low	Yes	Yes, up to 1 m above bedrock	5	0	0.8
19	Barren on Colluvium	0.2	300	6	0	0	0	0	Low	Yes	Yes, up to 1 m above bedrock	5	0	0.9
20	Grassland tundra on Colluvium	0.5	300	6	10	100	45	30	High	Yes	Yes, up to 1 m above bedrock	5	0.1	0.6
21	Grassland tundra on Alluvium	1.5	500	5, 7	10	100	60	20	High	Some	Some	5	0.1	0.6
22	Grassland tundra on Colluvium	1.7	300	6	10	100	45	30	High	Yes	Yes, up to 1 m above bedrock	5	0.1	0.55
23	Boreal forest on Alluvium	1.7	500	5, 7	30	90	85	70	Med	No	Some	1	20	0.4
24	Boreal forest on Colluvium	1.7	300	6	20	90	85	70	Med	Yes	Yes, up to 1 m above bedrock	1	15	0.4

25	Shrubland tundra on Colluvium	1.7	300	6	20	100	75	55	Med	Yes	Yes, up to 1 m above bedrock	4	0.2	-0.3
26	Shrubland tundra on Colluvium	2.1	300	6	20	100	75	55	Med	Yes	Yes, up to 1 m above bedrock	4	0.2	-0.3
27	Shrubland tundra on Colluvium	1.8	300	6	20	100	75	55	Med	Yes	Yes, up to 1 m above bedrock	4	0.2	-0.3
28	Boreal forest on Colluvium	2.1	300	6	20	90	85	70	Med	Yes	Yes, up to 1 m above bedrock	1	15	0.5
29	Grassland tundra on Alluvium	1.8	500	5, 7	10	100	60	20	High	Some	Some	5	0.1	0.5
30	Grassland tundra on Alluvium	2.1	500	5, 7	10	100	60	20	High	Some	Some	5	0.1	0.5
31	Grassland tundra on Colluvium	2.1	300	6	10	100	45	30	High	Yes	Yes, up to 1 m above bedrock	5	0.1	0.5
32	Grassland tundra on Colluvium	0.2	300	6	10	100	45	30	High	Yes	Yes, up to 1 m above bedrock	5	0.1	0.6
33	Shrubland tundra on Colluvium	1.2	300	6	20	100	75	55	Med	Yes	Yes, up to 1 m above bedrock	4	0.2	-0.3
34	Boreal forest on Colluvium	1.4	300	6	20	90	85	70	Med	Yes	Yes, up to 1 m above bedrock	1	15	0.2
35	Boreal forest on Colluvium	1.2	300	6	20	90	85	70	Med	Yes	Yes, up to 1 m above bedrock	1	15	0.2
36	Grassland-lichen-moss tundra on Colluvium	1.2	300	6	10	95	45	30	Med	Yes	Yes, up to 1 m above bedrock	5	0.05	0.8
37	Barren on Colluvium	1.5	300	6	5	90	50	0	Low	Yes	Yes, up to 1 m above bedrock	5	0	0.8
38	Shrubland-lichen-moss tundra on Colluvium	0.9	800	3	15	95	30	0	Med	Some	Yes	4	0.05	0.3
39	Barren on Colluvium	1.8	300	6	5	90	50	0	Low	Yes	Yes, up to 1 m above bedrock	5	0	0.7
40	Shrubland-lichen-moss tundra on Colluvium	0.5	800	3	15	95	30	0	Med	Some	Yes	4	0.05	0.3
41	Grassland tundra on Alluvium	1.2	500	5, 7	10	100	60	20	High	Some	Some	5	0.1	0.6
42	Grassland tundra on Alluvium	1.4	500	5, 7	10	100	60	20	High	Some	Some	5	0.1	0.6
43	Shrubland tundra on Alluvium	1.7	500	5, 7	20	100	85	75	Med	Some	Some	4	0.2	-0.3
44	Grassland tundra on Alluvium	1.7	500	5, 7	10	100	60	20	High	Some	Some	5	0.1	0.55
45	Shrubland tundra on Alluvium	1.8	500	5, 7	20	100	85	75	Med	Some	Some	4	0.2	-0.3
46	Boreal forest on Alluvium	1.4	500	5, 7	15	95	70	30	Med	No	Some	1	20	0.2
47	Boreal forest on Alluvium	1.8	500	5, 7	30	90	85	70	Med	No	Some	1	20	0.5
48	Anthropogenic on Alluvium	1.4	500	5, 7	0	0	0	0	Med	Some	Some	5	0	0.9
49	Anthropogenic on Alluvium	2.1	500	5, 7	0	0	0	0	Med	Some	Some	5	0	0.9
50	Boreal forest on Alluvium	4	500	5, 7	30	90	85	70	Med	No	Some	1	20	0.5
51	Water	1.2	N/A	N/A	N/A	N/A	N/A	N/A	N/A	N/A	N/A	N/A	N/A	N/A
52	Water	0.9	N/A	N/A	N/A	N/A	N/A	N/A	N/A	N/A	N/A	N/A	N/A	N/A
53	Boreal forest on Alluvium	2.1	500	5, 7	30	90	85	70	Med	No	Some	1	20	0.5
54	Boreal forest on Alluvium	1.5	500	5, 7	15	95	70	30	High	No	Some	1	20	0.2
55	Shrubland tundra on Alluvium	1.5	500	5, 7	20	100	85	75	Med	Some	Some	4	0.2	-0.3

56	Shrubland tundra on Alluvium	1.4	500	5, 7	20	100	85	75	Med	Some	Some	4	0.2	-0.3
57	Boreal forest on Alluvium	1.2	500	5, 7	15	95	70	30	Med	No	Some	1	20	0.2
58	Shrubland tundra on Alluvium	1.2	500	5, 7	20	100	85	75	Med	Some	Some	4	0.2	-0.3
59	Shrubland tundra on Alluvium	0.9	500	5, 7	20	100	85	75	Med	Some	Some	4	0.2	-0.3
60	Boreal forest on Alluvium	0.9	500	5, 7	10	95	70	30	High	No	Some	1	20	0.1
61	Grassland tundra on Alluvium	0.9	500	5, 7	10	100	60	20	High	Some	Some	5	0.1	0.6
62	Shrubland-lichen-moss tundra on Alluvium	0.9	300	3	15	100	30	0	Med	No	Yes	4	0.05	0.3
63	Wetland on Alluvium	1.2	500	5, 7	40	100	95	85	Med	Some	Some	5	0.1	0.8
64	Barren on Alluvium	1.2	500	5, 7	10	40	30	0	Low	Some	Some	5	0	0.7
65	Barren on Alluvium	1.4	500	5, 7	10	40	30	0	Low	Some	Some	5	0	0.7
66	Grassland tundra on Alluvium	0.5	500	5, 7	10	100	60	20	High	Some	Some	5	0.1	0.6
67	Water	0.2	N/A	N/A	N/A	N/A	N/A	N/A	N/A	N/A	N/A	N/A	N/A	N/A